UNIVERSITY OF CALIFORNIA, SAN DIEGO

Experiments on Electron Vortices in a Malmberg-Penning Trap

A dissertation submitted in partial satisfaction of the

requirements for the degree Doctor of Philosophy

in Physics

by

Travis Buell Mitchell

Committee in charge:

Dr. Charles F. Driscoll, Chairman
Professor Morteza Gharib
Professor Thomas M. O'Neil
Professor Cliff Surko
Professor Charles Van Atta

1993

The dissertation of Travis Buell Mitchell is approved, and it is acceptable in quality and form for publication on microfilm:

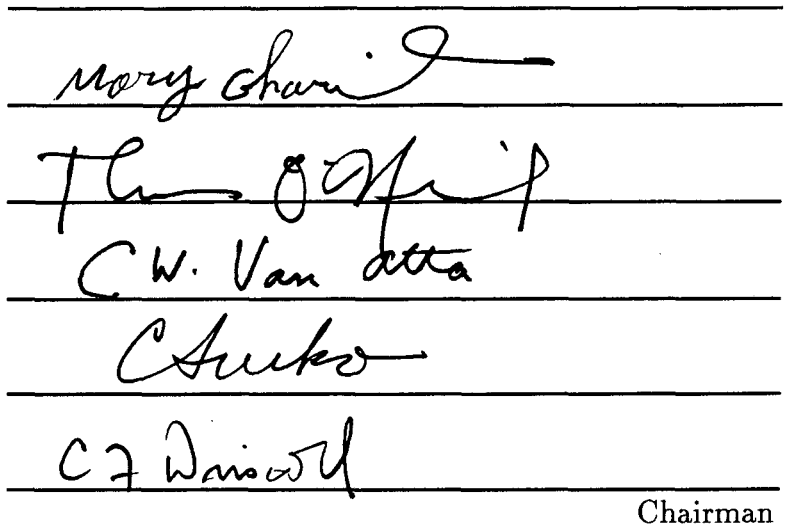

Chairman

University of California, San Diego

1993

This dissertation is dedicated to Marjorie Yoder Mitchell

Contents

List of Figures

List of Tables

Acknowledgements

It is a pleasure to acknowledge the people whose help, encouragement and support made this possible. Foremost among them has been my thesis adviser Fred Driscoll, some of whose generosity of spirit and unerring scientific insight I hope has rubbed off on me. Kevin Fine has been a teacher and friend since my first days in the non-neutral plasma group. If I have progressed in experimental technique from those days when my habit of burning out amplifiers necessitated the installation of special circuitry to protect the remaining ones, it is in large part thanks to him. Fred and Kevin also designed and constructed the EV containment device with which my dissertation research was done.

I owe a special debt of gratitude to the late John Malmberg for taking me into his research group, and for sharing so generously of his time, knowledge and enthusiasm. I am also grateful for the friendship and support of Dirk Hartmann.

I would like to thank the UCSD plasma community for its support and encouragement over the years. In particular, I have enjoyed talks with Bret Beck, Brian Cluggish, Steve Crooks, Pei Huang, Jim Kadtke, Nathan Mattor, John Moody, Tom O'Neil, Ralph Smith and Mark Tinkle. Bob Bongard and Jo Ann Christina provided technical and secretarial help in a way that always left me appreciative of their competance and good will.

Last but far from least, I would like to thank my family for their unswerving faith in me.

Financial support for this research was provided by Office of Naval Research grant N00014-89-J-1714 and National Science Foundation Grant PHY91-20240.

Vita, Publications and Fields of Study

Vita

17 February 1963	Born, Springfield, Illinois
1985	B.S., Swarthmore College
1986-1987	Teaching Assistant, Department of Physics University of California, San Diego
1987-1993	Research Assistant, Department of Physics
1988	M.S., University of California, San Diego
1993	Ph.D., University of California, San Diego

Publications

1. T. B. Mitchell. A Search for Nearby Stars in Sproul Parallax Fields. *Bull. Am. Astron. Soc.*, 19:641 (1987).

2. K. S. Fine, C. F. Driscoll, T. B. Mitchell and J. H. Malmberg. Dynamics and Instabilities of 2D Electron Plasma Vortices. *Bull. Am. Phys. Soc.*, 34:1932 (1989).

3. K. S. Fine, C. F. Driscoll, T. B. Mitchell and J. H. Malmberg. Symmetric Vortex Merger in Pure Electron Plasmas. *Bull. Am. Phys. Soc.*, 35:2135 (1990).

4. T. B. Mitchell, K. S. Fine and C. F. Driscoll. Observation of a Wall-Induced Instability of Two Interacting Vortices. *Bull. Am. Phys. Soc.*, 35:2135 (1990).

5. T. B. Mitchell, K. S. Fine and C. F. Driscoll, Dynamics of Two Electron Vortices in a Cylindrical Trap. *Bull. Am. Phys. Soc.*, 36:2331 and 36:2670 (1991).

6. K. S. Fine, C. F. Driscoll, J. H. Malmberg, and T. B. Mitchell. Measurements of Symmetric Vortex Merger. *Phys. Rev. Lett.*, 67:588 (1991).

7. T. B. Mitchell and C. F. Driscoll. Measurements of Asymmetric Vortex Merger. *Bull. Am. Phys. Soc.*, 37:1415 and 37:1804 (1992).

8. B. Cluggish, J. H. Malmberg, T. B. Mitchell and C. F. Driscoll. Damping of the $L = 1$ Diocotron Mode and Associated Transport. *Bull. Am. Phys. Soc.*, 37:1415 (1992).

9. T. B. Mitchell, C. F. Driscoll and K. S. Fine. Experiments on Stability of Equilibria of Two Vortices in a Cylindrical Trap. To appear in *Phys. Rev. Lett.*

Fields of Study

Major Field: Physics

Studies in Plasma Physics
Professors Pat Diamond, Daniel Dubin, Marshall Rosenbluth and William Thompson

Studies in Mechanics
Professor Joachim Appel

Studies in Electromagnetism
Professor Roger Dashen

Studies in Quantum Mechanics
Professor Julius Kuti

Studies in Statistical Mechanics
Professors Andrei Ruckenstein and Duncan Haldane

Studies in Nuclear Physics
Professor Keith Brueckner

Studies in Mathematical Physics
Professor Frank Thiess

Abstract of the Dissertation

Experiments on Electron Vortices in a Malmberg-Penning Trap

by

Travis Buell Mitchell

Doctor of Philosophy in Physics

University of California, San Diego, 1993

Dr. Charles F. Driscoll, Chairman

Experiments are presented on confined pure electron plasmas. These plasmas are cylindrical columns contained inside hollow conducting cylinders in an axial magnetic field. In the 2-dimensional $E \times B$ drift approximation, an electron column is a vortex evolving in (r, θ) according to the $2D$ Euler equation.

The 'diocotron' waves of a single vortex vary as $\exp(ik_z z + il\theta - i\omega t)$, with $k_z = 0$. The $l = 1$ wave is observed to damp at a rate strongly dependent on the radial position of the column in the cylindrical trap. The $l = 2$ and $l = 3$ waves exhibit a decay instability, where the mode l decays to mode $l - 1$. When this decay instability is prevented by negative feedback, exponential decay is observed.

Next, the center-of-mass motions of two vortices symmetric in radius and vorticity, and sufficiently well-separated to be stable to merger, are characterized. Equilibria are observed in which the vortices orbit about the center of the cylinder, with either oscillations about stable equilibria or exponential divergence away from unstable equilibria. The equilibrium positions, oscillation frequencies, and instability

rates for these spatially extended vortices agree well with the predictions of point vortex theory, apparently because surface waves and shape distortions do not couple significantly to the center-of-mass motion.

Finally, the merger of two vortices with unequal radii has been quantified. The two vortices merge rapidly when they are closer than a critical separation, but stay separated for many orbits when the separation is slightly larger. Merger is accompanied by the formation of filamentary arms, and results ultimately in an axisymmetric central core surrounded by a lower density halo. A simple algorithm for defining the core and halo of a merged vortex is found to be consistent with experiment. The self-energy of the merged core is found to be roughly the same as the sum of the self-energy of the merging vortices. The fraction of the total circulation entrained into the core varies from 70% to 90% as the ratio of the initial vortex radii is varied from 1:1 to 2:1. This fraction also depends on the initial placement of the two vortices.

Chapter 1

Introduction and Summary

1.1 Overview of Dissertation

In this work, I describe experiments on confined pure electron plasmas. The plasmas studied are electron columns contained inside a trap consisting of hollow conducting cylinders in a uniform axial magnetic field. The magnetic field provides radial confinement, and electrostatic fields on end cylinders provide axial confinement. Because John Malmberg pioneered use of these traps to study plasma processes [45], whereas Penning [55] used a similar geometry to make a cold cathode ionization gauge, I refer to the confinement device as a 'Malmberg-Penning' trap.

In the operating regime of the experiments, where the 2D $\mathbf{E} \times \mathbf{B}$ drift approximation is valid and where fast electron motions in the axial direction average over axial variations, the columns evolve according to the 2D Euler equation. The columns therefore evolve as would patches of vorticity in an incompressible and inviscid fluid contained in a circular tank. The vorticity of the flow is proportional to the electron density, and the sign of the vorticity is given by the sign of the charge [42].

This 'fluid analogy' adds to the significance of non-neutral plasma experiments: while non-neutral plasmas are a subject of increasing interest in their own right – having found homes in such diverse places as accelerators, free electron lasers,

atomic clocks and neutron stars – vortices have a tremendous importance due to the central role of vorticity in fluid dynamics and turbulence. I will be presenting both results which apply only to plasmas and results which also apply to fluid vortices. To help differentiate between these, I try to adhere to a convention that when the structures are referred to as columns, the phenomenon being described is unique to plasmas; when referred to as vortices, it is believed that the phenomenon also applies to 2D fluid vortices.

As will be seen, several of the complications of vortex experiments using conventional fluids do not apply to electron systems. For example, in the electron system there is no boundary layer at the containing wall to complicate the dynamics, and the Reynolds number is high: an electron vortex can rotate about its axis over 10^5 times before its radius doubles due to 'viscosity'. Additionally, the vorticity is easily manipulated, accurately measured and directly imaged [17]. As a consequence of these advantages, I have been able to quantitatively study some basic vortex phenomena which have not been satisfactorily examined before.

The dissertation is organized as follows. Chapter 2 consists of background information on non-neutral plasmas in general, and the 'Equilibrium Voltage' (EV) containment device in particular. The operation and diagnostics of the EV device are described in detail, some relevant previous results on transport and temperatures are reviewed, and the fluid analogy (and observed discrepancies from it) is discussed.

Chapter 3 contains the results of studies of a single vortex/column. I first describe studies of the damping of surface waves characterized by the azimuthal mode number l (i.e. varying as $\cos(l\theta)$), but having no axial variation ($k_z = 0$). In fluid dynamics, these are referred to as Kelvin waves on a vortex; in plasma physics they are referred to as diocotron waves. The $l = 1$ wave corresponds to a column displaced from the center of the cylindrical trap. Measurements of the radius and

displacement of such a column show changes at rates strongly dependent on radial position. I find that while both angular-momentum-conserving and -nonconserving transport is taking place, the data is consistent with an exponential damping of the l=1 wave. The measured rates of this damping, however, are somewhat higher than those predicted by a preliminary theory [11].

The $l \geq 2$ diocotron waves can be damped by a spatial Landau-mechanism resonance damping [5, 14]. I have discovered, however, that small amplitude $l = 2$ and $l = 3$ waves, even when stable to resonance damping, are unstable to a decay instability. In this instability, the l wave decays to both an exponentially growing $l-1$ 'daughter' wave and presumably to a resonant band of particles. When the decay instability is suppressed by negative feedback on the daughter wave, exponential damping on slow 'viscous' timescales is observed to occur. Finally, I have observed $l = 3$ perturbations to grow exponentially on highly elliptical vortex structures. This appears to be the first experimental observation of an instability predicted 100 years ago by Love [44].

I have investigated the use of external electric fields rotating in the θ-direction to transfer angular momentum to the column [25] and have achieved significant transfer accompanied, however, by a large amount of heating. The central density increases by about 50%, and the column becomes somewhat narrower. The coupling of the fields to the column is through electron plasma waves.

Finally, I describe some measurements of the $l = 0$, $k \neq 0$ 'sloshing' density perturbations induced on an off-axis column, when the magnetic field is not aligned with the trap axis [33]. I quantify the relationship between the $l = 0$ signal amplitudes and the confinement times of the plasma in the EV apparatus, and present a more complete interpretation of the use of these signals to align the magnetic field with the trap.

Chapter 4 describes experiments on two vortices symmetric in vorticity and radius. The (r, θ) drift motions of the 'center-of-vorticity' of two vortices, sufficiently well-separated so as to be stable to merger [29], are described first. Equilibria are observed in which the vortices orbit about the center of the cylinder, with either oscillations about stable equilibria or exponential divergence away from unstable equilibria. The equilibrium positions, oscillation frequencies, and instability rates are obtained with high accuracy. I find that these results agree closely with predictions of a simple point vortex theory, where the spatially extended vortices are replaced with point vortices of the same circulation. I have extended the stability theory to the case of equilibria at unequal radial positions. The wide-ranging agreement between experiments and point vortex theory suggests that surface waves and shape distortions do not couple significantly to the center-of-vorticity motion, at least at the precision of the current measurements.

I then discuss the lifetime of the 2 vortex state, which is observed to vary by 5 orders of magnitude depending on the initial placement of the columns. For small initial separations, immediate vortex merger is observed when the separation between symmetric vortices, d_{12}, is below a critical value given by $d_{12} \sim 3.2\rho_v$, where ρ_v is the vortex radius [29]. This high precision measurement is consistent with a range of fluid theory and simulation, and improves upon more qualitative fluids experiments. Rapid merger is also observed for some large initial separations, because dynamical instabilities can result in the vortices immediately drifting into each other.

Vortices injected onto stable equilibrium points at larger separations are found to become unstable to merger on long time scales due to the column expansion discussed in Chapter 3. The observed rates of expansion are consistent with those measured for single columns. Lifetimes are anomalously low, however, for vortices injected onto unstable equilibrium points. I believe this is due to a greatly enhanced

rate of column expansion that occurs when the column trajectories move periodically in radius.

In Chapter 5, the merger of two vortices with differing radii, but equal in peak vorticity, is quantified. This asymmetric vortex merger is a topic of current interest due to its relevance to the problem of freely evolving 2D turbulence [46]. The two vortices merge rapidly when they are closer than a critical separation, but stay separated for many orbits when the separation is slightly larger. Merger is accompanied by the formation of filamentary arms, and results ultimately in an axisymmetric central core surrounded by a low density halo. The peak vorticity of the merged core is observed to be roughly the same as that of the merging vortices. The vorticity profile of the core and halo, and the lifetimes of the two-vortex state, are observed to be dependent on the initial placement of the two vortices.

The halo can be defined as that part of the merged profile sufficiently far away from the core that it is not bound, i.e. far enough that subsequent encounters with other vortices can advect it away. This suggests a simple, consistent algorithm for defining the core and halo of a merged vortex. Using this algorithm, it is found that the fraction of the total circulation entrained into the central core after a merger varies from 70% to 90%, as the initial vortex radii are varied from 1:1 to 2:1. Additionally, the self-energy of the merged core is found to be roughly the same as the sum of the self-energy of the merging vortices. The quantitative picture of asymmetric merger which emerges from the experiments is consistent with some 2D turbulence theories based on direct numerical simulations of the Euler equations [8, 69], but inconsistent with results obtained from contour dynamics simulations [21].

Chapter 2

Background

2.1 Overview

In this chapter I present some background information on Malmberg-Penning traps in general, and the Equilibrium Voltage (EV) trap in particular. Since research on non-neutral plasmas has been going on for years, and much of this is of relevance to my experiments, I include a fair amount of review of previous work. A useful review of larger scope can be found in Roberson and Driscoll [60].

2.2 Description of EV Containment Device

The EV device is a trap which uses crossed magnetic and electric fields to contain clouds of electrons within a cylindrical boundary [26]. The exterior is a cylindrical vacuum vessel, constructed of low-permeability stainless steel and maintained at an operating pressure of $\sim 4 \times 10^{-10}$ torr. Around the vacuum vessel is a water-cooled solenoid, which provides an axial magnetic field B_z of up to 470 Gauss. This field provides the radial confinement of electrons by constraining them onto small Larmour orbits about the field lines. Two small saddle coils provide magnetic fields B_x, B_y perpendicular to the main field, for the purposes of cancelling out the Earth's magnetic field and aligning B_z with the trap axis.

Within the vacuum vessel, and aligned with it, are a series of hollow, cylin-

drical electrodes. Electrons are injected into these electrodes from a filament source consisting of an ohmically heated spiral of tungsten wire. After injection, axial confinement is ensured with negative confining potentials V_c on 'gate' electrodes, whose axial separation L_c determines the length of the confined column. The confining potential, V_c, is chosen to be sufficiently negative to reflect electrons back to the confined region when they move towards the gate electrodes. Since positive ions are not confined axially, the electron plasma contains a negligible number of ions.

Fig. 2.1 is a schematic of the EV device interior, showing the arrangement of the electrodes. Next to the filament source is a region consisting of eight cylindrical electrodes of gold-coated OFHC copper. During confinement of a column, two of these are used as confinement gates: the one nearest the filament is the 'inject' gate and the other is the 'dump' gate. The electrodes all have an inside radius $R_w = 3.81$ cm and a length $L_{cyl} = 7.89$ cm, except for one (L2) which is 4.07 cm long. The electrode labeled 'S' is azimuthally divided into four 60° wall sectors and a frame, which allows pickup and control of $\theta -$ asymmetric waves.

At the opposite end of this region from the filament is a positively biased collimator plate, with three holes of varying size spaced 120° apart. The collimator can be rotated about its axis, which is offset from and parallel to the axis of the containment electrodes. This allows the desired collimator hole to be positioned anywhere along an arc passing through the trap's axis. Only the smallest hole, of radius $R_{coll} = 1.59$mm, was used in this work.

Beyond the collimator plate is a velocity analysis region, consisting of four electrodes. Concentric with and centered lengthwise on one of these electrodes (A3) is a small magnetic solenoid. At the end of the analysis region is a charge collector, biased to +158 V, which can be used to measure the number of electrons passing through the collimator plate and analyzer region. The analysis electrodes and

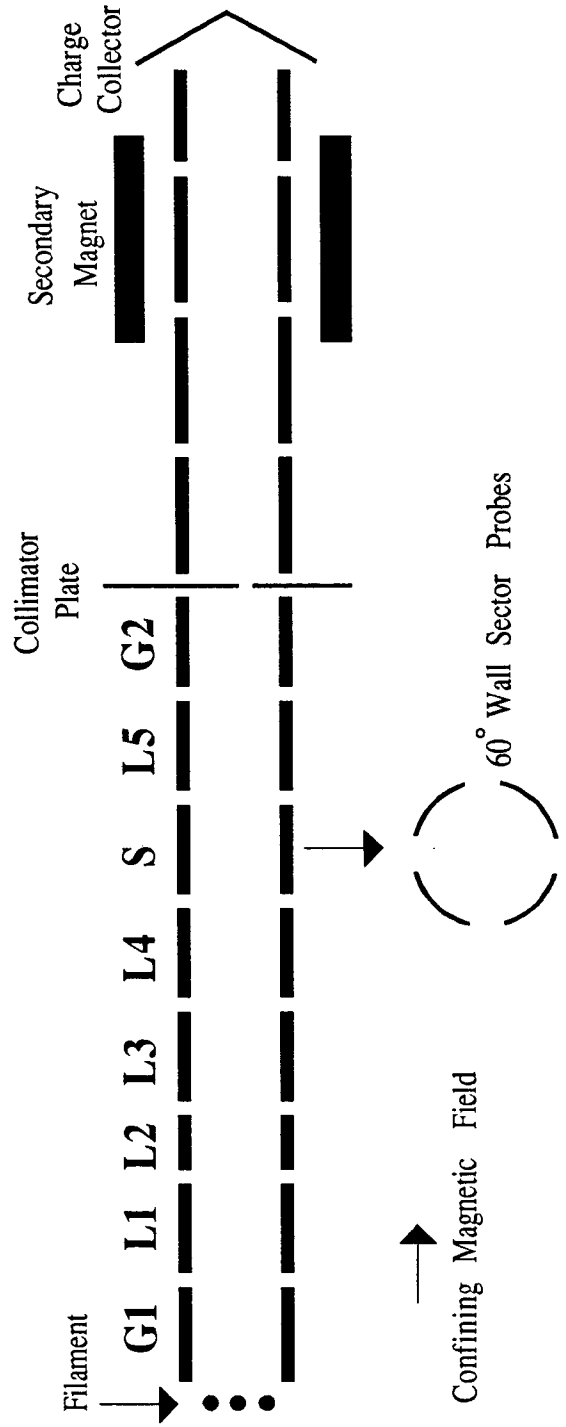

Figure 2.1: Schematic diagram of the EV apparatus interior.

secondary magnet allow a measurement of both the perpendicular and parallel temperature distributions, $T_\perp$ and $T_\parallel$, of the electrons which pass through the collimator hole.

2.3 Operation of the EV Apparatus

A typical experimental cycle consists of several different manipulations and measurements. There will be at least four phases: injection, manipulation (to achieve the desired initial condition), experiment, and dump. These cycles are run in a repetitive mode at $\sim$ 1 Hz; density profiles and temperature profiles are then built up from many measurements of plasmas with nearly identical initial conditions. Such profiles rely on a high degree of reproducibility: typically, uncontrolled shot-to-shot variations in density of less than 0.5% are seen.

For injection, the inject gate is grounded for $\sim$ 100 μsec, during which time an electron column forms between the filament source and the dump gate. The formed column will have a potential (due to space charge) matching that of the source [45]. The inject gate is then ramped to a containment voltage V_c, which traps the column and isolates it from the filament.

The source was designed to produce an electron column whose charge density is radially uniform: the filament source is wound in an Archimedes spiral geometry, giving (to lowest order) a parabolic radial potential across it. The column density is mainly determined by this parabolic potential, which is set by the filament current (normally 9.6 A). The temperature of the column is largely determined by the spacing of the filament, i.e. the voltage drop between each winding. With normal operation of the filament, columns with densities of $n \sim 5 \times 10^6 \mathrm{cm}^{-3}$, and temperature $T \sim 0.3$ eV, are formed. The radius of the injected column can be set by changing the bias potential V_{bias} at the filament center, since the potential at the column center must

equal this potential and the column density is fixed.

The specific manipulations required to set up an initial condition will depend on the experiment. One such manipulation, very often used, is electrostatic 'tilt'. To perform tilting, equal and opposite voltages are quickly ($< 1\mu$sec) applied to 2 wall sectors separated in θ by π. The speed of the voltage rise time, relative to the $l = 1$ period, gives rise to a substantial amplitude $l = 1$ wave after the voltages have reached their maximum value. The combination of the $l = 1$ motion and the voltage perturbations results in fast radial transport of electrons. This transport results in a smoothing of the density profile and a quieting of density fluctuations. The speed of the transport is dependent on the length of the column, and on the amplitude of the $l = 1$ wave present. The smoothing and quieting is qualitatively similar to that given by magnetic tilt [26], but faster by a factor of ten. After the desired density profile is achieved, the perturbation is turned off and the $l = 1$ wave damped before further manipulations. Other manipulations, such as multiple column creation and adjustment of initial column positions, will be described later.

After the initial condition is created, an experiment phase takes place during which a desired evolution time t is allowed to elapse. Because measurements of the charge induced on the wall sectors, Q_{sector}, are relatively non-perturbative, observations of Q_{sector} allow the evolution of the system to be monitored non-destructively.

In the dump phase, the containment voltage on the dump gate is quickly (~ 0.1 μsec) brought to ground, and the electrons stream out to either be collected on the collimator plate, or to pass through the collimator hole and be collected on the charge collector in the analysis region. By measuring the voltages induced on these collectors, and knowing their capacitances, the charge dumped on them can be obtained. For example, the total number of electrons within the trap, N_e, is the sum of the charge dumped on the collimator plate and charge collector. In the

next sections, I describe how electron density and temperature distributions can be determined.

2.4 Density Measurements

The 3D electron density at a particular time, $n_e(r, \theta, z)$, is diagnosed with both Gauss' law measurements of the total charge within a conducting cylinder, and with measurements of the charge that after dumping flows along B_z and through a collimator hole at the end.

2.4.1 Gauss' Law Measurements

The line density $N_{Le}(z)$ of a density distribution $n_e(r, \theta, z)$ is defined by

$$N_{Le}(z) \equiv \int_0^{R_w} dr \int_0^{2\pi} r \, d\theta \, n_e(r, \theta, z) \, . \tag{2.1}$$

Use of equation 2.1 requires precise knowledge of $n_e(r, \theta, z)$, however. The Gauss' law measurement measures the total image charge induced on an interior cylinder to obtain a quick determination of the average N_{Le} of a 3D column about its middle, i.e. $z = 0$.

To obtain this image charge measurement, a central cylinder is switched to a high impedance amplifier. Since the cylinder was connected to ground previously, the charge of the plasma within, Q_{cyl}, is balanced by positive image charge on the cylinder. After the cylinder is switched, it is only capacitively coupled to ground. Its capacitance C_{cyl} is the sum of the capacitance of the lead connected to the cylinder and the distributed capacitance of the cylinder to ground, and is known. When the plasma is dumped, the cylinder's voltage drops by a value $V_{Gauss} = Q_{cyl}/C_{cyl}$. Careful calibration of the amplifier gains and of the capacitances yields measurements of Q_{cyl} accurate to $\sim$1%. The Gauss' law line density is then given by

$$N_L \equiv \frac{Q_{cyl}}{-e L_{cyl}} \text{ (electrons/cm)} \, . \tag{2.2}$$

This line density is used with the total number N_e to define a column length L_p:

$$L_p \equiv \frac{N_e}{N_L} \,. \tag{2.3}$$

2.4.2 Radial Density Profile Measurements

Taking many density measurements with the collimator hole at different positions permits a density profile $n(r)$ to be constructed at any desired evolution time. The basic measurement is the charge $Q_{coll}(r,\theta)$ which flows along B_z through the collimator hole of area $A_h = 7.94\,\mathrm{mm}^2$. This is the z integral of the plasma density:

$$Q_{coll}(r,\theta) = -eA_h \int dz\; n_e(r,\theta,z)\;, \tag{2.4}$$

where $-e$ is the electron charge.

The possible collimator hole positions are limited by the geometry to an arc which transects the trap axis. Thus, the hole can be rotated to any radial position, but only two θ-positions are available at each r. When the density profile is θ-symmetric this restriction does not matter, and it is straightforward to construct 'radial profiles' consisting of $Q_{coll}(r)$. An example of such a radial profile is figure 3.19. A z-averaged density is then obtained as $n(r) \equiv -Q_{coll}(r)/eA_hL_p$.

In order to image densities in both r and θ, however, it is necessary to do the scanning in θ by varying the θ-phase of the electron column at the time of the dump. The technique to make plots of $Q_{coll}(r,\theta)$ at arbitrary θ requires that the plasma within the trap be rotating about the axis with a single frequency. This produces a voltage signal on the sector probe at the same frequency (plus harmonics, which can be filtered out). By triggering a computer-controlled pulse delay generator off a specific phase of the signal, and then delaying a specific fraction of a period before the dump, any desired θ-position of the density distribution can be set [26], and phased-locked 2D density plots can be constructed out of measurements of many identically evolving plasmas.

3D Density Distributions

If the density profile's temperature is known, it is in principle straightforward to calculate 3D density $n_e(r,\theta,z)$ and potential $\phi_e(r,\theta,z)$ distributions from $Q_{coll}(r,\theta)$. In my data analysis, I have often used a code which does this calculation for θ-symmetric densities [26]. Assuming θ-symmetry, and that the plasma maintains a Boltzmann distribution along each field line, Poisson's equation becomes

$$\nabla^2\phi_e(r,\theta,z) = 4\pi e n_e(r,\theta,z) = 4\pi e n_0(r) \exp\left(\frac{e\phi_e(r,\theta,z)}{k_B T(r)}\right) , \tag{2.5}$$

with boundary conditions

$$\begin{array}{lll} \phi_e(R_w,\theta,z) = 0 & \text{for} & -L_c/2 < z < +L_c/2 \\ \phi_e(R_w,\theta,z) = V_c & \text{for} & L_c/2 <\mid z \mid \end{array}$$

where L_c is the length of the containment cylinders. The code uses an iterative technique to find a function $n_0(r)$, and hence $n_e(r,\theta,z)$ and $\phi_e(r,\theta,z)$, which satisfies both Eq. 2.5 and Eq. 2.7. The solution also yields the 3D electrostatic energy $\mathcal{H}_{\phi e}$ of the column from:

$$\mathcal{H}_{\phi e} = \frac{1}{2}\int n_e(r,\theta,z)\phi_e(r,\theta,z)\; r\; dr\; 2\pi\; dz\; . \tag{2.6}$$

2D Density Distributions

Given the length L_p of the column from the Gauss' law measurement, I define a z-averaged 2D electron density $n(r,\theta)$ by

$$n(r,\theta) \equiv \frac{Q_{coll}(r,\theta)}{-eA_h L_p}\; . \tag{2.7}$$

With Poisson's equation, $\nabla^2\phi = 4\pi n e$, a 2D potential $\phi(r,\theta)$ can be calculated. The 2D electrostatic energy $\mathcal{H}_\phi$ is given by

$$\mathcal{H}_\phi = \frac{1}{2}\int n(r,\theta)\phi(r,\theta)\; r\; dr\; 2\pi\; . \tag{2.8}$$

These 2D quantities are important in my data analysis, as it is often not necessary (or possible) to generate the full 3D density distribution.

2D Density Plots

Figure 5.2 is an example of a phase-locked 2D plot of $n(r, \theta)$. This plot also has dots indicating the points at which density measurements were taken, and a circle which indicates the collimator hole size. The 2D plots in this dissertation have all been produced with the same format: there are 6 solid contours linearly increasing from zero to the maximum density, with 4 grey scales between the solid contours. Thus, the lowest grey scale indicates densities between noise and 4.2% of the peak density. This format does a good job of revealing the details in the data, but note that at large density gradients only the solid contours are apparent. The noise of the density measurements is typically $\sim 0.1\%$ of the peak density. I calibrate the density scale by indicating, in the caption, the density between solid contours.

2.4.3 Sector Probe Signals

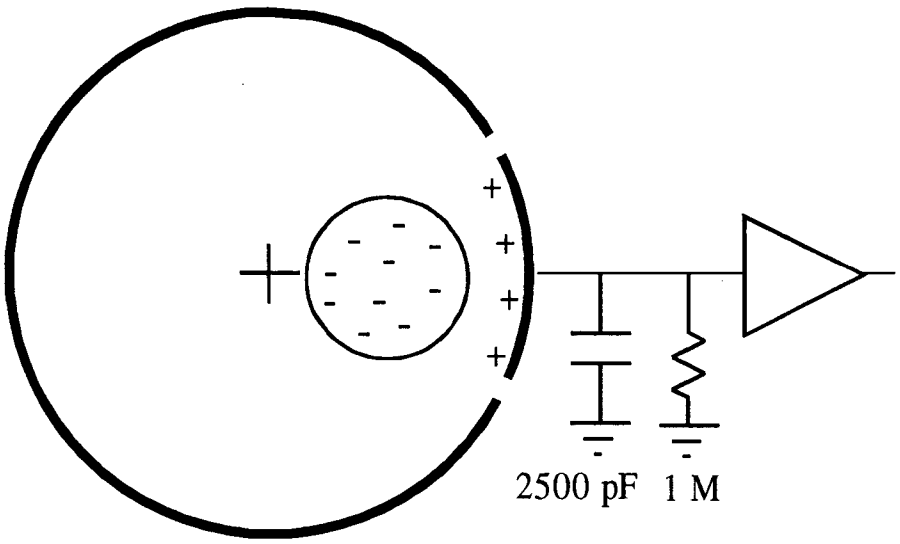

Figure 2.2: Schematic diagram of the circuit connected to a sector probe.

The charge induced on the 60° wall sector probes reveals much about the dynamics of the confined electron plasma. I measured the induced charge with the circuit shown in figure 2.2. High-impedance amplifiers were used exclusively,

to give a capacitive coupling to the sector. Some previous work on non-neutral plasmas [15, 38] used low-impedance (i.e. resistively coupled) amplifiers; however, high-impedance amplifiers signals provide much greater signal-to-noise ratios and are easier to interpret. The internal capacitance of the sectors is $\approx$ 300 pF, and thus including the added C = 2,500 pF and R = 1 MΩ, the real part of the impedance is given by:

$$|Z| = \frac{R}{(1+\omega^2 R^2 C^2)^{\frac{1}{2}}} \approx \frac{1}{\omega C} \tag{2.9}$$

The approximation of the second term is a good one since $1 << \omega^2 R^2 C^2 = 310$ at 1 kHz, which is the lowest frequency of interest. The voltage measured on the sector is then simply proportional to the amount of charge induced on it: $V_{sector} = Q_{sector}/C$.

The sector probe signals $V_{sector}(t)$ obtained from electron columns with finite $(r-\theta)$ area are observed to be very similar to those that would be induced by 'line' charges with zero $(r-\theta)$ area. This is because the electric field outside a circular column is identical to that of a line charge of the same N_L positioned at the column's center. It has been observed that the narrow electron columns used in this work are usually quite circular. A knowledge of the Q_{sector} induced by a line charge, as a function of its position, is therefore useful. The calculation of this is straightforward since the method of images can be used in this cylindrical geometry to easily obtain the electric field at any point.

The image charge density (per unit length) on the conducting wall is proportional to the electric field $E(R_w, \theta)$, and an integral over the sector probe's angular width then gives the total induced charge per unit length. For a sector with angular width $\Delta\theta$ and center at $\theta = 0$, the charge induced by a line charge of density N_L and position (d, θ) is:

$$Q_{sector}(d, \theta, N_L) = \frac{N_L e}{\pi}\left(\arctan\left(\frac{(1+d)\sin(\theta+\frac{\Delta\theta}{2})}{(1-d)\left(1+\cos(\theta+\frac{\Delta\theta}{2})\right)}\right)\right.$$

$$+\arctan\left(\frac{(1+d)\sin(\theta-\frac{\Delta\theta}{2})}{(1-d)\left(1+\cos(\theta-\frac{\Delta\theta}{2})\right)}\right)\Bigg). \qquad (2.10)$$

Here, d is the normalized displacement of the column from the axis, i.e. $d \equiv D/R_w$. (Note that as a convention I define length variables normalized to the wall radius to be the lower-case versions of the unnormalized variables.)

An alternative expression can be obtained from an integration of the Kapetanakos and Trivelpiece [38] result for the current induced on a sector probe, when the right hand side of their Eq. 22 is corrected with a multiplication by 2 [26]. This gives the equivalent result:

$$Q_{sector}(d,\theta,N_L) = \frac{N_L e\Delta\theta}{2\pi} + \frac{2N_L e}{\pi}\sum_{l=1}^{\infty}\sin\left(\frac{l\Delta\theta}{2}\right)\cos(l\theta)\frac{d^l}{l}. \qquad (2.11)$$

The sector probe signals are easy to interpret in terms of the dynamics of the electron column(s) inducing them. When only one vortex is contained, it either remains on axis – resulting in no signal – or is displaced from the axis, where interactions with its image produce a circular orbit about the axis at the l=1 diocotron frequency $f_{l=1}$ [26]. The θ-variation, for all displacements, is thus $\theta(t) = 2\pi f_{l=1}t$.

At small column displacements, $V_{sector}(t)$ is simply a sinusoid at the fundamental l=1 frequency, due to the d^l amplitude dependence of the harmonics (see equation 2.11). As d is increased the harmonics appear, but with capacitive coupling these are in phase with the fundamental. (When the sector is resistively coupled, the phases of the harmonics are a function of frequency, and interpretation becomes harder.) In figure 2.3 I show observed $V_{sector}(t)$ signals generated by a single column at three different displacements, along with the waveform predicted by the equations 2.10 and 2.11.

Fine [26] has previously shown that measurements of the induced current for various displacements d from the axis of an electron column are in good agreement with the predictions of Kapetanakos and Trivelpiece [38]. I have found similarly

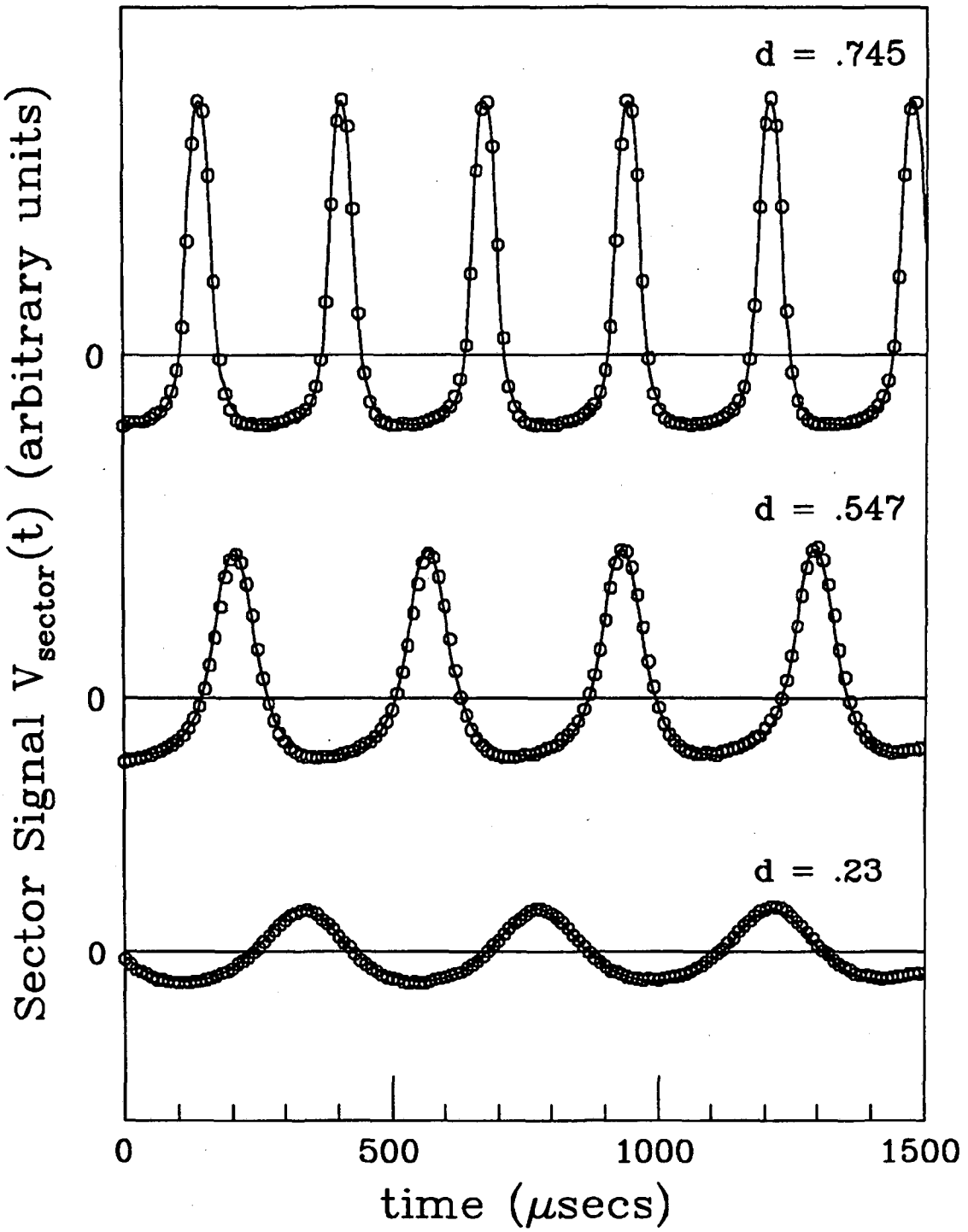

Figure 2.3: Measured (o) and predicted (—) waveforms for three normalized displacements, $d = .745$, .547 and .23. The predicted waveforms were generated from Eq. 2.11, using values of N_L and d from a fit of the waveform.

good experimental agreement with the predictions of equations 2.10 and 2.11 and measurements of induced charge. I therefore routinely use measurements of V_{sector} to measure displacement. Equation 2.11 gives for the ratio of the fundamental's amplitude $A^{(1)}_{l=1}$ and the first harmonic's amplitude $A^{(2)}_{l=1}$ the relation

$$\frac{A^{(1)}_{l=1}}{A^{(2)}_{l=1}} = \frac{\sin(\Delta\theta/2)\, d}{\sin(\Delta\theta)\,(d^2/2)} = \frac{1.154}{d}, \tag{2.12}$$

using $\Delta\theta = 60°$. Since these amplitudes can be measured from a Fourier transform of a single $V_{sector}(t)$ waveform, this way of measuring the column displacement d is much faster than the alternative method of creating a density plot of $n(r,\theta)$.

When more than one column is present, the wall charge signal will (from the superposition principle) be the sum of the signals that either column generates. Thus, even when the dynamics of the motions are more complicated, a picture of how the columns are moving can be deduced from the signal. Examples of such signals and their interpretation are given in Appendix B. A quantitative method of analysis, currently under development, obtains the positions of several contained columns from instantaneous V_{sector} measurements taken from many different sectors. For n columns there are 2n free variables (the position coordinates), which suggests that the simultaneous measurements of 2n different V_{sector} signals can yield the positions of the columns at each point in time that the signals are digitized. Problems arise from symmetries and measurement noise, however, so more independent sector signals are required to obtain reliable position data.

2.5 Temperature Issues

As will be discussed in section 2.8, the dynamics of electron columns are often well-described by equations of motion isomorphic to the 2D Euler equation. This isomorphism breaks down, however, when the columns have different parallel temperatures. Since most manipulations of the columns produce some change in

their temperatures, it is important to have an ability to measure temperature, and to predict how temperatures will change during manipulations. In this section, I describe the various temperature diagnostics available on the EV apparatus, and detail how some commonly used manipulations heat or cool the plasma.

2.5.1 Perpendicular Temperature Measurements

The $T_\perp$ diagnostic on the EV apparatus operates by measuring the change in the parallel energy of the dumped electron when a secondary magnetic field causes some perpendicular energy to be transferred to the parallel direction. This is commonly called a 'magnetic beach' analyzer [37]. After the end gate has been lowered, the plasma expands ('disassembles') towards the collimator. During this disassembly, the plasma electrostatic energy increases the parallel velocities in a complicated fashion. However, since the time for a gyro orbit ($\sim$ 1 nsec) is small compared to the disassembly time ($\sim 1\mu$sec), the gyromagnetic moment $\mu = mv_\perp^2/2B_z$ is conserved, and the collimated beam that passes through the hole enters the analyzer region with its perpendicular energy distribution unchanged.

The collimated beam then encounters a potential barrier caused by the secondary magnetic field B_s of the analyzer solenoid. Since the space charge of the diffuse beam is small, each electron conserves its total kinetic energy $\mathcal{H}_\perp + \mathcal{H}_\parallel = \frac{1}{2}m(v_\perp^2 + v_\parallel^2)$ as well as the gyromagnetic moment. In order to conserve both quantities, the average parallel energy must change by $\Delta\mathcal{H}_\parallel = -(B_s/B_z)k_BT_\perp$ within the analyzer solenoid. This change is parallel energy is measured by applying retarding voltages to the analyzer electrodes. If an electron's $v_\parallel$ drops low enough, it will not make it through cylinder A3. By measuring the density collected at the end as a function of the voltage on A3, and repeating with different B_s values, the perpendicular energy distribution can be constructed to $\sim$ 5% accuracy.

2.5.2 Parallel Temperature Measurements

In many of the experiments of this dissertation, it was important to measure the parallel temperature $T_{||}$ of two columns to ensure that they had the same value. A $T_{||}$ diagnostic has been developed for Malmberg-Penning traps [23], which obtains the temperature from measurements of the number of electrons sufficiently energetic to escape past the end confinement potentials. However, this approach doesn't work for off-axis columns, since it requires that the columns being measured be stationary for times longer than a diocotron period.

A different way of measuring $T_{||}$ is to measure $T_{\perp}$ at the time of interest, and also to measure the final temperature $T_{\perp eq}$ after the two temperatures have equilibriated. As described by Hyatt [37], temperature anisotropies relax on a collisional timescale. Due to the conservation of thermal energy on the millisecond collisional timescale, $T_{||}, T_{\perp}$ and $T_{\perp eq}$ are related by

$$T_{||} + 2T_{\perp} = 3T_{\perp eq} \tag{2.13}$$

While this method yields accurately calibrated temperatures, it requires a great deal of time – typically, 15 minutes for each temperature measurement. Therefore, when creating an initial condition of two columns which had to have the same (arbitrary) $T_{||}$, I used a method based on observations of the $T_{||}$-dependent finite-length contributions to the l=1 frequency. This fast method will be discussed in section 3.2.1.

2.5.3 Cooling/Heating from Expansions/Compressions

The electron column cools during a slow axial expansion of the column, and heats during a slow compression [37]. 'Slow' is relative to the time $\tau_{bounce} \equiv 2L_p/v_{||}$ it takes for an electron to 'bounce' once in $\hat{\mathbf{z}}$. This results in the axial bounce adiabatic invariant $I_{||} \equiv \oint v_{||}\, dz$ remaining a constant, as the electrons exchange energy with

the confinement power supplies. A useful first order estimate of the new temperature $T'_{\|}$ as a function of initial and new plasma lengths is given by:

$$T'_{\|} \approx T_{\|}\left(\frac{L_p}{L'_p}\right)^2 . \tag{2.14}$$

2.5.4 Cascade Heating

I have often found it necessary to let a column expand beyond a 'cut' gate into an electrode at ground potential. This manipulation, which I term 'cascading', results in both adiabatic expansion and disassembly expansion of the column. Figure 2.4 shows a schematic of the process. A single plasma is confined in cylinder L3 by potentials on an end gate and on a 'cut' gate L4. Cylinder S, on the other side of the cut gate, is at ground. When the cut gate is lowered, the plasma will initially expand adiabatically into L4. When the cut potential is low enough, however, some electrons will no longer be confined and will cascade into L3. This process does not preserve the adiabatic invariant $I_{\|}$, and some of the electrostatic energy of the column will go into the $v_{\|}$ of the escaping electrons. As the cut lowering continues, more plasma spills over until ultimately L4 is at ground and the column is confined in L3-S. The final state has had a mix of adiabatic cooling and electrostatic heating of the parallel velocities.

Density transport can also occur during this cascading. A column being cascaded is often off-axis, so there are no symmetries during the cut, and the dissimilar θ-direction drifts on the two sides of the cut gate can result in a changed final density profile.

Cascade heating has been experimentally studied with a single on-axis column, and in Appendix A I discuss this study in depth. My main conclusions are:

- The amount of adiabatic cooling or cascade heating caused by expansion of a column into a cut gate depends on the speed of the cut gate lowering time τ_{cut},

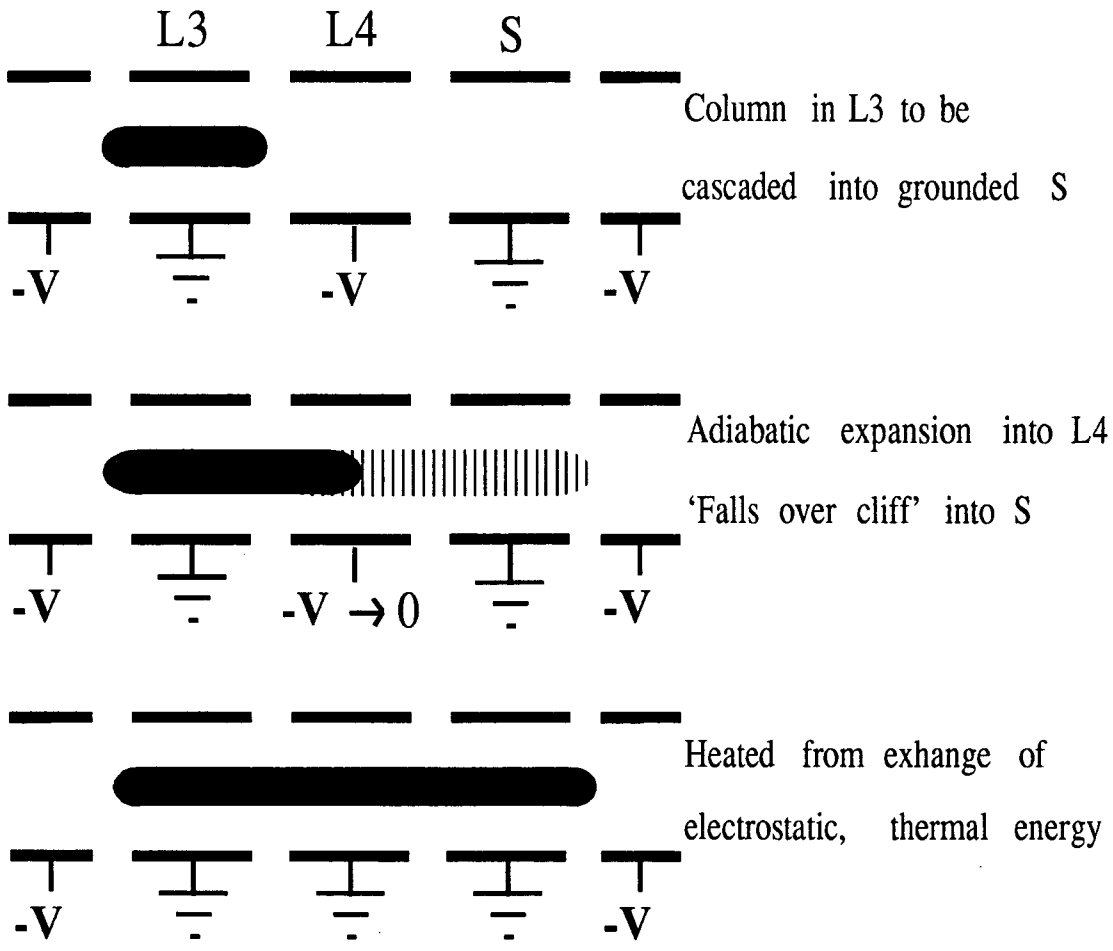

Figure 2.4: Schematic of expansion into a grounded electrode, which will result in cascade heating.

relative to τ_{bounce}.

- For the column expansion past the cut gate, the amount of heating can be predicted from energy conservation of the electrostatic and thermal energies.
- The presence of another column on the opposite side of the cut gate, at a different θ-position, is estimated to lower the amount of cascade heating done by $\sim 10\%$.
- Density transport from cascading can be reduced by decreasing τ_{cut}, although

the transport can not be made negligible.

2.6 Transport Issues

In this section, I briefly review some of the results of previous experiments on plasma transport in Malmberg-Penning traps. It is useful to conceptually divide transport into externally-induced transport (where external torques cause non-conservation of angular momentum), and internal transport.

2.6.1 Angular Momentum Conservation

Non-neutral plasmas have exceptional confinement properties, as compared with neutral plasmas. One reason for this is that angular momentum conservation strongly constrains the radial transport [52]. The total canonical angular momentum $\mathcal{P}_\theta$ is the sum of a mechanical and a vector potential contribution:

$$\mathcal{P}_\theta = \sum_j \left[m_e V_{\theta j} R_j \quad + \quad \frac{eB_z}{2c}\left(R_w^2 - R_j^2\right)\right] , \tag{2.15}$$

where R_j is the distance of particle j from the axis, $V_{\theta j}$ is its velocity in the θ-direction, m_e is its mass, and the summation is over all particles. In my experiments, the mechanical contribution (first term) is $\sim 10^4$ times less than the electromagnetic part, and can be neglected. If there are no external couplings applying torques and hence changing the angular momentum, the constraint on radial positions is then $\sum_j R_j^2 =$ constant, which implies that only a fraction of the contained electrons can reach the wall and be lost.

$\mathcal{P}_\theta$-conservation does not necessarily constrain the rate of expansion of an off-axis column's radius. This is because $\mathcal{P}_\theta$-conserving processes can result in the column expanding its radius while simultaneously moving closer to the axis. Experimentally, I have found that the rate of radius expansion dramatically increases when the column is off-axis (section 3.2.2).

2.6.2 Externally-Induced Transport

The operating parameters of the EV apparatus result in negligible couplings with processes known to cause transport. These processes include electron-neutral collisions [15], electromagnetic radiation [53] and finite wall resistances [71]. The remaining observed transport is known as 'anomalous' transport, and is believed caused by couplings with the small intrinsic electrostatic or magnetostatic field errors of the apparatus. Applied field errors are well known to cause transport [25, 24]. EV was designed with the goal of minimizing field errors in mind, and has anomalous transport rates about 25 times less than those of the prior V′ apparatus [19].

2.6.3 Internal Transport

When the external couplings are small enough, electron-electron interactions will result in an on-axis plasma evolving to a confined thermal equilibrium before appreciable expansion of the column radius. This transport to global thermal equilibrium has been experimentally studied [60, 20], and the equilibration time was found to scale roughly as B^2 for monotonic profiles, and as B^1 for short non-monotonic profiles. These scalings are in general agreement with the predictions of theory [54, 22].

When the plasma is unstable, however, much faster cross-field transport takes place (100 μsecs instead of seconds). Examples of such instabilities are the vortex pairing instability (see section 4.5.1 and the Kelvin-Helmholtz shear-flow instability [16].

2.7 Transport and Equilibration Timescales

The electron plasma has kinetic times, such as the time for an axial electron oscillation, τ_{bounce}, which determine the times required for equilibriation or trans-

port. Here I give expressions for these times scaled to the typical parameters of my experiments, and then relate them to the time for approach to equilibrium.

The fastest time is that for an electron to make a cyclotron orbit about a field line, τ_c:

$$\tau_c \equiv \frac{2\pi mc}{eB} = 10^{-9}\text{secs}\,\left(\frac{375\,\text{G}}{B}\right)\,. \tag{2.16}$$

The time for an electron to 'bounce' once axially through the column of length L_p is

$$\tau_{bounce} \equiv \frac{2L_p}{v_{||}} = 1\,\mu\text{sec}\,\left(\frac{L_p}{20\text{cm}}\right)T_{||}^{-1/2}\,. \tag{2.17}$$

Here, $T_{||}$ is measured in electron volts. The electron column will rotate about its $\hat{\mathbf{z}}$ axis due to $\mathbf{E}\times\mathbf{B}$ drifts arising from its self electric field. At the low densities of these experiments, a column of uniform density n_e will have a rotation time of

$$\tau_{rotation} \equiv \frac{B}{nec} = 5.2\,\mu\text{sec}\,\left(\frac{B}{375\,\text{G}}\right)\left(\frac{5\times10^6\text{cm}^{-3}}{n}\right)\,. \tag{2.18}$$

Finally, the time between electron-electron collisions [4], τ_{ee}, is

$$\tau_{ee} = 6.8\,\text{msecs}\;T^{3/2}\left(\frac{5\times10^6\text{cm}^{-3}}{n}\right)\,. \tag{2.19}$$

We can use these timescales to characterize the approach to equilibrium. Suppose an electron column with no initial symmetries has just been contained by the close of the inject gate electrode. The $(\theta - z)$ motions will quickly smooth over the bulk of the $(\theta - z)$ density asymmetries through passive scalar advection, leaving intact only those perturbations corresponding to stable modes or nonlinear coherent structures [36]. Thus, the column will symmetrize in $n(z)$ on a timescale of $\sim 10\,\tau_{bounce}$, and in $n(\theta)$ in $\sim 10\,\tau_{rotation}$, perhaps leaving behind plasma or diocotron waves which will damp on slower timescales.

The temperature distributions $T_{||}(\theta,z)$ and $T_{\perp}(\theta,z)$ will similarly be symmetrized by this passive scalar mixing. These separate temperature distributions will

then relax to an equilibrium distribution T_{eq} on a collisional timescale of several τ_{ee} [37].

Relaxation of monotonically decreasing density profiles $n(r)$ to the confined thermal equilibrium profile is much slower. Theory [54] predicts an equilibration time τ_{eq}, from transport steps caused by binary interactions, going roughly as

$$\tau_{eq} = 0.68\text{sec}\ T^{-1/2} \left(\frac{B}{375\,\text{G}}\right)^2 D_{mm}^4\ , \tag{2.20}$$

where D_{mm} is a typical length for the radial asymmetry, in millimeters. Only preliminary experiments have been done on this process to date, but a magnetic field dependence of $B^{2\pm.5}$ has been found, in agreement with the predicted scaling [31].

Finally there is the 'anomalous' transport believed caused by the small but inevitable electrostatic field errors present in the apparatus. Anomalous transport has been quantified by measuring the 'mobility' time, τ_m, required for the central density of an on-axis column to decrease by a factor of two. Driscoll, Fine and Malmberg found that τ_m scales as $(L_p/B_z)^{-2}$ over five decades in L_p/B_z, with one decade of scatter. The best slope-2 logarithmic fit to the EV data gave

$$\tau_m = 110\,\text{sec} \left(\frac{B}{375\,\text{G}}\right)^2 \left(\frac{20\text{cm}}{L_p}\right)^2\ . \tag{2.21}$$

2.8 Drift Dynamics and the Fluid Analogy

The electron dynamics are observed to be well approximated by 2D guiding center theory. The dynamics are 2D because the axial bouncing of the individual electrons averages over any z variations at a rate fast compared to $r-\theta$ variations; typically, $\tau_{rotation} > 5\tau_{bounce}$. Guiding center theory is valid because the gyroradius (typically ~ 30 microns) is smaller than the other lengths of the system. Deviations caused by finite-length effects will be discussed in section 3.2.1, but these effects are observed to result only in the 2D dynamics taking place in a rotating frame rather than the lab frame.

Using the 2D approximation, the unneutralized electron charges give rise to electrostatic potentials $\phi(r,\theta,t)$ through Poisson's equation, $\nabla^2\phi = 4\pi en$. These potentials result in cross-field drifts, given by

$$\mathbf{v}(r,\theta,t) = -c\nabla\phi \times \hat{\mathbf{z}}/B_z \; . \tag{2.22}$$

These velocities are well defined even where there are no electrons. Taking the curl of the velocity gives the vorticity Ω:

$$\Omega \equiv \nabla \times v \quad = \quad \nabla^2\phi\frac{c}{B}\hat{z} \quad = \quad n\frac{4\pi ec}{B}\hat{z} \; . \tag{2.23}$$

The vorticity of the electron system is thus proportional to the density. Using this fact, the continuity equation is also a statement that the convective derivative of the vorticity is zero, which is an evolution equation for the system:

$$\frac{\partial\Omega}{\partial t} + v \cdot \nabla\Omega = 0 \; . \tag{2.24}$$

These 2D drift-Poisson equations are isomorphic to the 2D Euler equations for an inviscid fluid of uniform density ρ [41, 5, 17]. This is displayed in Fig. 2.5. The electric potential ϕ is analogous to the streamfunction ψ, and the drift velocity analogous to the fluid velocity. The momentum equation for fluids gives the same evolution equation for the system, and the boundary conditions are also equivalent, namely ϕ = const and ψ = const on the walls. Thus, an initial distribution of electrons $n(r,\theta)$ in a cylinder, having vorticity $\Omega \propto n$, will evolve exactly the same as an identical initial distribution of vorticity $\Omega(r,\theta)$ in a uniform fluid.

There have been many experimental results which have shown striking quantitative agreement with predictions of fluid theory. These include prior observations of:

- elliptical distortions caused by wall interactions [28, 63],

and my observations of

2D Drift-Poisson

Poisson

$$\nabla^2\phi = 4\pi e n$$

E × B Drifts

$$\mathbf{v} = -\frac{c}{B}\nabla\phi \times \hat{z}$$

Vorticity

$$\zeta \equiv \nabla \times \mathbf{v}$$

$$= \nabla^2\phi \, \frac{c}{B}\, \hat{z}$$

$$= n \, \frac{4\pi e c}{B}\, \hat{z}$$

Continuity

$$\frac{\partial n}{\partial t} + \mathbf{v} \cdot \nabla n = 0$$

$$\frac{\partial \zeta}{\partial t} + \mathbf{v} \cdot \nabla \zeta = 0$$

2D Euler, ρ = constant

Stream Function

$$\mathbf{v} \equiv -\nabla\psi \times \hat{z}$$

Vorticity

$$\zeta \equiv \nabla \times \mathbf{v}$$

$$= \nabla^2\psi \, \hat{z}$$

Momentum

$$\frac{\partial \mathbf{v}}{\partial t} + \mathbf{v} \cdot \nabla \mathbf{v} = -\frac{1}{\rho}\nabla p$$

$$\frac{\partial \zeta}{\partial t} + \mathbf{v} \cdot \nabla \zeta = 0$$

electric potential	ϕ	$\leftrightarrow$	ψ	stream function
velocity	$\mathbf{v}$	$\leftrightarrow$	$\mathbf{v}$	velocity
density, vorticity	n, ζ	$\leftrightarrow$	ζ	vorticity

Figure 2.5: Isomorphism between the 2D drift-Poisson equations and the 2D Euler equations for a constant density fluid.

- symmetric vortex mergers [29, 48] (see section 4.5.1),
- stability of equilibria of two vortices [50, 34] (section 4.3),
- inviscid relaxation of distorted vortices via a decay instability [66] (section 3.2.3),
- l=3 surface wave instabilities of highly elliptical vortex structures [44] (section 3.2.4).

There are, of course, aspects of the 3D physical system which are not within the framework of the 2D fluid analogy, and plasma parameters where the analogy does not hold. These can result in discrepancies between the observations and the predictions of 2D fluid predictions. An example of a discrepancy is that Driscoll [16] has observed an exponentially growing $l = 1$ instability in a hollow column, where 2D fluid theory predicts only an algebraically growing instability. This has been attributed to temperature-independent shears caused by the axial variation of the 3D column [65].

Another discrepancy is that there are temperature-dependent drifts caused by finite-length effects. These drifts have been invoked by Peurrung and Fajans [57] to explain observations of abnormally low growth rates of the Kelvin-Helmholtz instability of an annular electron plasma [56]. The impact of the drifts on my experiments is discussed in section 3.2.1.

Peurrung and Fajans [57] have experimentally investigated the question of at which plasma parameters the finite-length drifts begin to produce deviations from 2D fluid predictions. They found that a fast azimuthal smearing of the plasma column begins to occur when $0.75 < \Lambda < 3.0$, where

$$\Lambda \equiv k\frac{\lambda_D^2}{R_v L_p}\,, \tag{2.25}$$

with R_v the radius of the column, λ_D its Debye length, and k a parameter near unity. I note that the parameter Λ was less than 0.1 for all of the experiments discussed in this dissertation, and that I did not observe any fast smearing of the columns.

Chapter 3

Single Vortex Studies

3.1 Overview

This chapter describes wave and transport experiments on a single confined electron column. Some of the phenomena have 2D fluid analogues, so the electron column will be referred to as a vortex when appropriate.

Low frequency plasma waves are observed on non-neutral columns [14]. For an infinitely long column, their dispersion relation is the same as that for a neutral plasma column except for a Doppler shift due to the $\mathbf{E} \times \mathbf{B}$ rotation [12]. They are characterized by potential perturbations of the form $\delta\phi = \psi(r)\exp(il\theta + ik_z z - i\omega t)$ [58]. The modes with $l \neq 0$ and $k_z = 0$, and thus $\delta\mathbf{E}$ perpendicular to $\mathbf{B}$, are known as the diocotron waves. Modes with $k_z \neq 0$ are called electron plasma waves.

Section 3.2 includes the results of experiments with diocotron waves. Diocotron waves have been the subject of years of experimental and theoretical study (see Davidson [13] and references therein). In fluid theory, the waves are known as Kelvin waves [43]. In their small amplitude limit, they are those 2D density perturbations whose $\mathbf{E}$-field and consequent $\mathbf{E} \times \mathbf{B}$ drifts self-consistently rotate the perturbation about the column (but always slower than the column's $\mathbf{E} \times \mathbf{B}$ rotation).

I first present some results on the l=1 diocotron wave, which is a special case among the diocotron waves. A $\cos(\theta)$ perturbation at small amplitude is equivalent

to displacing a rigid column a distance D off axis. The displaced column then orbits about the trap axis due to the **E**-field of the asymmetric image charges [26]. However, finite-length and temperature effects will in general be substantial. Fine has established that, to first order in displacement, these effects result in a constant frequency offset to the infinite-length $l = 1$ frequency [27, 28]. I have studied whether the frequency offset varies at large displacements, and find that within the experimental uncertainties, it does not (section 3.2.1).

The $l = 1$ wave is also different from $l \neq 1$ waves in that it is not susceptible to a spatial Landau-like damping where electrons in resonance with the wave are transported out [5, 14]. The reason for this difference is that the resonant point for the $l = 1$ is at the wall, where there is no density. However, there are other mechanisms which could cause it to damp. One recent theory is that 'rotational pumping' will result in an angular-momentum (P_θ) conserving expansion of the electron column's radius R_{rms}, giving an exponential damping of the displacement from the axis (i.e. the l=1 amplitude) [11].

In section 3.2.2, I present direct measurements of $R_{rms}(t)$ and $D(t)$ for a variety of experimental parameters. I find that while both P_θ-conserving and P_θ-nonconserving transport is taking place, the data is consistent with an exponential damping of the l=1. My measured rates are higher, however, than those crudely estimated for rotational pumping.

The $l \geq 2$ diocotron waves can be damped by the aforementioned resonance damping [14]. I have discovered, however, that small amplitude $l = 2$ and $l = 3$ waves, even when stable to resonance damping, are unstable to a decay instability. In this instability, the l mode wave decays to both an exponentially growing $l - 1$ 'daughter' wave and presumably to a resonant band of particles. When the decay instability is suppressed, by negative feedback on the daughter wave, exponential

damping on slow 'viscous' timescales is observed to occur (section 3.2.3).

A final new diocotron wave result is an observation that $l = 3$ perturbations on highly elliptical vortex structures can grow exponentially (section 3.2.4). This appears to be the first experimental observation of an instability predicted 100 years ago by Love [44].

In section 3.3 I describe the use of a phased electric field perturbation to drive electron plasma waves and couple angular momentum to and from the column. Eggleston, O'Neil and Malmberg [25] have previously demonstrated radial density transport with this technique, with the direction of the transport dependent on the characteristics of the induced plasma wave, but were not able to demonstrate a net $\sum_j R_j^2$ decrease. I have been able to cleanly demonstrate a transfer of angular momentum to the column, but have also found that the heating associated with the technique limits its usefulness.

In section 3.4 I describe an investigation of l=0 'sloshing' modes. These are z-dependent motions of electrons which occur when the magnetic field is not aligned with the confinement walls, and the image fields from the l=1 diocotron orbit of an off-axis column cause a time-dependent z-motion of the column density [33]. I have made a detailed study on the EV apparatus of the signals induced on the confinement rings by these modes, as a function of the misalignment of the magnetic field.

At large misalignments I see the features predicted for a single 'sloshing' mode [33]. At small misalignments, however, the signals from different rings lose coherence, suggesting the existence of local sloshing motions. As a consequence, I find that the magnet alignment given by minimizing the differential signal from the two end rings does not correspond to that given by plasma transport minimization. Better agreement with this latter alignment is given by minimizing the sum of the signal power off all the rings.

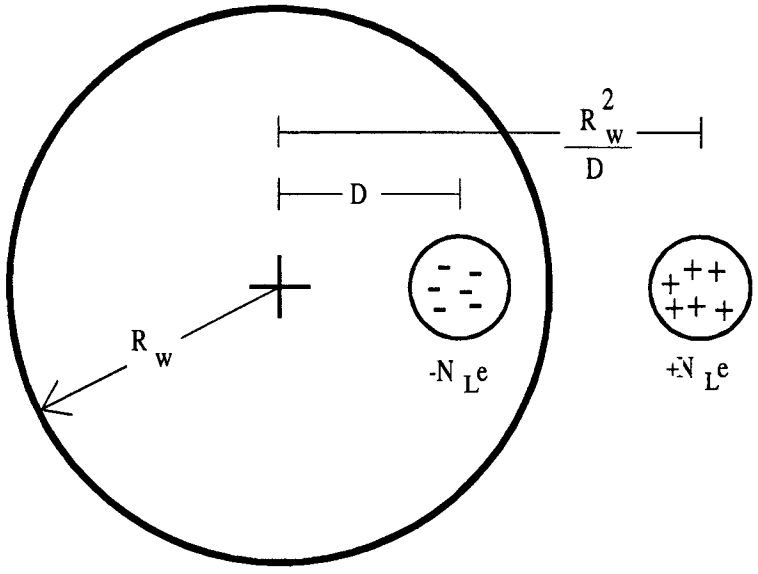

Figure 3.1: l=1 Diocotron Mode Coordinates

3.2 Diocotron Waves

3.2.1 l=1 Finite Length Effects

The l=1 diocotron is different from the other diocotron waves, in that it is much better modeled as the dynamical equilibrium of a displaced column than as a mode [26]. This permits an easy calculation of the effects of finite-length in $\hat{\mathbf{z}}$ [27].

Infinite Length $l = 1$ Diocotron

The variables of a diocotron mode are as shown in figure 3.1. A z-independent column of line density N_L and radius R_v is displaced a distance D from the axis of the containment walls. When the column remains circular, its field outside is that of a line charge at radial position D, and the image field is that of a line charge of opposite sign and the same N_L at radial position R_w^2/D. The electric field at the

column center is then

$$\mathbf{E}(r = D) \;=\; \frac{-2N_L e}{(R_w^2/D) - D}\hat{\mathbf{r}}\,. \tag{3.1}$$

The force $\mathbf{F}_{l=1}^{\infty}$ arising from the infinite length $l = 1$ image field, and the resultant drift velocity v_E from this force, are

$$\mathbf{F}_{l=1}^{\infty} = N_L \mathbf{E}_{l=1} \quad \text{and} \quad \mathbf{v}_E = \frac{c\,\mathbf{F}_{l=1}^{\infty} \times \mathbf{B}}{N_L e B^2}\,. \tag{3.2}$$

This gives for the infinite length l=1 frequency $f_{l=1}^{\infty}$:

$$f_{l=1}^{\infty} \;=\; \frac{c}{2\pi D}\frac{F_{l=1}^{\infty} \times B}{N_L e B^2} \;=\; \frac{cN_L e}{\pi B}\left[\frac{1}{R_w^2 - D^2}\right]\,. \tag{3.3}$$

Finite-Length Effects

Often, the predictions of equation 3.3 for $f_{l=1}^{\infty}$ and the measured $l = 1$ frequency $f_{l=1}$ are substantially different. The reason for this is that finite-length effects are often substantial, relative to the forces from the image field. A first order model for the finite-length effects have been developed by Fine [27]. The important effect, for columns with my experimental parameters, is a radial magnetron force which the electrostatic end fields exert in addition to, and proportional to, the axial confinement force. This radial force will produce drifts in the θ-direction which, like the axial force needed to contain the column, will have a component proportional to $T_{\|}$. The magnetron force for hot columns can be of the same order as image charge forces, and can thus result in very substantial increases to the $l = 1$ frequency, relative to the infinite-length prediction.

Happily (for the use of electron plasmas to study 2D interactions), the magnetron force is found to be, to first order in displacement, proportional to displacement. This is true both of the model and of experiments [27]. This proportionality suggests that finite-length effects will only produce an orbit of the column about the containment axis, at a constant frequency independent of D. Therefore, for any

general configuration of charges with the same $T_{||}$, the prediction of Fine's model is that the configuration will evolve as 2D vorticity would, only within a rotating frame produced by the magnetron motion.

Finite-Length Effects At Large Displacements

I have experimentally tested whether this result, that finite-length effects produce only a constant frequency orbit in $\hat{\theta}$, breaks down at large displacements. I find it to be valid out to displacements of $d < 0.73$. I moved a narrow ($R_v/R_w = .15$) and cold ($T_{||} \sim 0.25$ eV) column with an on-axis line density $N_L = 4.8 \times 10^6$ cm^{-1} to various displacements d, where its l=1 frequency $f_{l=1}$ and off-axis line density N_L were then measured. The measured d and N_L were then used in equation 3.3 to calculate the infinite length $f_{l=1}^{\infty}$, and the frequency shift $\Delta f_{l=1}$ due to finite length effects was thus known:

$$\Delta f_{l=1} = f_{l=1} - f_{l=1}^{\infty} \, . \tag{3.4}$$

I then repeated these measurements on a hotter ($T_{||} \sim 2.0eV$) and less dense ($N_L = 2.4 \times 10^6 \mathrm{cm}^{-1}$) column. I plot $\Delta f_{l=1}$ versus d, for both the hot and cold column, in figure 3.2. No strong dependence of the frequency shifts on displacement in the region $.36 < d < .73$ is seen.

Variations of Column Length vs. Displacement

The electron column changes its length L_p when it is moved to a different radial displacement. This is a finite-length effect due to the containment geometry of Malmberg-Penning traps. The reason for it can be seen in figure 3.3, which shows the vacuum confining potential surfaces. The cylinder walls are either at the confining potential V_c or grounded. The flat contour at the midplane between the grounded rings and the gate ring is at $V_c/2$ (as it must be, from the symmetry). Unless the

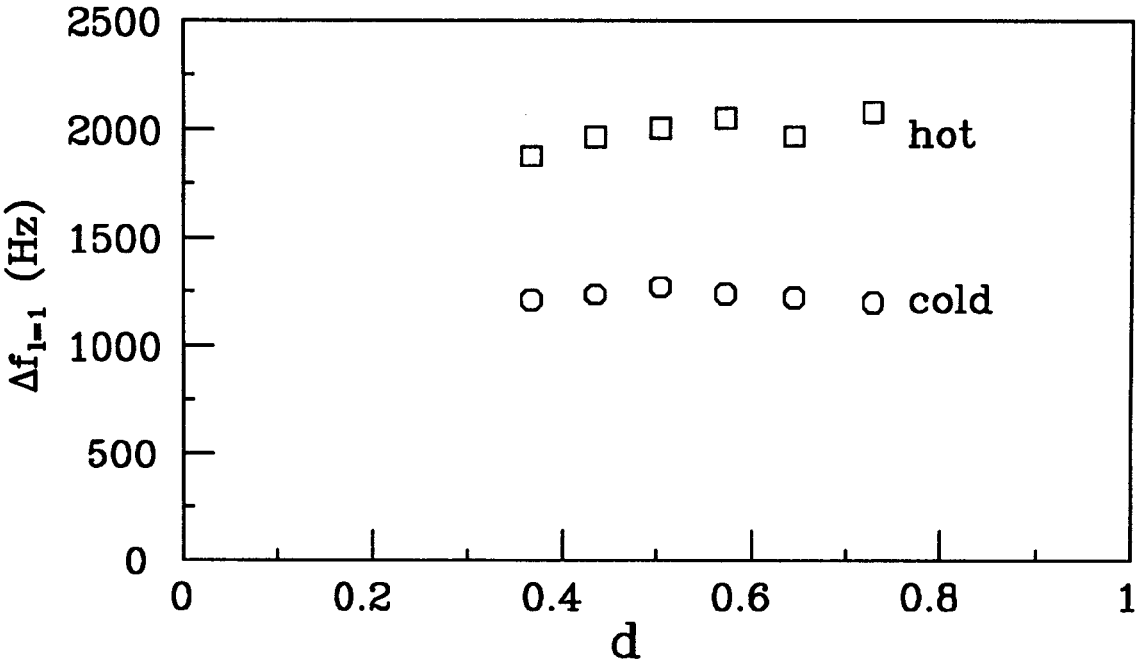

Figure 3.2: Finite length frequency shift $\Delta f_{l=1}$ for two parameters of N_L and T.

column is reflected at the potential $V_c/2$, it seems clear that L_p has to change as the column is displaced from the axis.

I have measured this effect by moving a column off axis and measuring its Gauss' law line density N_L, which gives L_p through equation 2.3. L_p versus d, for a column of on-axis length $L_p = 19.7$ cm, is shown in figure 3.4. To first order, the variation with displacement goes as d^2: the line is a plot of $1+.054d^2$, obtained from a fit. Since the confinement potential used here was close to the lowest possible without losses being observed, this resulted in the effect being small, with L_p increasing only about 4% at the largest displacements. Greater changes in L_p were observed to result when V_c was increased relative to V_{bias}. I generally used the lowest possible confinement fields in my vortex experiments to minimize this effect.

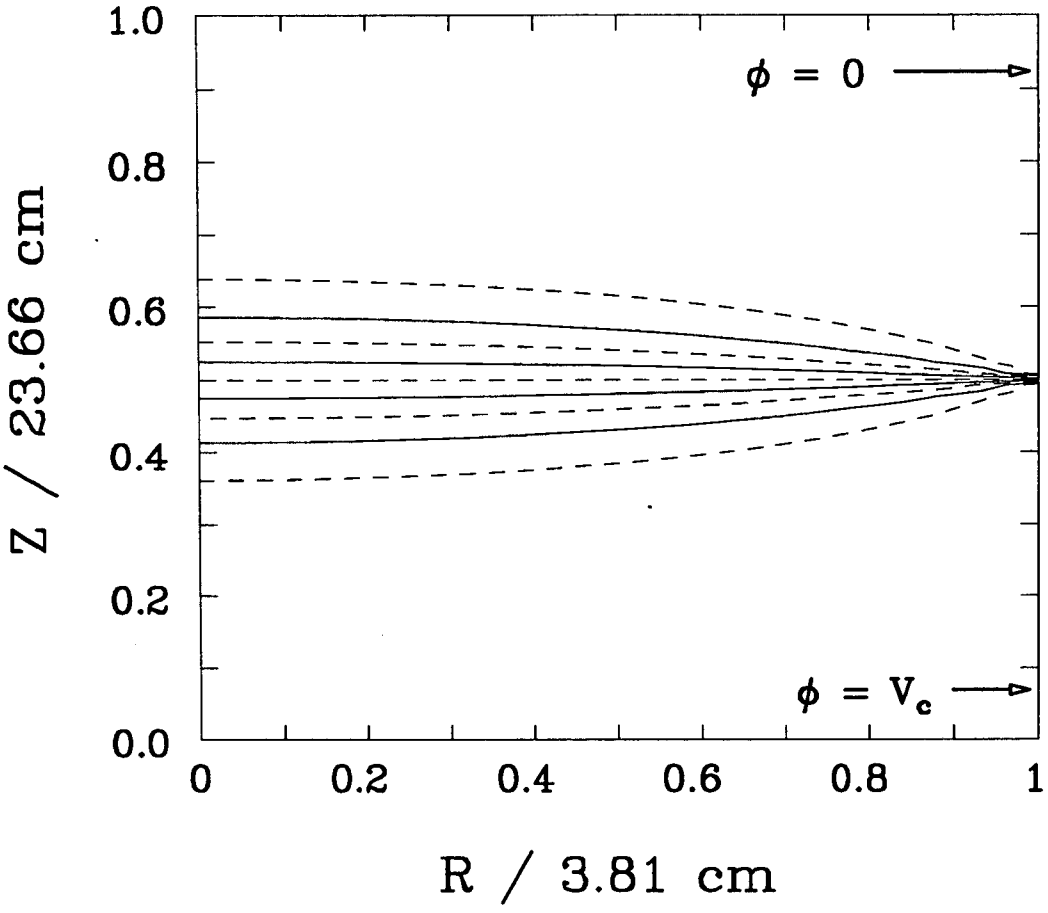

Figure 3.3: Confining potential surfaces within a Malmberg-Penning trap. The 10 potential contours are linearly spaced between 0 and V_c. There is no contained plasma.

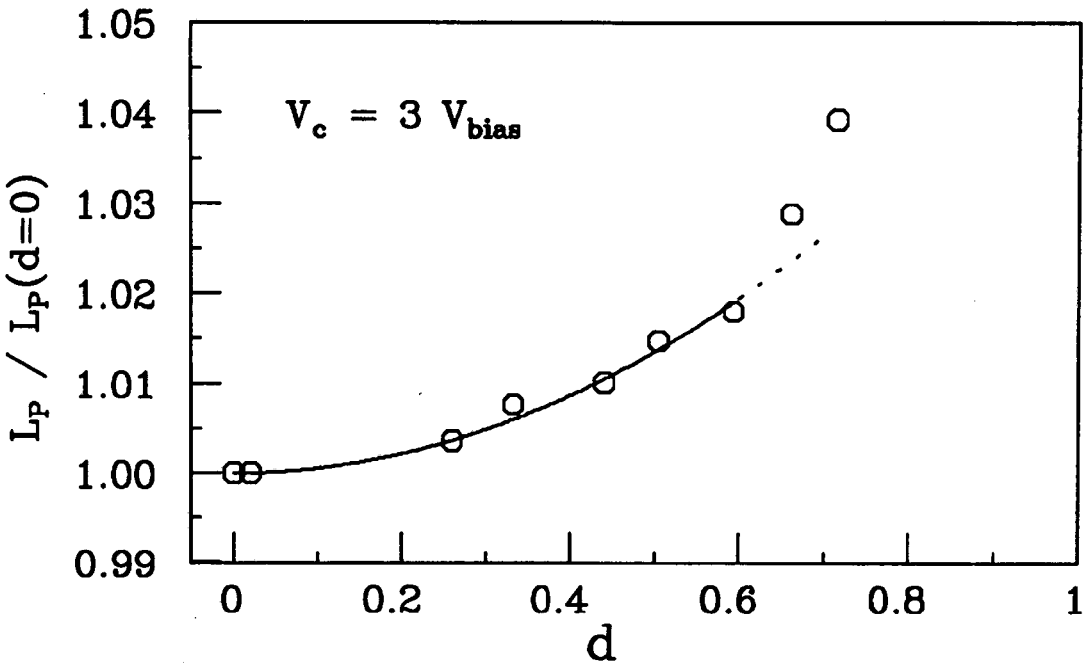

Figure 3.4: Measured Column Length L_p vs. Displacement, for V_c = -10V and V_{bias} = -3.3V. $L_p(0)$ =19.7 cm. The line is a fit to d^2.

3.2.2 Column Expansion and $l = 1$ Damping

An electron column in a Malmberg-Penning trap will be subject to various types of transport, which will result in a gradual expansion of its radius. This expansion is responsible for (among other things) limiting the lifetime of the two-column state (section 4.5.2). In this section, I present some direct measurements of the expansion, and establish that both P_θ-conserving and P_θ-nonconserving transport takes place. The transport rates are observed to be strongly dependent on the displacement D of the column from the axis.

Figure 3.5 shows column expansion taking place at a low magnetic field of B_z = 94 Gauss. The column was displaced from the axis to D = 1.35 cm., and a phase-locked $n(r,\theta)$ plot was taken of it. It was then contained for 100 msecs, and a second plot made using a phase-lock on the still-present $l = 1$ signal. As can be seen by eye, the column has expanded and moved slightly toward the axis during its

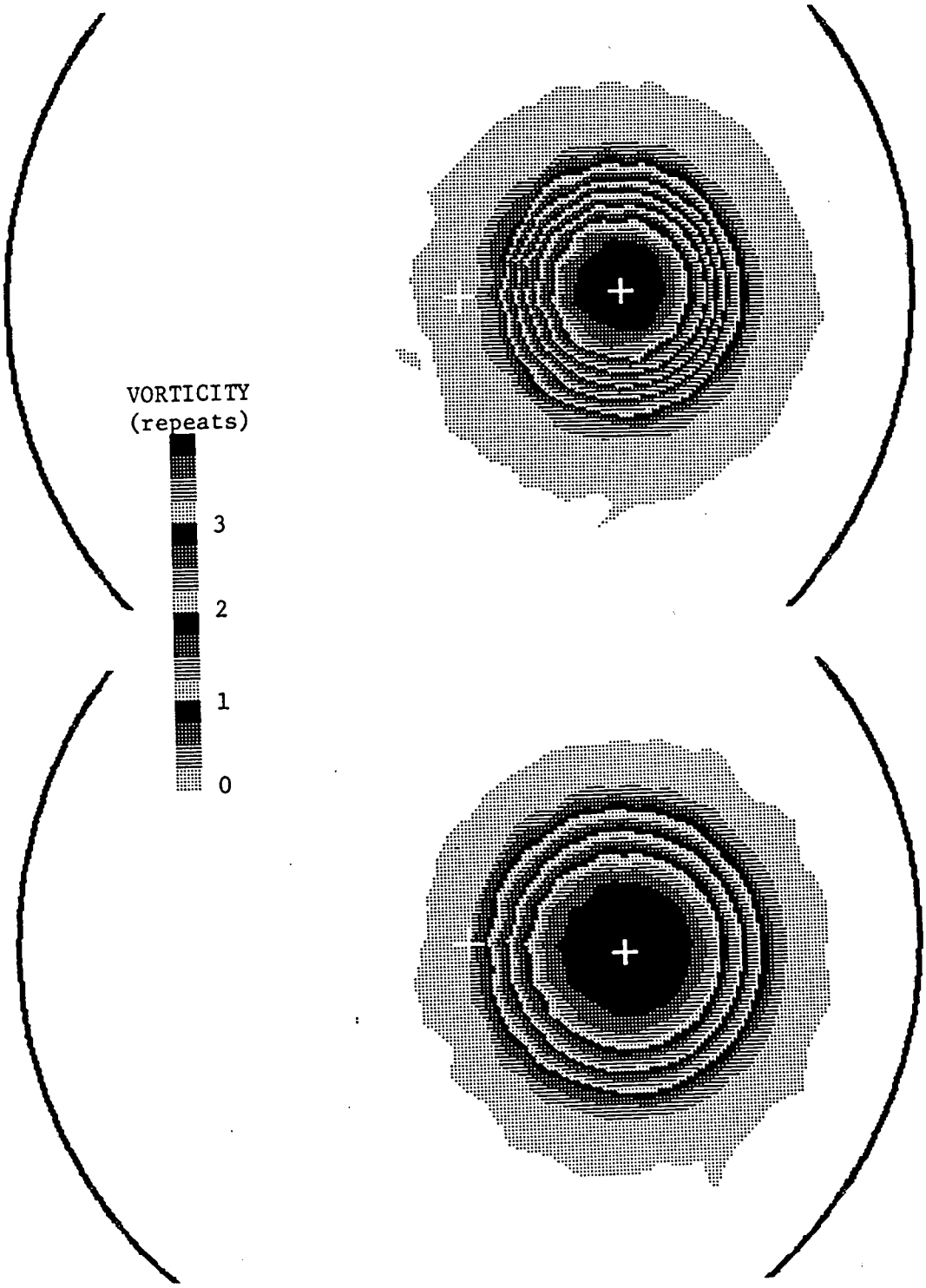

Figure 3.5: Expansion of an off-axis column. $B_z = 94$ Gauss, $L_p \sim 23$ cm, $V_c = -100$ V and $\Delta t = 0.1$ seconds. Density between solid contours: $5.5 \times 10^5 \mathrm{cm}^{-3}$.

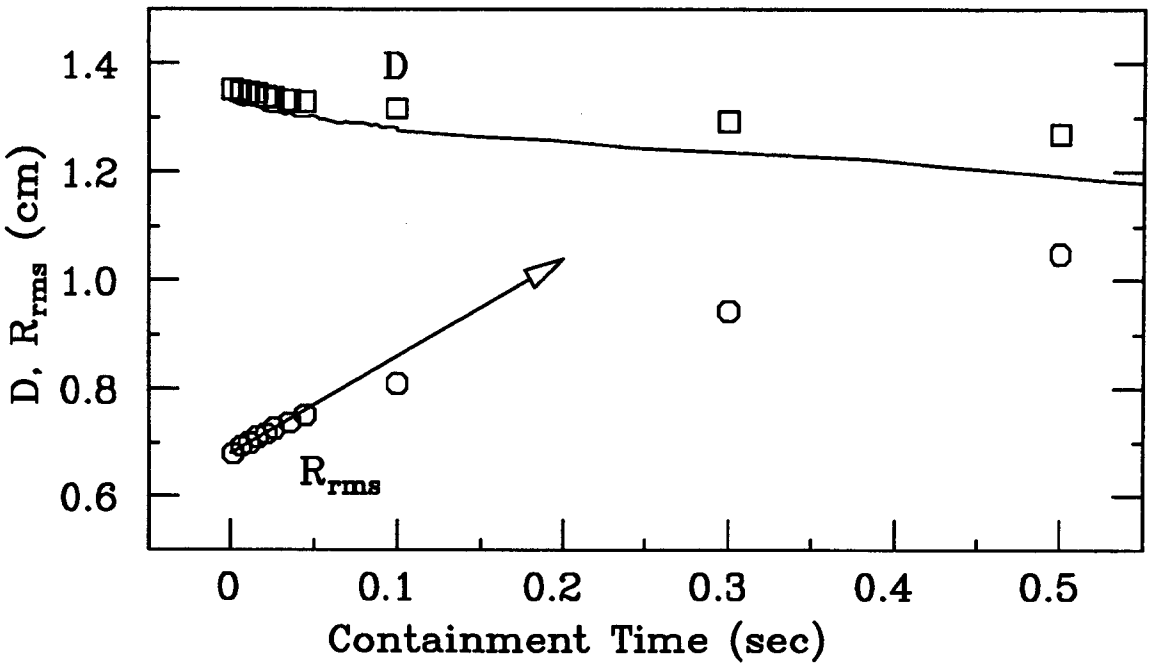

Figure 3.6: Displacement D and radius R_{rms} versus containment time. $B_z = 94$ Gauss, $L_p \sim 23$ cm and $V_c = -100$ V. The solid curve is $D(t)$ measured from wall sector signal analysis.

confinement.

Figure 3.6 shows, for the initial condition of figure 3.5, the evolution of column radius R_{rms} and displacement D with containment time. R_{rms} is defined below in equation 3.7. $D(t)$ was determined by both density plots (□) and wall sector signal analysis (—). The results of these two measurement techniques agree in shape but are offset a small amount which increases with time. The expanding column begins losing density to the wall at about $t = 0.5$ seconds.

As can be seen, the rates at which D and R_{rms} change vary with time. I therefore focused on a study of the rates at early times, before any substantial changes in the plasma parameters has occurred. The rates are measured by fitting the early data points, where the change is linear in time, to a straight line. In figure 3.6, for example, I have used the first 6 points of $R_{rms}(t)$ to calculate an initial slope, shown in that figure with an arrow.

Before proceeding, it is useful to consider how column expansion relates to the angular momentum P_θ. When a column is off-axis, angular momentum conservation does not restrict the rate of expansion of the column's radius, since the column can conserve $\mathcal{P}_\theta$ by both expanding and moving towards the axis. One can thus separate any observed column expansion into transport which does, and transport which does not conserve P_θ. To facilitate this separation, I define the following quantities.

The sum over the j particles, of the square of their radial positions $\sum R_j^2$, can be written in terms of $\mathcal{P}_\theta$ (see equation 2.15) by

$$\sum_j R_j^2 = N_e R_w^2 - \mathcal{P}_\theta \left(\frac{2c}{eB_z}\right) . \tag{3.5}$$

As a consequence, $\sum R_j^2$ is conserved when P_θ is conserved (i.e. when no particles are being lost to the wall). I therefore define a normalized angular momentum L of a continuous 2D density distribution $n(r,\theta)$ by :

$$L \equiv \frac{\int r^2 dr \;\; \int r d\theta \;\; n(r,\theta)}{\int dr \;\; \int r d\theta \;\; n(r,\theta)} . \tag{3.6}$$

It is useful to similarly define a root-mean-square radius R_{rms} of the charge distribution by

$$R_{rms} = \left(\frac{\int r'^2 dr \;\; \int r' d\theta \;\; n(r',\theta)}{\int dr \;\; \int r d\theta \;\; n(r,\theta)} \right)^{\frac{1}{2}} \tag{3.7}$$

where the primed coordinates are about the distribution's center-of-charge.

From these definitions, for a density distribution symmetric about its center we have the relations

$$L = R_{rms}^2 + D^2 \qquad \text{and} \qquad \dot{L} = 2R_{rms}\dot{R}_{rms} + 2D\dot{D} , \tag{3.8}$$

where D is the displacement of the center-of-charge from the axis. The column radius and displacement are thus free to change while conserving L, as long as $R_{rms}\dot{R}_{rms} + D\dot{D} = 0$. Therefore, given measured values of $R_{rms}(t)$ and $D(t)$, I can

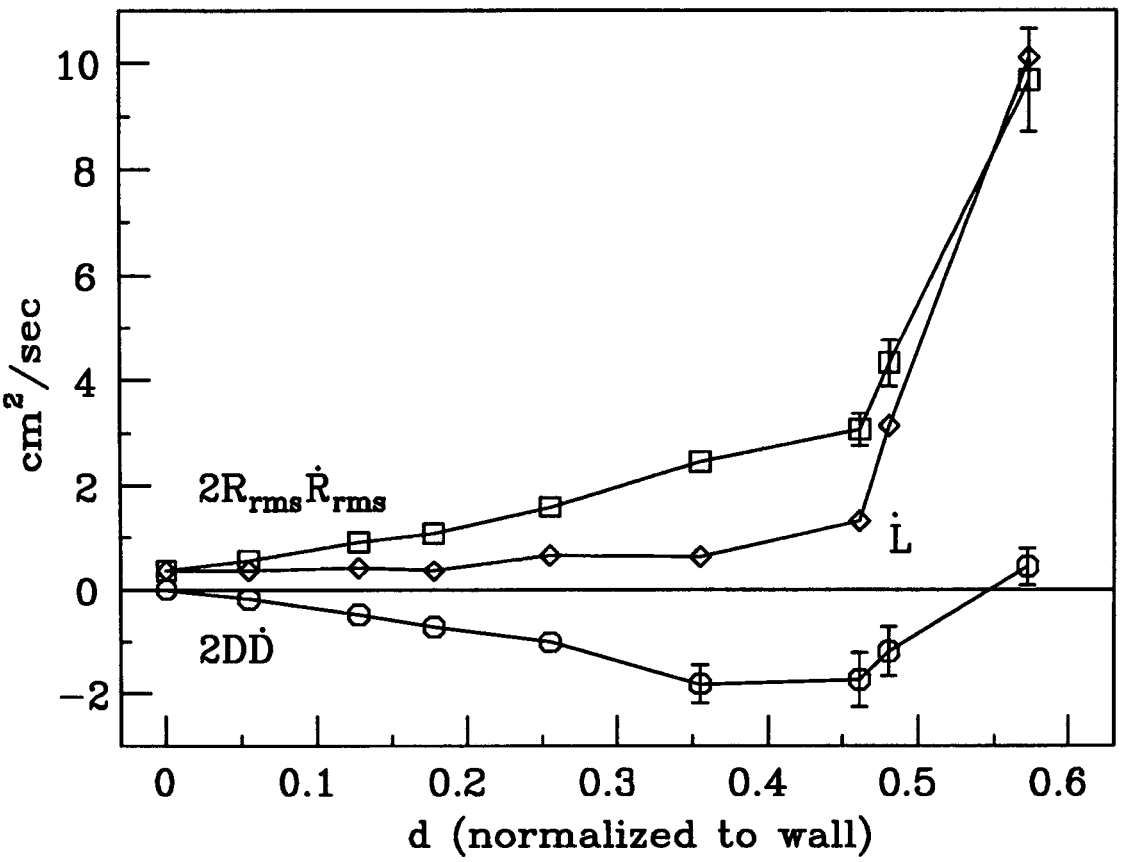

Figure 3.7: Expansion rate ($2R_{rms}\dot{R}_{rms}$), displacement rate ($2D\dot{D}$), and their sum ($\dot{L}$) versus displacement, as measured from density plots. $B_z = 94$ Gauss.

decompose expansion rates $2R_{rms}\dot{R}_{rms}$ into a P_θ-conserving rate $-2D\dot{D}$ and a P_θ-nonconserving rate $\dot{L} = 2R_{rms}\dot{R}_{rms} + 2D\dot{D}$. Such changes in R_{rms} and D will not necessarily, of course, conserve the energy of the system.

Returning to the $B = 94$ Gauss data of the previous figures, in figure 3.7 I plot the initial rates $2D\dot{D}$, $2R_{rms}\dot{R}_{rms}$ and their sum $\dot{L}$ versus the displacement $d = D/R_w$ of the column. The general result is that the expansion rate $2R_{rms}\dot{R}_{rms}$ increases very strongly with D. Expansion can be divided into three separate regions, based on the displacement of the column.

On the axis, the expansion rate is at a minimum, and consists entirely of P_θ-nonconserving transport (as it must, since $D = 0$). The transport rates of this region

have been studied previously by Driscoll, Fine and Malmberg [18], who dubbed the transport 'anomalous transport'. It is believed caused by the small residual electrostatic or magnetostatic field errors of the apparatus, which break the θ-symmetry and thus permit P_θ to change.

For small displacements, $2D\dot{D}$ is found to increase at nearly the same rate as $2R_{rms}\dot{R}_{rms}$, and thus there is little change in $\dot{L}$ from the on-axis value. To a good approximation, therefore, the expansion rate for displacements of $0 < d < 0.36$ is given by the sum of a P_θ-conserving transport process and a constant value $\dot{L}$ of anomalous transport. The P_θ-conserving transport is currently under experimental investigation by Cluggish *et.al* [10] and theoretical investigation by Crooks and O'Neil [11]. It is believed to be caused by 'rotational pumping' of the column by the confinement fields.

In the rotational pumping mechanism, column expansion is driven by thermal heating of the column at the expense of its electrostatic energy, $\mathcal{H}_\phi$. (See section 4.5.3 for a further discussion of this.) I have measured the $\mathcal{H}_\phi(t)$ of the expanding columns of figure 3.7, and observe that $\mathcal{H}_\phi$ always decreases with time at rates increasing with d. This result is consistent with rotational pumping.

For large displacements ($d > 0.36$), I find that while the expansion rate continues to strongly increase with d, the movement of the column back towards the axis slows or even changes sign. The result is large changes in the measured values of angular momentum. The cause of this dramatic increase in $\dot{L}$ is currently unknown, although a reasonable speculation is that it is related to the column's closer proximity to the wall and field errors [26].

I have repeated my measurements of expansion rates for 5 different initial conditions, and with each have found a similar sharp increase of expansion rates with displacement. The measured expansion rates are plotted in figure 3.8, and the

parameters of the different data sets are tabulated at the bottom.

I have established that the expansion rates at small displacements are consistent with other experimental studies. Previous studies have found an $(L_p/B)^2$ scaling for the on-axis $\dot{L}$ transport [18], and an exponential damping of $D(t)$ for the P_θ-conserving transport [10]. This latter result implies the proportionality $R_{rms}\dot{R}_{rms} \propto D^2$. I have fit the data of figure 3.8, for small displacements of $0 \leq d < 0.36$, to the equation $R_{rms}\dot{R}_{rms} = \alpha + \gamma D^2$. These fits are shown (solid curves) in figure 3.8. I find that the data at small displacements is consistent with the predictions: the fit of the data to D^2 is reasonable, and the on-axis transport characterized by α scales roughly as the square of the column length and magnetic field.

The measured damping rates $\gamma = -\dot{D}/D$ are tabulated below figure 3.8. A comparison of these rates with values from a rough calculation of Crooks and O'Neil [11] finds that the measured rates are between 6 and 38 times higher than predicted for rotational pumping. I have tabulated this ratio as γ/γ_{pred}. Rates from data taken at significantly higher densities and magnetic fields by Cluggish [9] are about 4 times higher than predicted. Further studies on both the theory and experimental fronts are begin undertaken, and I feel that it is likely that rotational pumping will be shown to be the mechanism for the P_θ-conserving expansion seen at small displacements.

This still leaves the large P_θ-nonconserving expansion seen at large displacements unexplained. It is interesting that although it has been generally believed that different mechanisms and scalings will characterize P_θ-conserving and nonconserving transport, data sets 1 and 3 show almost identical changes in expansion rate versus d, in spite of their dissimilar magnetic fields. Further measurements of $R_{rms}(t)$ and $D(t)$, preferably made with a phosphor screen and camera diagnostic to reduce data-collection time, will be required to understand transport at large displacements.

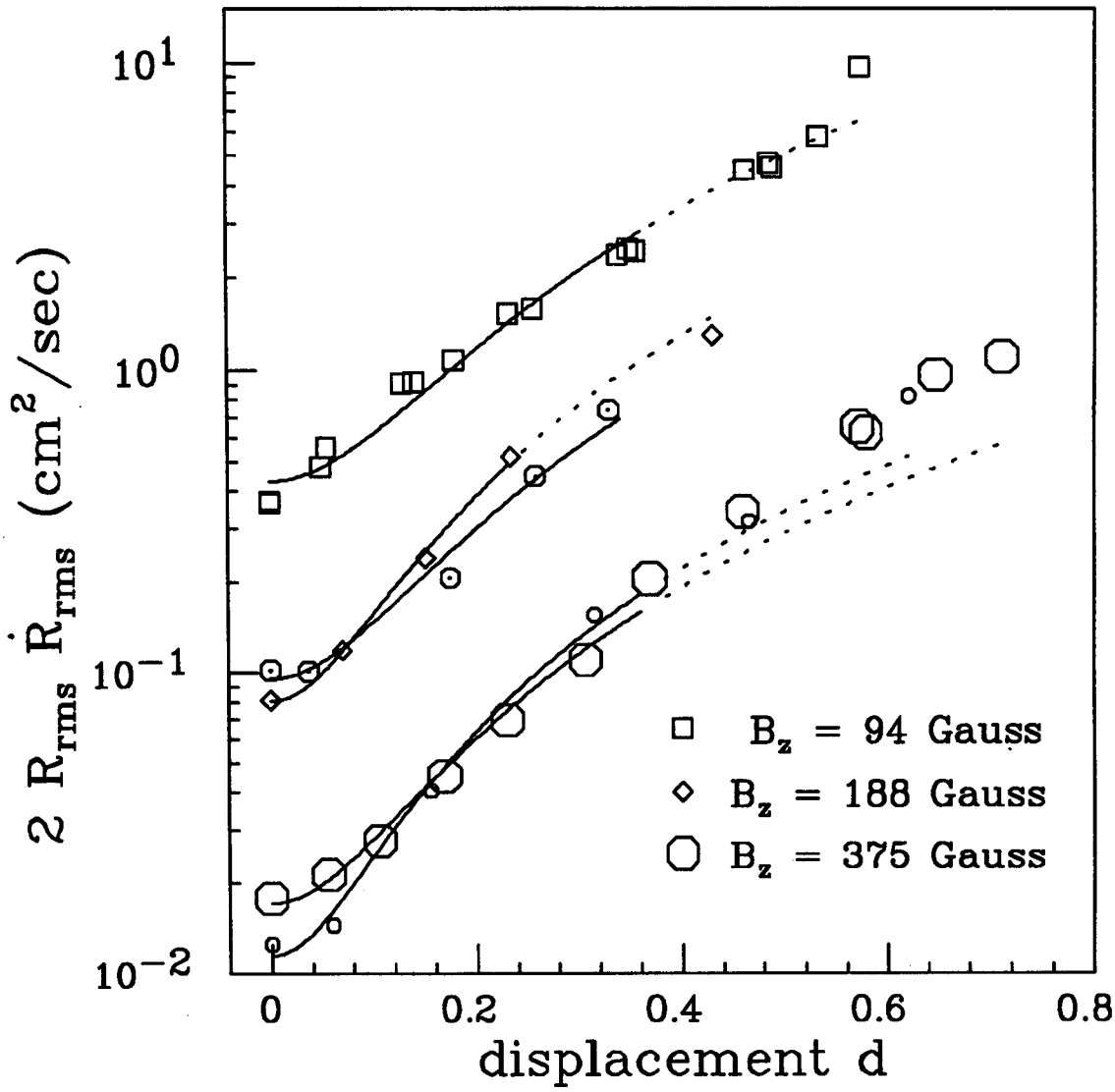

Data Set	B (Gauss)	R_{rms} (cm)	L_p (cm)	T (eV)	$n_{r=0}$ cm^{-3}	V_c/V_{bias}	γ (sec^{-1})	γ/γ_{pred}
1 ○	375	.384	22.4	0.2	5.8 $\times 10^6$	30	.547	8.8
2 ◇	188	.483	22.5	0.2	4.7 $\times 10^6$	30	3.80	36.8
3 □	94	.64	22.5	0.1	3.4 $\times 10^6$	30	9.25	37.
4 ⊙	375	1.30	29.2	1.2	6.8 $\times 10^6$	4.3	2.56	12.
5 ○	375	.397	17.0	0.2	8.8 $\times 10^6$	6.1	.658	6.

Figure 3.8: Expansion rates $2R_{rms}\dot{R}_{rms}$ versus displacement, for the tabulated plasma parameters. The solid curves are fits of the $0 \leq d < 0.36$ data to $\alpha + \gamma D^2$. The dots are continuations beyond $d > 0.36$.

3.2.3 Damping of $l > 1$ Diocotron Waves

I have studied the damping of the $l = 2, 3$ and 4 diocotron/Kelvin waves, and found evidence for mode couplings which have not been previously reported in the literature. At large amplitudes, the $l > 1$ diocotron waves are damped by a non-linear resonance damping process, where particles resonant with the wave drift into low-density filamentary arms [14, 17]. On vortices with 'sharp' radial vorticity profiles, however, small amplitude $l = 2$ and $l = 3$ waves are stable to this resonance damping. I have found that these small amplitude waves are unstable to a decay instability, where the l mode wave decays to both an exponentially growing $l - 1$ 'daughter' wave and (presumably) to a resonant band of particles. This decay instability can be suppressed with negative feedback on the daughter wave, and exponential damping on slow 'viscous' timescales is then observed.

The experiments of this section were done on electron columns whose vorticity profile was adjusted to 'sharpen' the edge and reduce the number of particles resonant with the diocotron waves. The calculated position of the $l = 2$ resonant layer was beyond the edge where the density went to zero. The positions of the $l = 3$ and $l = 4$ wave resonant layers occurred where the density was nonzero, but the densities at these layers were low enough that the waves were readily observable, presumably because so few particles were resonant that the resonance damping mechanism was saturated.

Calibration of the $l = 2$ Wave Amplitude

The diocotron wave amplitudes can be measured with phase-locked plots of the vorticity distribution, or with measurements of the signal $V_{l=i}(t)$ induced by the $l = i$ diocotron wave on a wall sector probe. I have calibrated the $l = 2$ wave case, and find that the amplitude of the wall sector signal $V_{l=2}$ is proportional to the

$l = 2$ wave amplitude, at least until the resonance damping process has resulted in significant transport.

The $l = 2$ wave amplitude can be characterized by the distribution quantities of eccentricity ϵ, aspect ratio a/b, or quadrupole moment q_2. These are easily calculated from phase-locked plots of $n(r, \theta)$ [26]. In the frame of the Cartesian coordinates (x, y) where the origin is at the center of mass of the distribution, I calculate the moments

$$\bar{x}\bar{x} \equiv \frac{1}{N_e}\int dA\, n\, x^2 \qquad \bar{y}\bar{y} \equiv \frac{1}{N_e}\int dA\, n\, y^2 \qquad \bar{x}\bar{y} \equiv \frac{1}{N_e}\int dA\, n\, x\, y\ . \tag{3.9}$$

These moments are used to solve for the angle ϕ_q where a Cartesian system (u, v) with the same origin, but rotated from (x, y), satisfies $\bar{u}\bar{v} = 0$. The eccentricity is then

$$\epsilon^2 \equiv \frac{\bar{u}\bar{u} - \bar{v}\bar{v}}{\bar{u}\bar{u}}\ . \tag{3.10}$$

where ϕ_q is the orientation angle of the quadrupole moment. A top hat profile (i.e. step function radial profile) ellipse with an aspect radio of a/b has an eccentricity given by $\epsilon^2 = 1 - (b^2/a^2)$, so I define an aspect ratio a/b for an elliptical distribution with a physical (non-top hat) radial profile by

$$a/b \equiv \left(1 - \epsilon^2\right)^{-1/2}\ , \tag{3.11}$$

and a quadrupole moment q_2 by

$$q_2 \equiv \frac{a/b - 1}{a/b + 1}\ . \tag{3.12}$$

In figures 3.9 through 3.10 I show 2 phase-locked plots of vortices with an l=2 wave, along with the measured aspect ratio and quadrupole moment. At low amplitudes the $l = 2$ is an elliptical distortion of the column. At large amplitudes, the electrons at the tip of the ellipse do not rotate as fast as the rest, and fall behind in θ, forming distinctive arms. These can be seen in figure 3.10, where 0.23% of

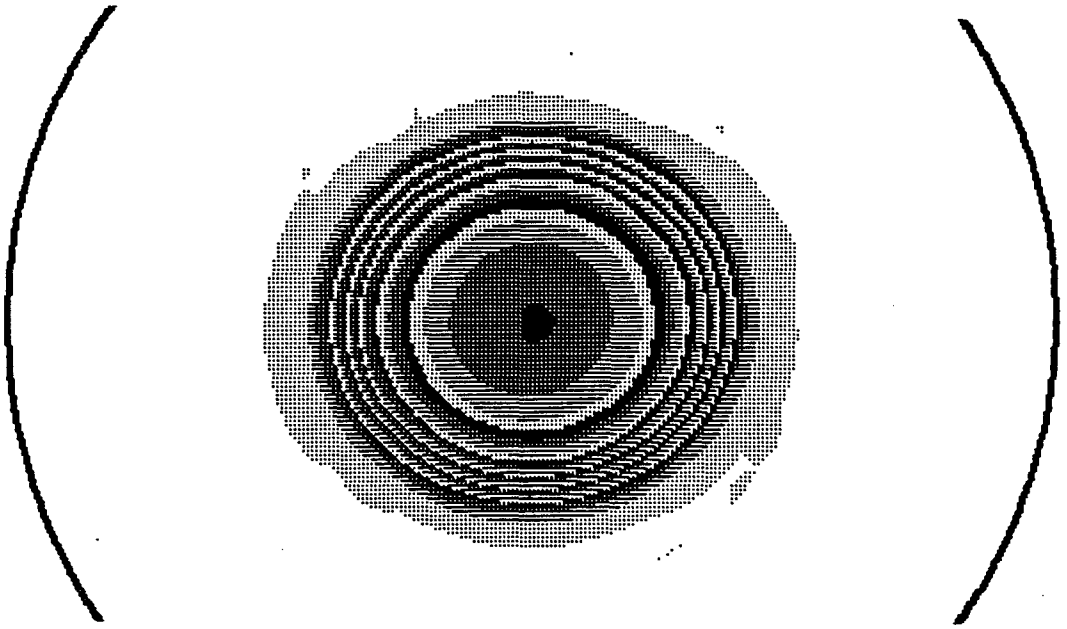

Figure 3.9: Density plot of an l=2 diocotron wave. Eccentricity $\epsilon = 0.44$, a/b = 1.11 and $q_2 = .052$. Density between solid contours: $1.1 \times 10^6 \mathrm{cm}^{-3}$.

the total density has been transported into the arms. This transport constitutes a (spatial Landau-type) mechanism for resonance damping of the mode [14, 17]. In this case, the resonance only occurs at large elliptical distortions, so it would be termed nonlinear damping. The details of the transport depend on the radial profile of the vortex – top hat profiles are not susceptible to it, for example – and the damping saturates when all of the resonant particles have been transported.

I find that the amplitude of the sector probe signal $V_{l=2}(t)$ is proportional to the quadrupole moment q_2. The linearity can be seen in figure 3.11, where I plot the received l=2 signal amplitude versus q_2. The proportionality begins to break down at the largest amplitude shown, which had ~1.3% of the total density in the arms.

Decay Instability of Diocotron Waves

I find that the fastest damping of small amplitude $l = 2$ and $l = 3$ waves occurs due to a previously unknown decay instability, where an $l - 1$ 'daughter'

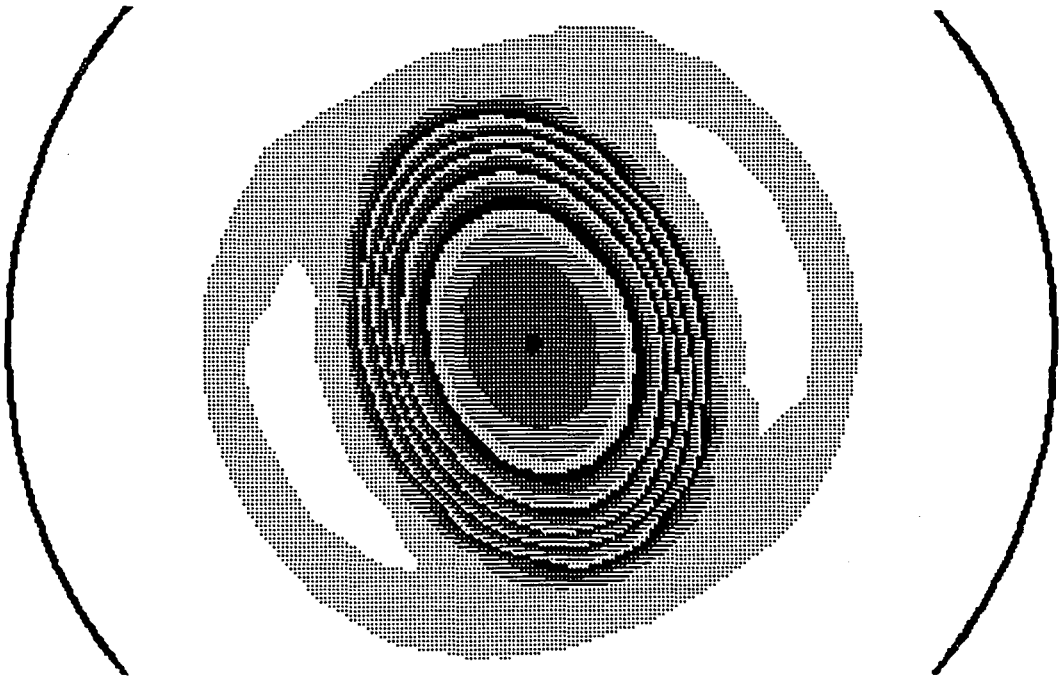

Figure 3.10: Density plot of an l=2 diocotron wave of aspect ratio $a/b = 1.38$ and quadrupole moment $q_2 = 0.16$. Resonance damping has transported 0.23% of the total density to the arms.

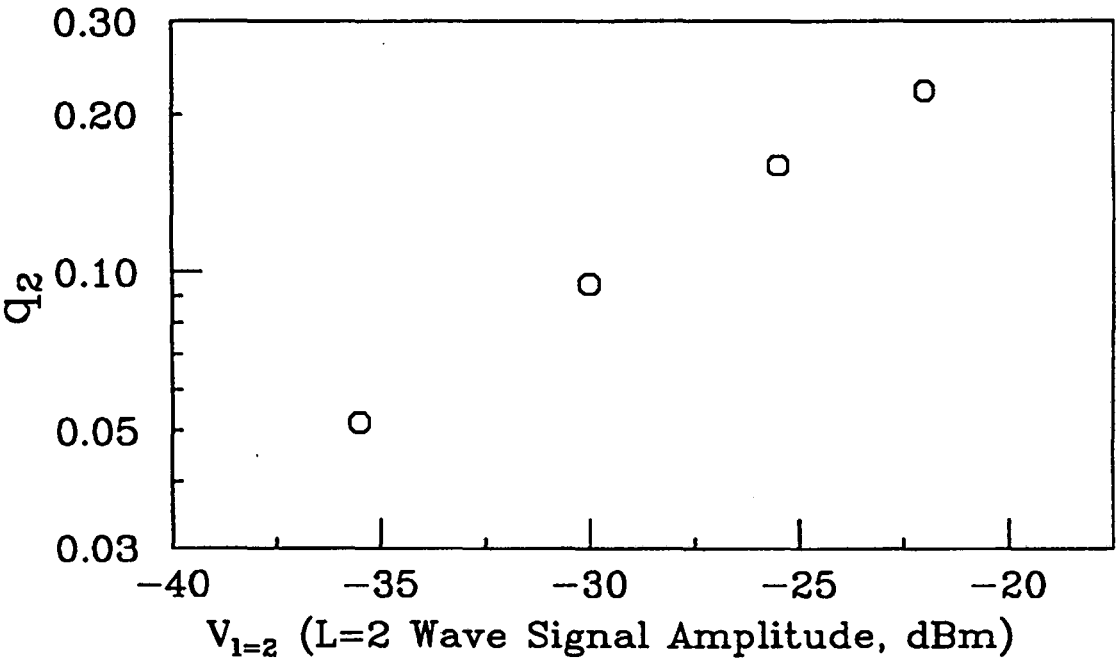

Figure 3.11: Amplitude of l=2 signal received on sector probe versus q_2.

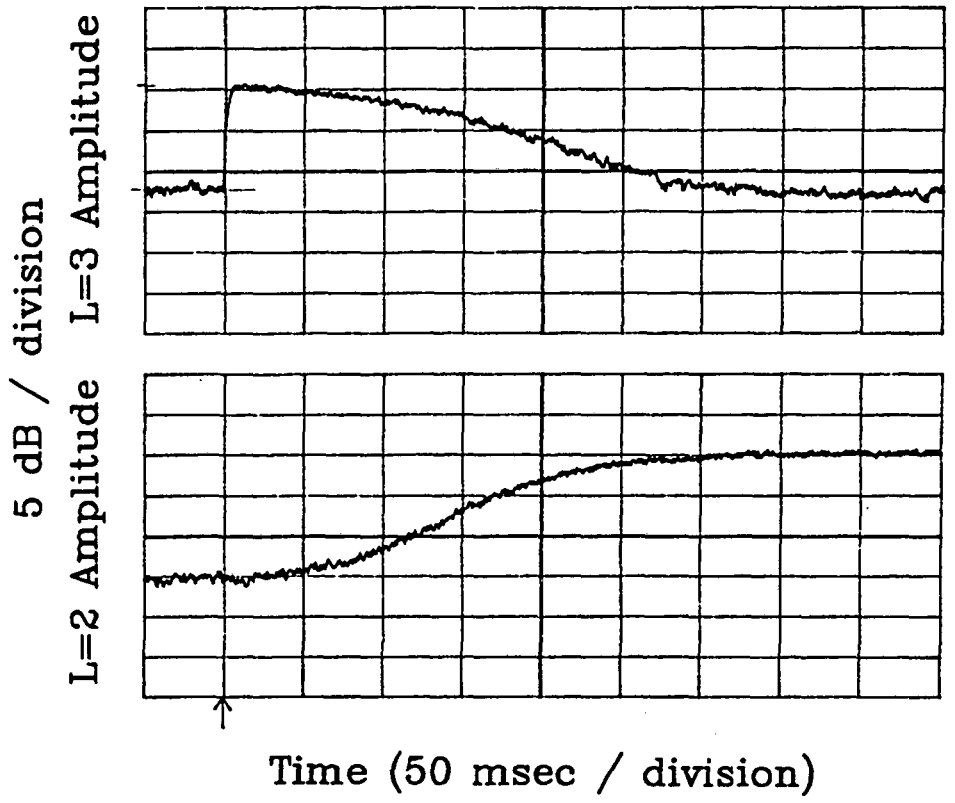

Figure 3.12: Exponential growth of an l=2 diocotron wave during a decay instability of an $l = 3$ wave. The $l = 3$ is grown at the time marked by the arrow.

wave grows exponentially at a rate γ while the decaying wave's amplitude damps as $(1 - e^{\gamma t})$. Figure 3.12 shows an $l = 3$ wave decaying into an $l = 2$ daughter wave. Presumably, transport of resonant particles is simultaneously occurring, and analytic theory and simulation results by Smith support this idea [66].

The shapes of the decaying and daughter wave amplitudes in figure 3.12 differ because wall sector probes of angular extent $\Delta\theta$ couple as $\frac{1}{l}\sin(\frac{l\Delta\theta}{2})$ to waves with an angular dependence of $e^{il\theta}$. When this effect is corrected for, a plot of the wave amplitudes show that the decaying wave and growing wave amplitudes vary symmetrically as $(1 - e^{\gamma t})$ and $e^{\gamma t}$ respectively. I define a time for the decay rates by, using the $l = 3$ decay for an example, $\tau_{3-2} \equiv 1/\gamma$.

The decay times are observed to be strongly dependent on the amplitude of

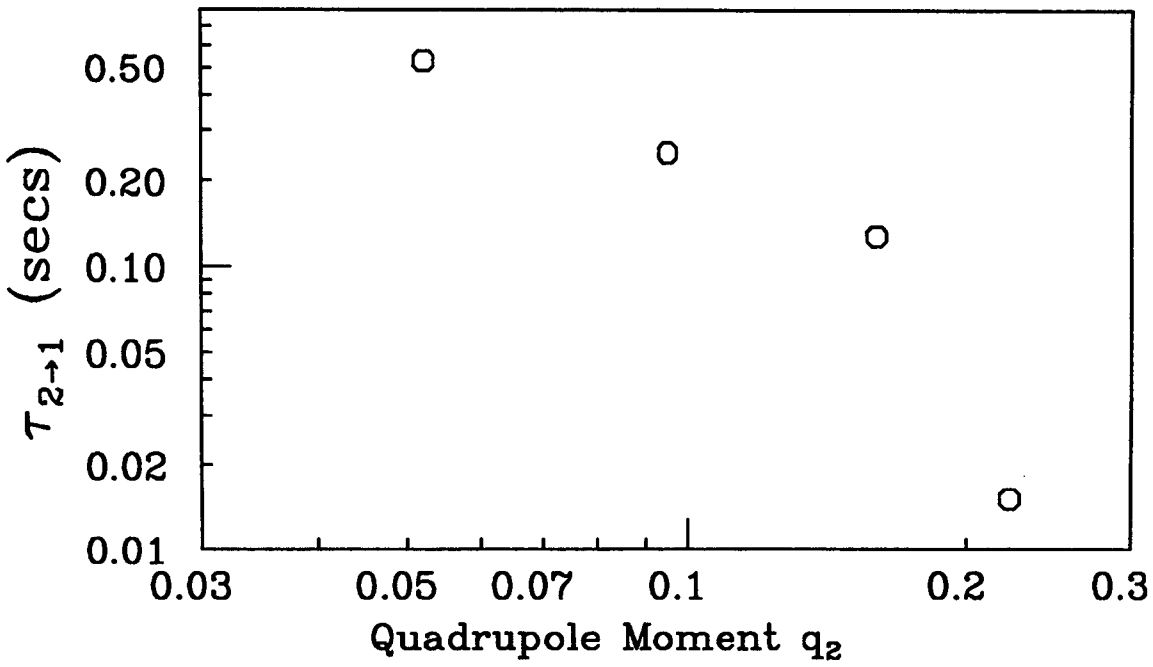

Figure 3.13: Decay time $\tau_{2\to1}$ for the decay process, versus the quadrupole moment q_2 of the damping $l = 2$ wave.

the decaying wave. This can be seen in figure 3.13, where I plot some measured decay times $\tau_{2\to1}$, versus the quadrupole moment of the damping $l = 2$ wave. I additionally found, although I don't plot them, that the times $\tau_{3\to2}$ for the decay of an $l = 3$ wave showed a similar dependence on the $l = 3$ wave amplitude.

Exponential Damping of the Diocotron Waves

The $l = 4$ wave, whose resonance layer was deeper within the vorticity profiles than the $l = 2$ and $l = 3$ waves, was found not to be susceptible to the decay instability, but rather to damp exponentially with a time constant $\tau_{l=4} = 0.065$ seconds. Similarly, I have also observed exponential damping of the $l = 3$ and $l = 2$ waves, with time constants at small amplitude of $\tau_{l=3} = 2.7$ secs and $\tau_{l=2} = 5.1$ secs. (With these waves, it was necessary to suppress the decay instability with a continuous application of negative feedback on the daughter mode. Filtration of the feedback signal prevented any inadvertent growth or damping of the original mode.)

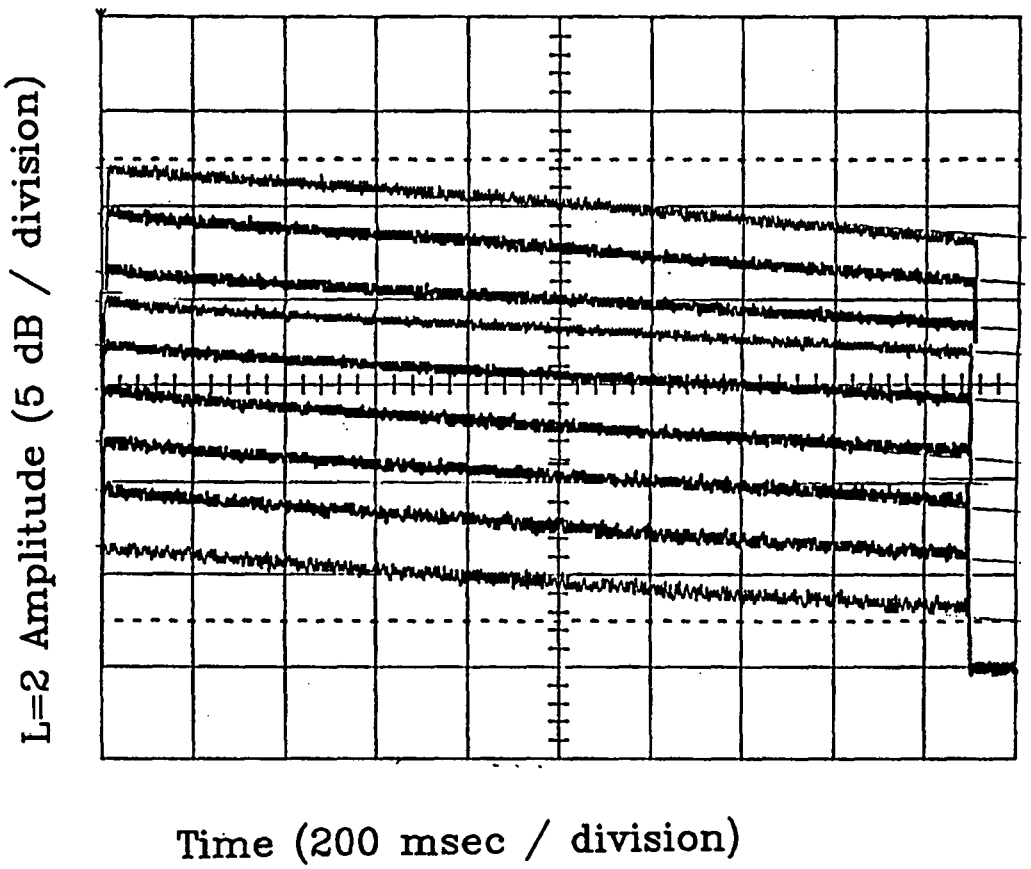

Figure 3.14: Exponential damping of nine l=2 waves of different initial amplitudes. Continuous negative feedback of the l=1 wave is on.

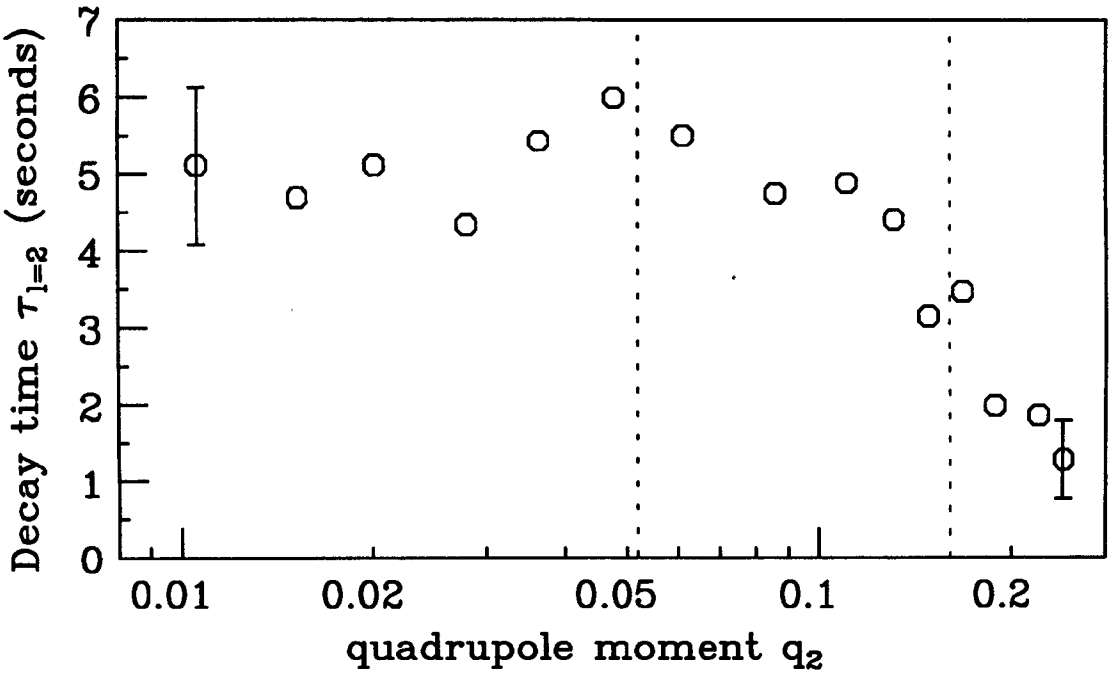

Figure 3.15: Time constant of l=2 damping, $\tau_{l=2}$, versus initial quadrupole moment of the l=2. The dotted lines indicate the amplitudes of the l=2 waves displayed in figures 3.9 and 3.10.

I have measured the variation of the $l = 2$ exponential damping with its amplitude, and found the damping to be independent of amplitude until resonance damping at large amplitudes became effective. Figure 3.14 shows the logarithm of the $l = 2$ signal amplitude versus time, for 9 different initial amplitudes. Damping rates were measured from the slopes of such wavesignals, and the time constant of the damping $\tau_{l=2}$ is plotted versus the initial amplitude of the l=2 wave in figure 3.15. The damping is observed to be roughly independent of amplitude with a $\tau_{l=2}$ of 5.1 ± 0.5 seconds, until the amplitude reaches the resonance damping regime of arm formation, where the damping rate becomes greater with increasing initial amplitude.

An explanation of the observed exponential damping consistent with previous experimental work is that the wave is damped by interparticle ('viscous') interactions. According to this view, velocity shears present in the initial profile and shears caused by the l=2 wave relax exponentially due to collisional particle transport. Driscoll has

measured the equilibriation time τ_{eq} at which monotonic profiles relax, and found τ_{eq} of 10 $\pm$ 4 seconds [31]. The observed small amplitude l=2 damping time of 5.1 seconds is within the experimental uncertainties of this rate. If this hypothesis holds up under further investigation, the l=2 damping rate (when decay damping is inhibited) could serve as an easily measurable quantity with which to investigate viscous interaction rates.

3.2.4 Love's Instability for Elliptical Vortices

I have observed $l = 3$ perturbations to grow exponentially on highly elliptical vortex structures. The growth of these perturbations can be measured directly with $n(r, \theta)$ plots. While the initial conditions required for this instability are those of a very large amplitude $l = 2$ diocotron wave, I was unable to simply grow an $l = 2$ mode to large enough amplitudes because of resonance damping on the non-zero edge of the vorticity profile. However, I was able to create highly elliptical initial conditions by injecting two circular vortices next to each other and allowing them to merge (section 4.5.1).

Figure 3.16 shows the time evolution of an elliptical vortex with an aspect ratio $a/b > 4$ and little initial $l = 3$ perturbation. By $t = 76$ μsecs the $l = 3$ component has saturated with an amplitude 80 times greater than that at $t = 20$ μsecs.

In figure 3.17 I plot the measured $l = 3$ amplitude versus time, for the same data sequence. The solid symbols correspond to the two plots of figure 3.16. The ratio of the $l = 3$ growth rate to the $l = 2$ frequency is found to be $\gamma/f_{l=2} \approx 4.9$. (I note that the instability would not be observed if it were significantly slower, because the elliptical structure is heavily damped by resonance damping.) I have also found that the instability can be seeded. Specifically, the phase of the l=3 wave resulting after merger can be changed π radians by reversing the sign of an initial vorticity

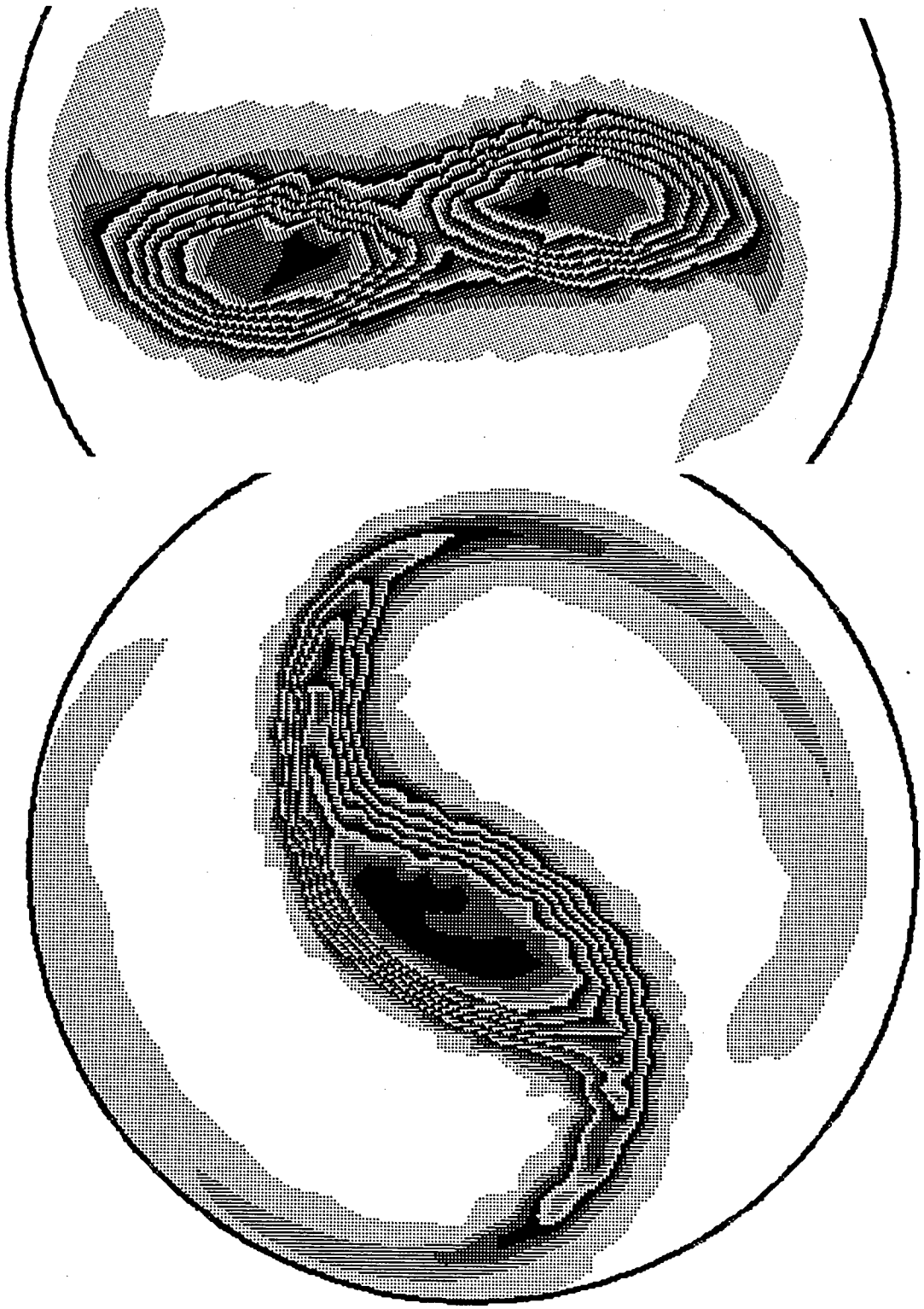

Figure 3.16: Density plots of an elliptical vortex unstable to Love's instability. Times: t = 20 and 76 μsecs. Density between solid contours: $2.9 \times 10^5 \mathrm{cm}^{-3}$.

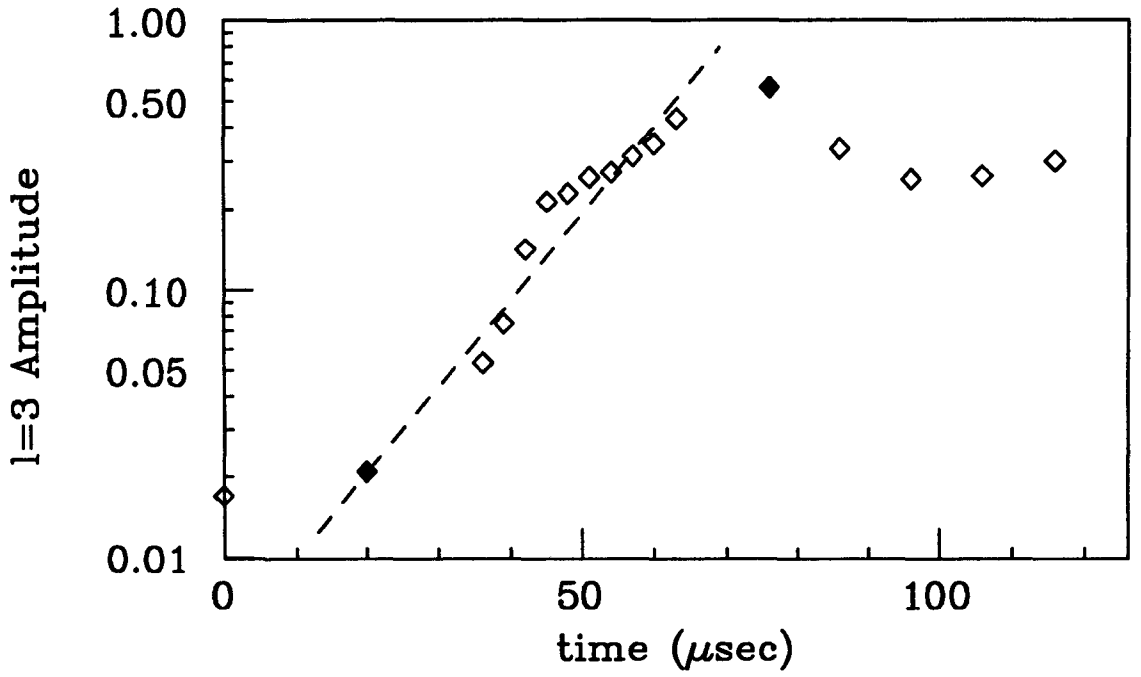

Figure 3.17: Amplitude of an l=3 perturbation versus time. Density plots corresponding to the solid symbols have been shown in figure 3.20. The result of a fit, giving a growth rate $\gamma/f_{l=2} = 4.9$, is also shown (dashed line).

perturbation. This is done by slightly altering the containment voltages of the setup.

This appears to be the first experimental observation of an instability predicted 100 years ago by Love, who investigated the stability of top hat profile elliptical vortices in 1893 [44]. (Ironically, he found the subject of elliptical vortices to be a 'somewhat ancient matter' since Kirchhoff [40] and Hill [35] had been working on it 10 years before.) He found that elliptical vortices were stable for aspect ratios $a/b < 3$, and unstable to $l \geq 3$ perturbations for $a/b > 3$. In the range of $3 < a/b < 5.8$, he found that the $l = 3$ perturbation was the fastest growing. For aspect ratios of 4.2:1, which is about the aspect ratio of the data of figure 3.17, Love's predicted growth rate for l=3 perturbations is $\gamma/f_{l=2} = 4.44$.

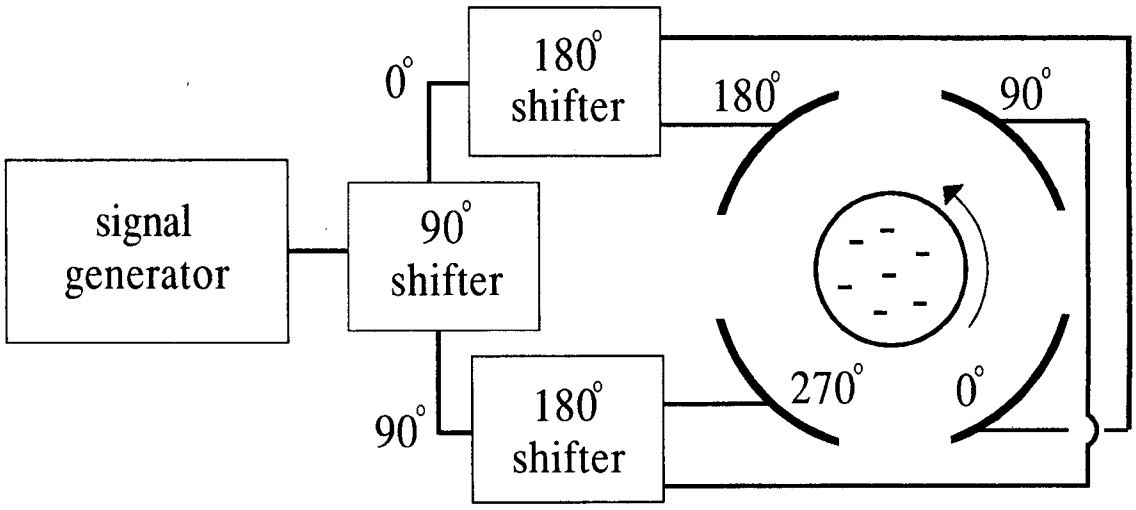

Figure 3.18: Experimental setup to investigate transport from θ-phased electric field perturbations.

3.3 Rotational Compression from $l = 1$ Phased Perturbations

Eggleston, O'Neil and Malmberg [25] have established that transport induced by asymmetric perturbing fields is enhanced by collective effects involving electron plasma modes. Interestingly, they found that the characteristics of the induced mode determined the transport; for example, modes rotating faster and in the same direction as the column transported density in. They were, however, only able to obtain a maximum 25% increase in central density from this effect, and did not demonstrate a net angular momentum increase (i.e. $\sum_j R_j^2$ decrease). I have investigated the effect further to determine whether it can be used as a technique for getting useful density increases. I have been able to demonstrate a net transfer of angular momentum to the column, but have also found that associated heating limits its usefulness.

Figure 3.18 shows the experimental setup. A frequency generator provided a perturbation signal of variable frequency f_{pert} and peak-to-peak amplitude V_{pert} (Volts). In order to give the perturbation a direction of rotation, the signal was put

through one 90° and two 180° phase splitters to produce 4 signals 90° apart in phase. These were then connected to the four wall sectors, also 90° apart, to give an $l = 1$ perturbation rotating either in the $+\hat{\theta}$ or $-\hat{\theta}$ direction (where the $+\hat{\theta}$ direction is defined as being the direction that the column rotates about its axis).

The frequency response of transport caused by those $l = 1$ perturbations was scanned by measuring the central density as f_{pert} was scanned. This revealed the presence of modes transporting density in or out of the center. The $k_z = 0$ (diocotron) modes were found to cause outward radial transport only. The $k_z \neq 0$ plasma modes were found to produce inward transport from perturbations rotating faster than the column in the $+\hat{\theta}$ direction, and outward from those in the $-\hat{\theta}$ direction.

I then focused on maximizing angular momentum transfer with the application of perturbations at the resonant frequency of $+\hat{\theta}$ plasma waves. To achieve maximal radial transport, I found it necessary to adjust the frequency of the perturbation, since the plasma mode's frequency shifts due to changes in the density profile. In figures 3.19 through 3.21 I show the collimated density and temperature profiles resulting from 1, 2 and 3 successive perturbations (of 0.5 seconds duration each) at an amplitude of $V_{pert} = 0.35$ Volts. The profile when the perturbation wasn't switched on is also shown. The temperature points shown were measured from the perturbed column, and the initial (unperturbed) column had a temperature of 0.9 eV.

My conclusions about rotational compression are as follows. The general idea that induced waves can impart angular momentum to (or from) the plasma is correct – the figures show this happening very cleanly. However, there is a strong correlation between the amount of transport and the amount of heating caused by the driven wave. The large rate of heating – more than 4 eV/particle for a decrease in $\sum_j R_j^2$ from .973 to .924 cm^2 – limits the usefulness of this technique, since at 10

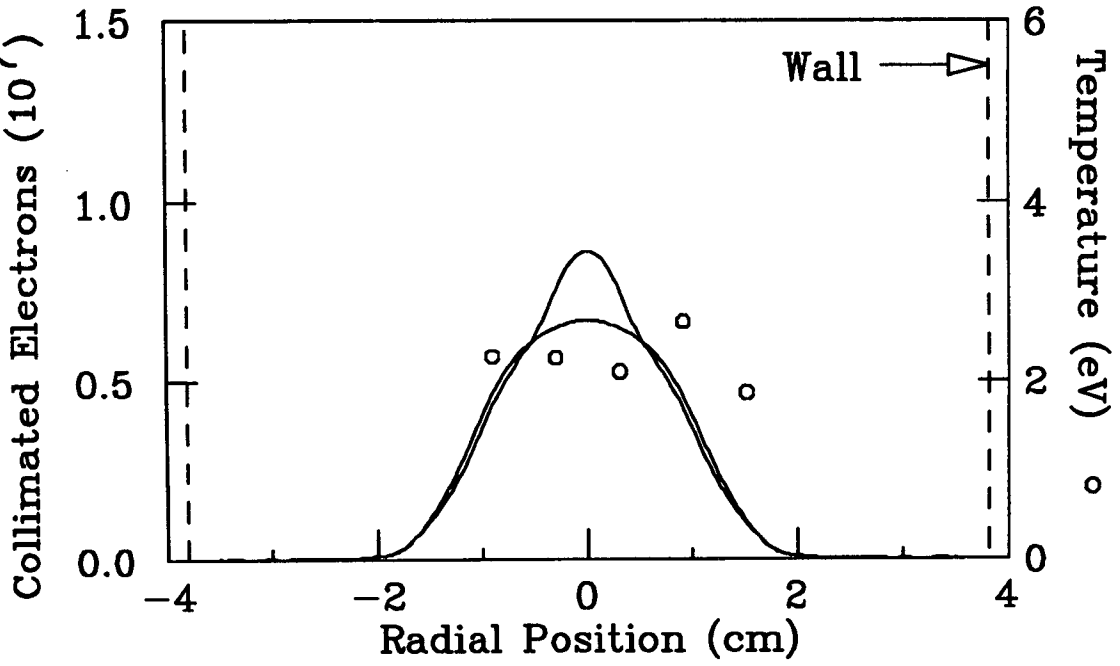

Figure 3.19: Radial collimated density and temperature profiles of column with and without an applied $l = 1$ perturbation of $V_{pert} = 0.35V$ at 9.5 MHz for 500 msec.

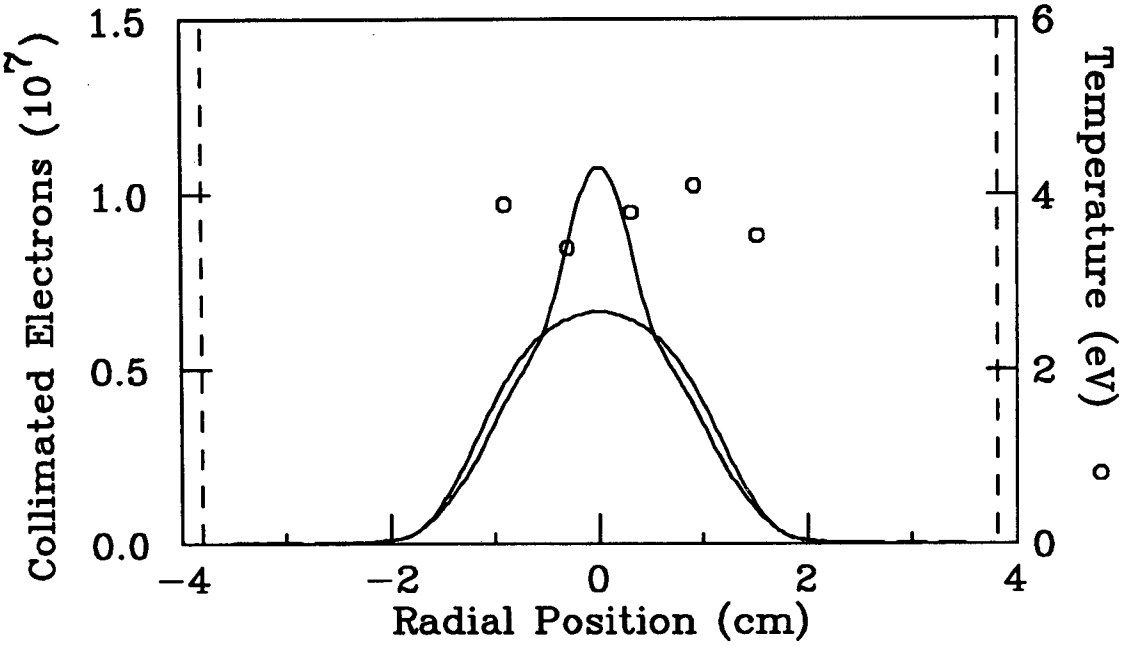

Figure 3.20: Same as figure 3.2, with second perturbation of 0.35 V_{pert} at 11.3 MHz for 500 msec.

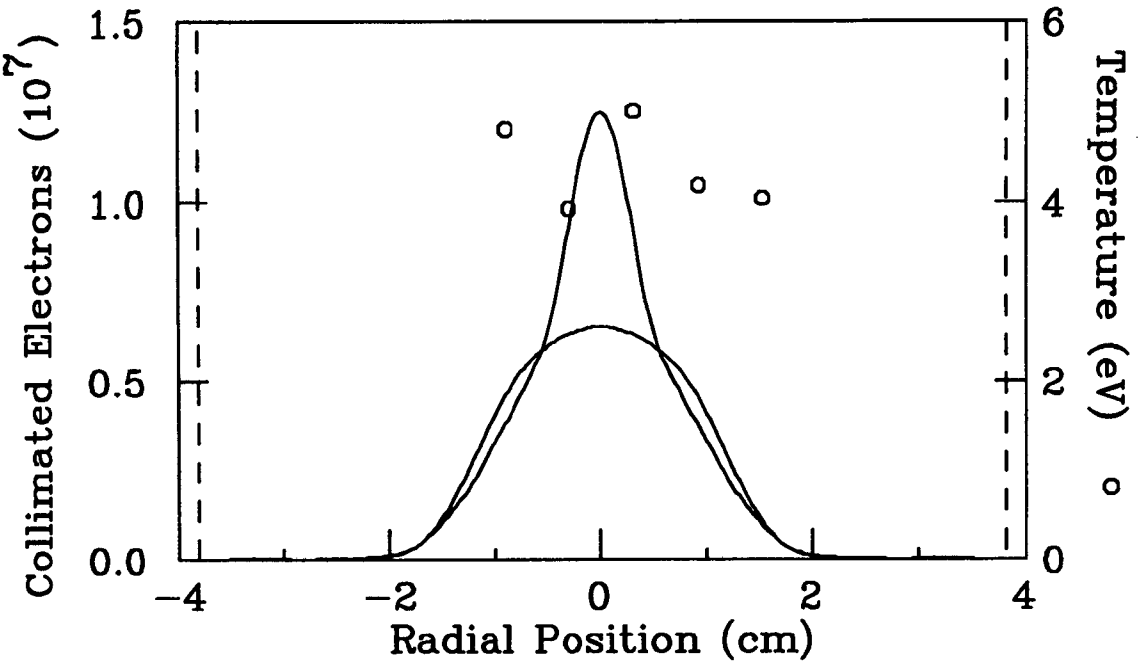

Figure 3.21: Same as figure 3.3, with third perturbation of 0.35 V_{pert} at 11.75 MHz for 500 msec.

eV ionization of the background gas is appreciable.

3.4 B_z Misalignment and l=0 'Sloshing' Signals

Misalignments of the magnetic field with the axis of the containment region are known to strongly impact transport and hence confinement times in Malmberg-Penning traps [26]. The EV apparatus has two magnetic field correction coils to create B_x and B_y fields, which enable the angle of the magnetic field to be changed. Measurements of confinement time are normally used to find the best alignment. This technique, 'confinement alignment', requires measurements of the plasma density remaining (usually central density) after long times, as a function of the correction field strengths. The correction coils are afterwards kept tuned to the fields which maximize the confined density.

Misalignment is also observed to result in l=0 signals off the containment

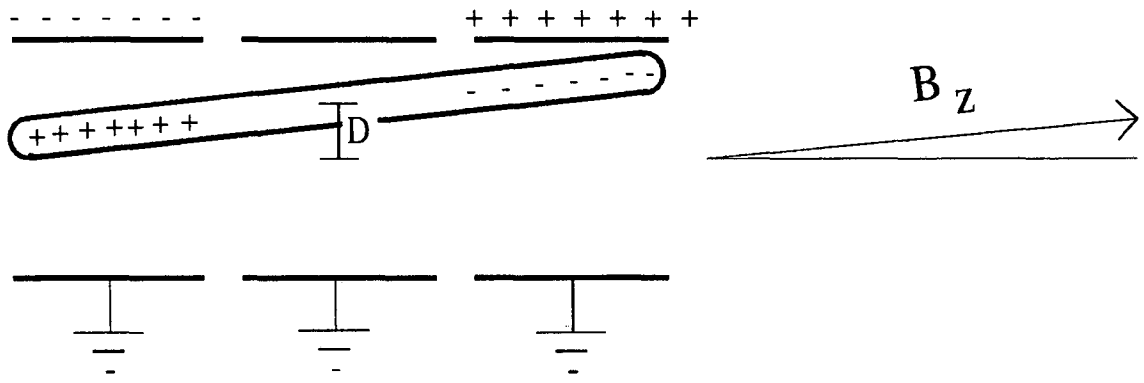

Figure 3.22: Density perturbation in $\hat{z}$ when an l=1 mode is present and B_z is misaligned.

rings, at the l=1 diocotron frequency, when an l=1 mode is present [33]. The reason that these signals are produced can be seen in figure 3.22, which is a schematic for what is happening at one instant in time. The column has a displacement D, and B_z is misaligned by an angle α. Due to the position of the wall surfaces relative to the column, one expects a density surplus on one end, and a density deficit at the other. (Because the $l = 1$ diocotron frequency is so much smaller than the plasma frequency or the bounce frequency, one can view the perturbation as a quasistatic change in the equilibrium rather than as a driven oscillation [33].) When the column has rotated about the trap axis by π radians, the perturbation will have changed sign, and the amount of charge within a ring will have changed. Hence one expects, as a consequence of the misalignment, to pick up an l=0 signal at the same frequency as the l=1.

Because the signals are functions of the misalignments, it is plausible that the best alignment of the magnetic field with the trap can be identified through their analysis. Hart [33] has asserted that minimizing the difference between signals on the end rings (next to the confinement gates) provides an easier and more accurate way of aligning Malmberg-Penning traps than the traditional method of tuning the

correction fields to minimize transport. He did not present any comparison between confinement alignment and this 'signal null' alignment, however.

I have made a study, on the EV apparatus, of the $l = 0$ signals as a function of alignment, and have found that at small misalignments the signals from different rings lose coherence. This suggests that local sloshings due to individual ring misalignments are taking place, rather than the single sloshing mode observed at large misalignments. This in turn suggests a technique for identifying the best alignment through the minimization of the sum of the signal power off all the rings. I find that this 'summed power' alignment technique yields closer agreement with confinement alignment than the signal null technique does.

3.4.1 $l = 0$ Signals from Large and Small Misalignments

Figure 3.23 shows the $l = 0$ signals measured from the rings for an l=1 amplitude of d = .06 and a B_z misalignment of 2.2×10^{-3} radians. The column, of radius $R_p \sim 1/3R_w$, was contained within the rings L3, L4, S, L5, G2; here listed in order of increasing distance from the filament. The oscilloscope was typically triggered off a specific phase of the l=1 signal, producing recordings of the l=0 signals phase-locked to the $l = 1$ mode. This was not possible for the recording of the S ring signal, as all its sector probes and its frame had to be connected together to measure the l=0 signal off it. The rings were capacitively coupled to a high-impedance low-noise amplifier.

These signals are consistent with the model shown in figure 3.22. The end rings (L3, G2) have the largest amplitudes (being closer to the end of the column than L4 and L5). There is little signal from the S ring, due to its central position in $\hat{\mathbf{z}}$. Additionally, the signals from rings on opposite sides of S are of opposite phase. In figure 3.24 I plot the l=0 signal amplitude from an end ring as a function of displacement d. It is linear in d near the axis, as has been predicted by Hart [33].

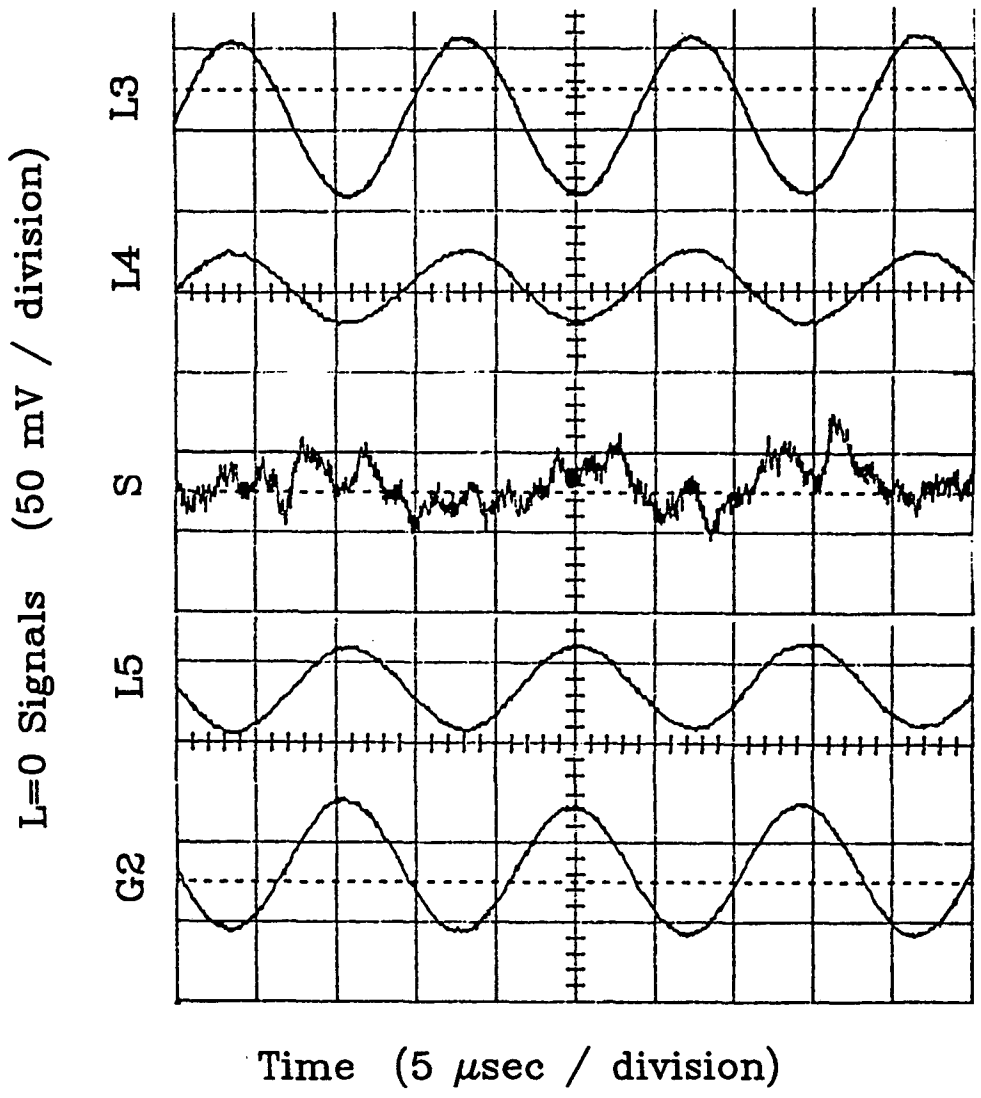

Figure 3.23: l=0 signals recorded with (large) misalignment $\alpha = 2.2 \times 10^{-3}$ radians and displacement $d = .06$. The S signal alone is not phased to the $l = 1$, and has amplitude 5 mV / division.

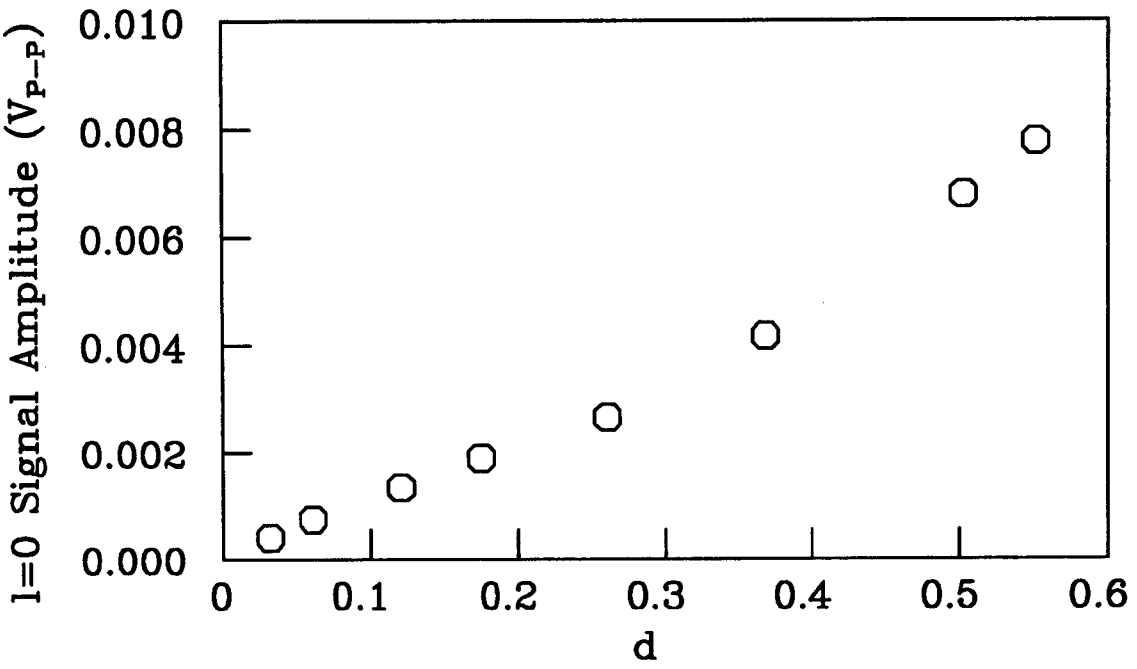

Figure 3.24: l=0 signal amplitude from an end ring, versus displacement of the column

In figure 3.25 I show the $l = 0$ signals resulting when the difference in the signals off the end ring are minimized, i.e., the signals (L3+L4) and (L5+G2) are closest to being identical. This 'signal null' alignment has a small misalignment of 1.2×10^{-4} radians from the confinement alignment value. The $l = 0$ signals here show important differences from their behavior at large misalignments. The signal amplitudes are smaller than those shown in figure 3.23, as expected, but are still appreciable ($>$ 20 dB above noise), and do not display the phase coherence seen previously. Indeed, the amplitudes and phases of the signals are now observed to be complicated functions of the geometry of the different rings and misalignment angle α.

I have concluded that there is a single 'global' mode of density sloshing only for large misalignments, and that at small misalignments there are 'local' sloshings between the individual rings. While this is hardly surprising – any containment

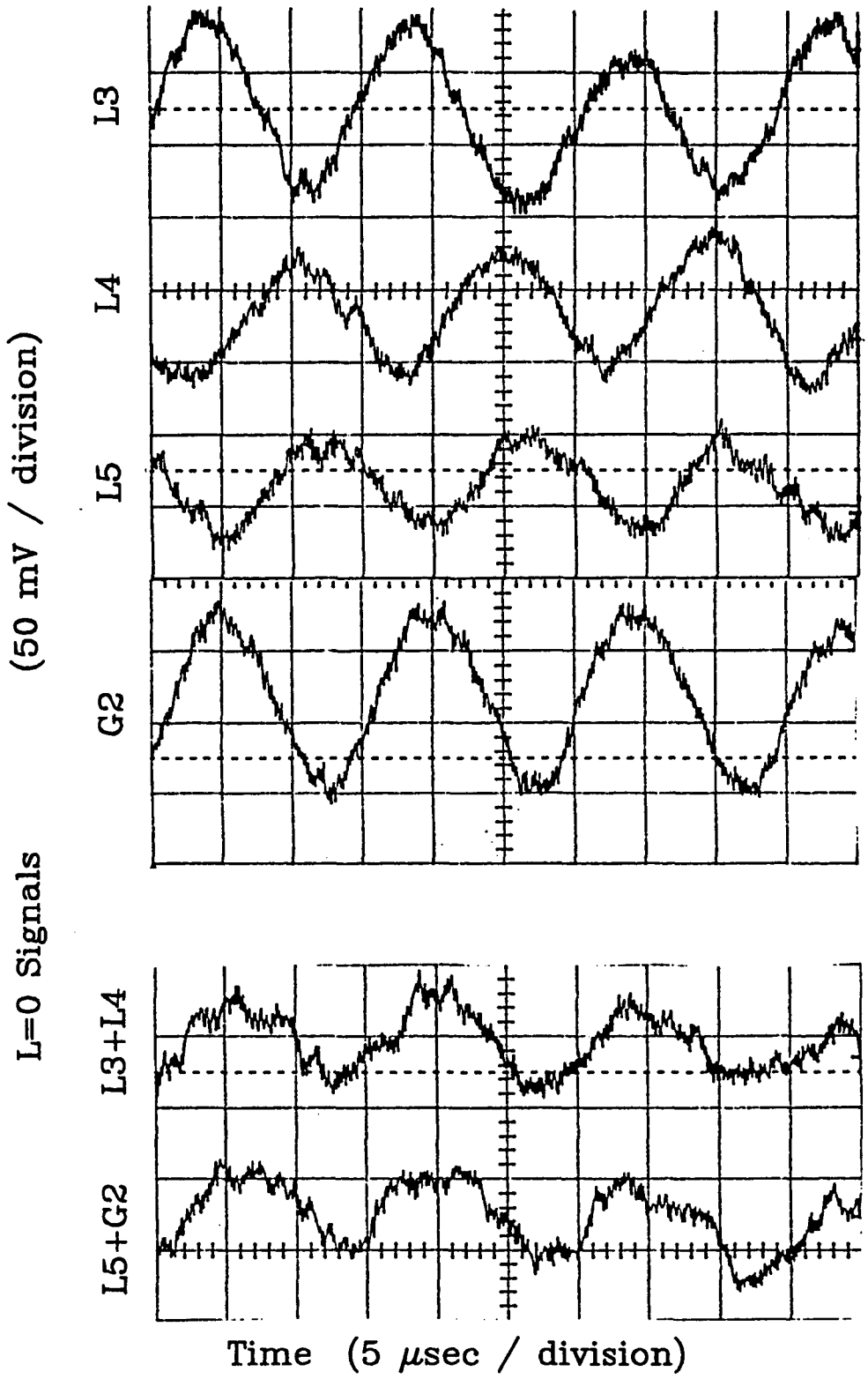

Figure 3.25: The l=0 signals recorded when the signal (L3+L4) − (L5+G2) was minimized ('signal null' alignment). Misalignment from 'confinement alignment' was $\sim 1.2 \times 10^{-4}$ radians.

region broken up into rings is bound to have small asymmetries in $\hat{\mathbf{z}}$ after it is assembled – it suggests that 'signal null' alignment (at least on the EV apparatus) is not a likely prescription to identify the alignment given by transport measurements (confinement alignment).

An alternative alignment approach is to minimize the sum of the signal power (i.e. signal amplitude squared) off all of the containment rings. The reasoning behind this is that since the signal amplitude off a ring indicates the proximity of the electron column to that ring, a minimization of the sum of the squared amplitudes should give a 'least-squares' alignment within all the rings. I term this alignment technique 'summed power' alignment.

3.4.2 Quantitative Comparisons of Alignment Techniques

I have quantified the differences between the alignments which minimize transport (confinement alignment) and those which minimize end signal differences (signal null alignment). For one particular confinement geometry (rings L1 to S), I have measured these B_x, B_y alignments as a function of B_z. A linear dependence of alignment values versus B_z implies that alignment is given by a specific angle within the trap. The measured values are plotted in figures 3.26 and 3.27, along with a least-squares fit through the data. My conclusion is that the confinement alignment and signal null alignment techniques both define angles, but that these are different angles.

In figure 3.28 I show the tuning curve given by the summed-power alignment (line) along with that given by confinement alignment (dots). The dashed lines show the measured signal power from individual rings. Each ring has its individual θ_x value at which its signal is minimized. The solid line is the sum of the signal power, and the dots show the central density (arbitrary units) remaining after 10 seconds. As can be seen, the minima of transport (i.e. the peak of the remaining central

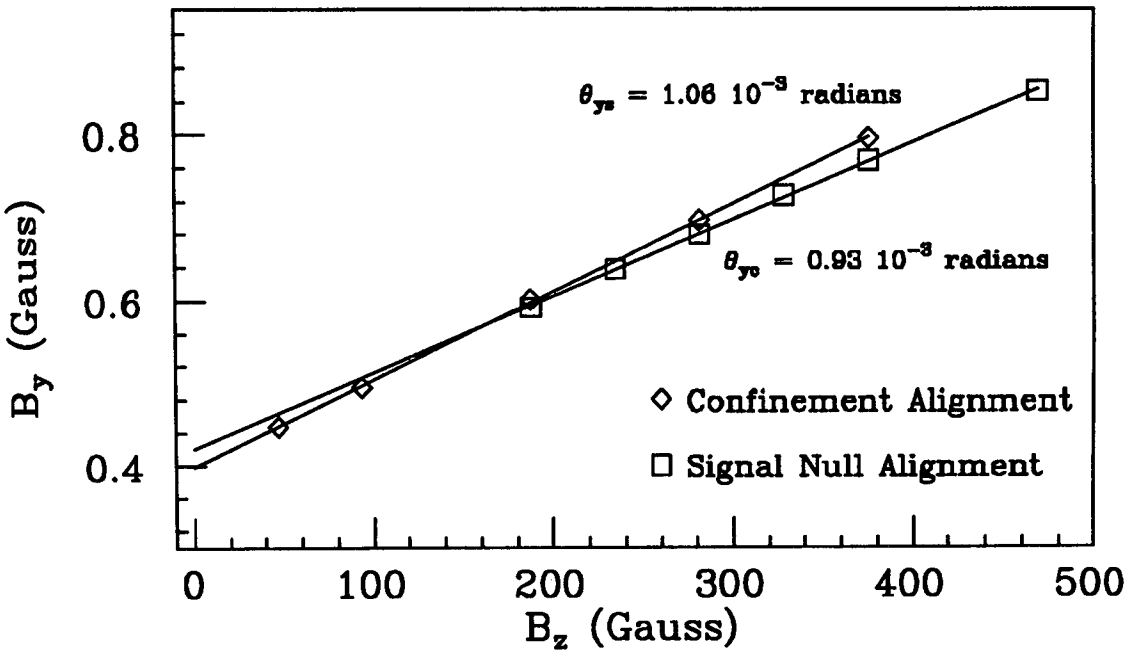

Figure 3.26: B_x correction for confinement alignment (◇) and signal null alignment (□).

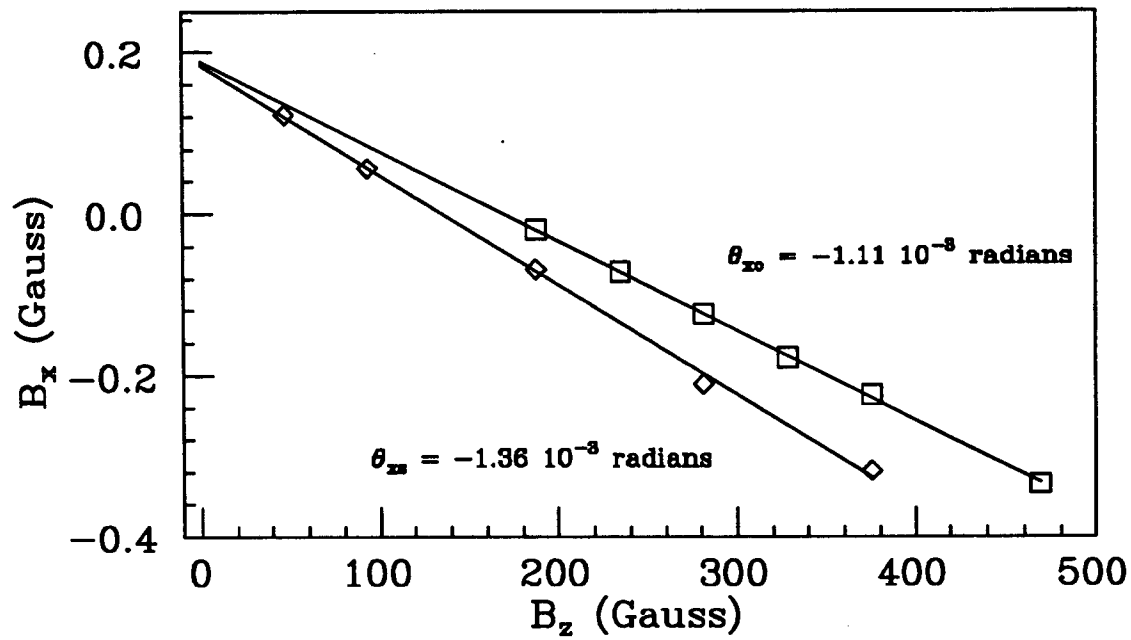

Figure 3.27: B_y correction for confinement alignment (◇) and signal null alignment (□).

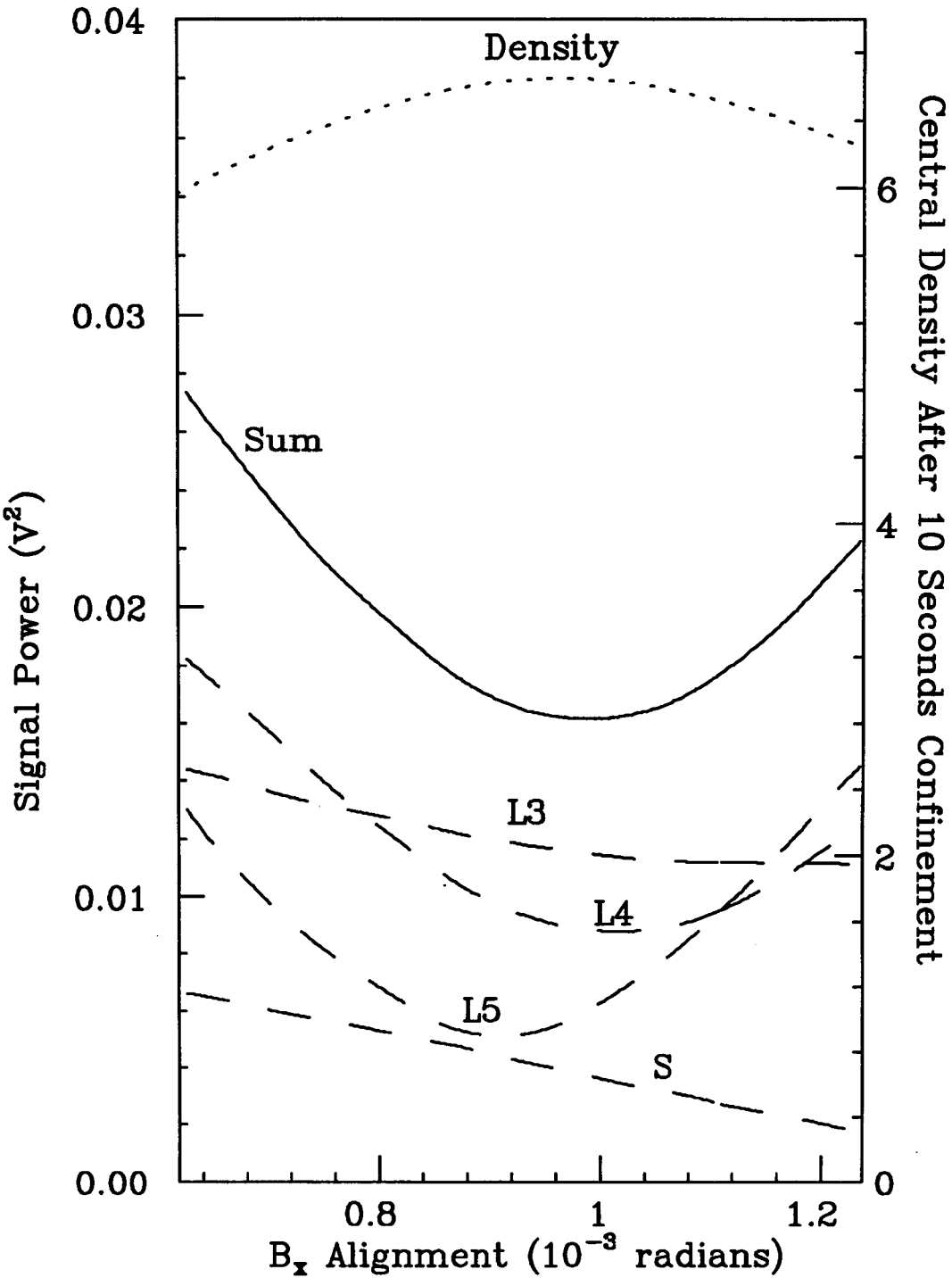

Figure 3.28: Remaining central density (dots) and summed signal power (solid line) versus θ_x. Also shown (dashes) is the signal power off each individual ring. The confinement region was L3 to L5, and $B_z = 282$ Gauss.

density) and the minima of the summed signal power are at close to the same value of θ_x.

To quantify the differences in alignment between the summed power and the signal null methods, with reference to the confinement method, I have plotted (figure 3.29) their measured difference in angle $(\Delta\theta_x, \Delta\theta_y)$ from the confinement alignment values, for three different confinement regions. I conclude that summed power alignment is closer to confinement alignment than signal null alignment is, by about a factor of two in angle. In terms of how big a difference this makes to confinement times, I estimate that use of signal null alignment will result (depending on which signals are nulled) in about a 5% reduction of remaining density, compared to the confinement alignment values. Summed power alignment is about a factor of 2 better by this criteria, as well.

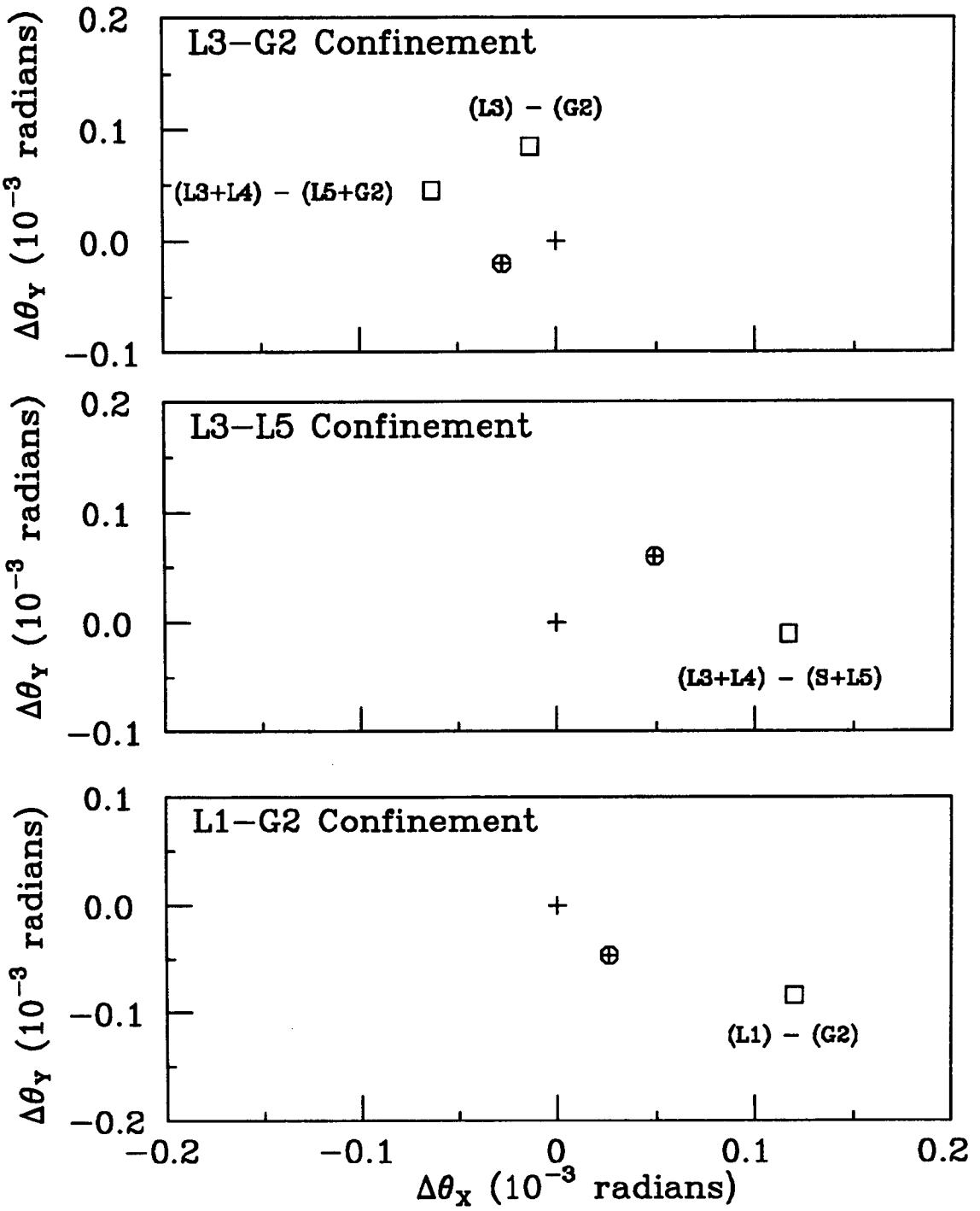

Figure 3.29: Difference (in angle) from correction given by confinement alignment, for summed power (⊕) and signal null (□) alignment techniques. The confinement regions and which rings were used for signal nulling are indicated.

Chapter 4

Symmetric Double Vortex Studies

4.1 Overview

This chapter describes experiments on two confined vortices which are symmetric in density and radius. At small separations, the vortices are observed to merge by flowing towards and wrapping around each other. At larger separations, the vortices orbit about each other until merger occurs at times up to > 100,000 orbit periods after merger. I have investigated both of these phenomena, and find that the two vortex electron system can be well characterized by a combination of results from both 2D fluid theory and plasma physics.

I describe the creation of the two vortex state, and its analysis, in section 4.2. The electron vortices used here were relatively narrow (radius $R_v/R_w \sim 0.15$), hot ($T_{\|} \sim 1.8eV$), and long ($L_p > 5R_w$). Their dynamics were investigated with two complementary diagnostics, wall sector signals and time series of $n(r,\theta)$ electron density plots. The density plots give direct measurements of vortex motions, but can usually only be taken within 500 μsecs of the injection of the vortices. The wall sector signals can be measured about 400 μsecs after injection (the delay is due to a voltage spike caused by injection), but are limited in what they reveal of the motions.

The dynamics of well-separated (i.e. not merging) vortices is described in section 4.3. I find that there exists equilibrium orbits in which each vortex orbits

about the center of the cylinder at constant radius. Some of these equilibria are linearly stable, and others are unstable. I have measured both oscillations about stable equilibria and exponential divergence from unstable equilibria.

The equilibrium positions, oscillation frequencies, and instability rates for the spatially extended vortices agree well with the predictions of a point vortex model (section 4.4). In this model, the extended vortices are replaced with point vortices of the same circulation Γ, positioned at their centers. Because this approximation eliminates the degrees of freedom describing shape distortions and surface waves, the good agreement of the model with the observations suggests that these effects do not significantly couple to the center-of-vorticity motions. This is useful because, unlike a system of 2 extended vortices, a system of 2 point vortices within a cylindrical boundary is integrable. Because of this integrability, 2D phase space maps can be constructed (section 4.4.4) which permit visualization of the fully nonlinear motions, as well as provide an understanding of the overall stability of the system.

In section 4.5 I discuss the various 2D fluid and electron plasma effects which cause the lifetime of the 2 vortex state to vary by 5 orders of magnitude. At small initial separations, immediate merger of the vortices into a single larger core is observed (section 4.5.1). Merger is a fundamental vortex property which I find to conserve the energy, angular momentum and vorticity of the electron vortex system, as predicted. Immediate merger occurs when the separations between the vortices, d_{12}, is below a critical value given by $d_{12} \sim 3.2\rho_v$, where ρ_v is the vortex radius [29]. I present some density plots of merging vortices in figures 4.10-4.11: these closely resemble plots of vortex merger from simulations [48, 68]. Immediate vortex merger can also occur at large initial separations (section 4.5.3), because the previously discussed dynamical instabilities can result in the vortices immediately drifting into each other.

For initial conditions giving scaled separations $d_{12}/2\rho_v > 1.8$, the two vortex

state can be terminated by either d_{12} decreasing or ρ_v increasing. For vortices injected onto stable equilibrium points (section 4.5.2), I find that P_θ-conserving column expansion of both vortices ultimately results in them being unstable to merger. The observed rates of expansion are consistent with those measured for single columns (section 3.2.2).

Lifetimes are anomalously low, however, for vortices injected onto unstable equilibrium points. In section 4.5.3 I present the evidence for this, and argue that it is due to a greatly enhanced rate of column expansion that occurs when the column trajectories move periodically in radius. Simple rate estimates are given, in support of a hypothesis that an effect I term 'orbital pumping' is responsible.

4.2 Creation and Analysis of Two Vortex State

I create the two vortex state by cutting a single electron column in half axially, moving the two halves to different θ-positions, and then cascading them together. This procedure is required since only a single column can be injected from the filament source. Figure 4.1 shows a schematic of the manipulations involved; there are sometimes additional steps required to generate phase-locked plots.

A two vortex experiment begins with a slow ($\sim 200\mu$sec) lowering and rising of the injection gate. After the rise pinches off a column from the filament, the column is displaced a distance D from the axis, by the growth of an l=1 diocotron mode to the desired amplitude. The wall sector signal induced by the $l = 1$ rotation can be used at this point to set the θ-phase of the column, by, for example, phase-locking to a zero-crossing of the waveform.

At the desired θ-phase, the column is cut in half longitudinally with a negative voltage applied to the central 'cut' ring. Equal density of the two cut columns is ensured by having the containment voltages on both ends equal. The θ-position of

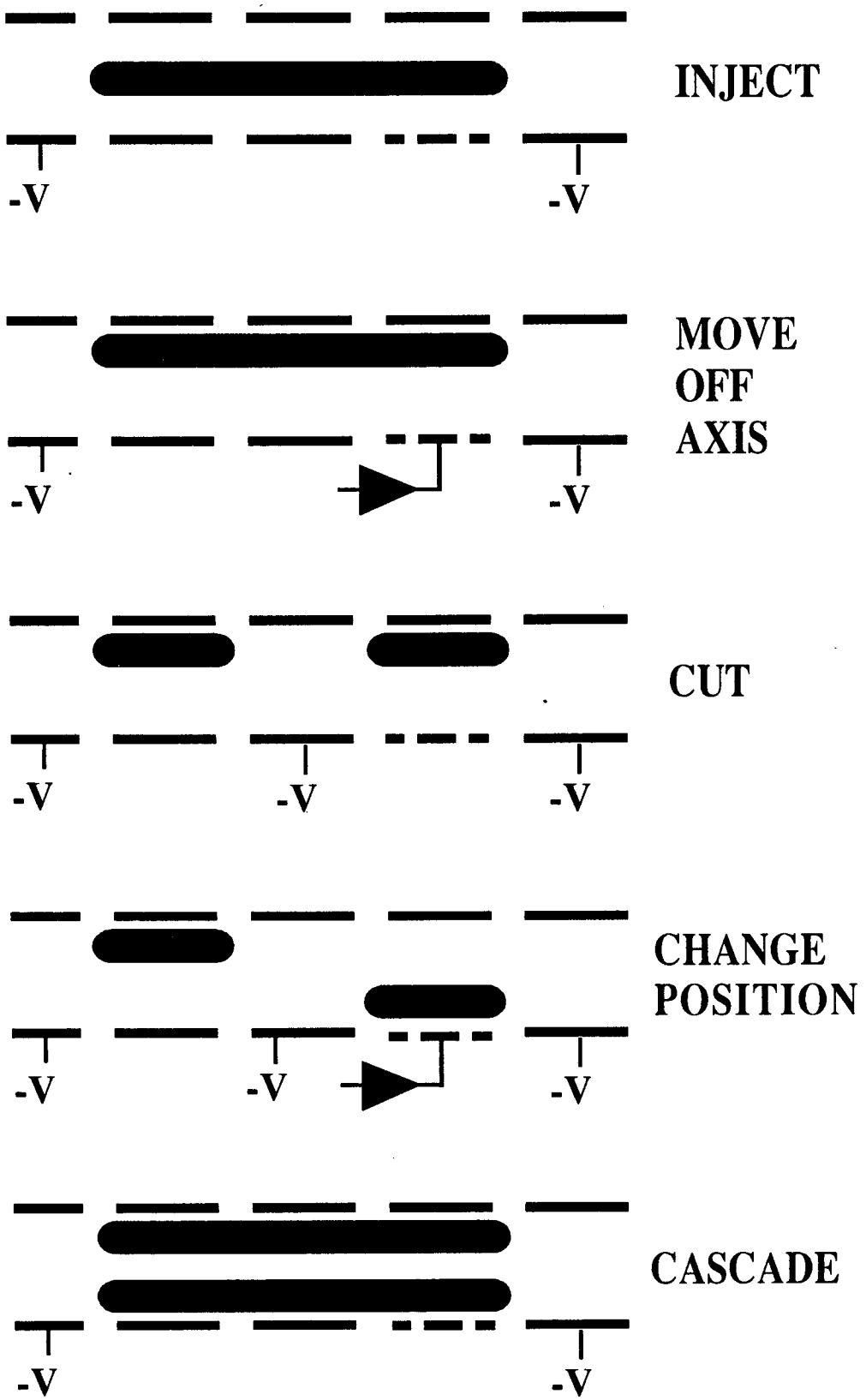

Figure 4.1: Manipulations to create two vortices from one vortex.

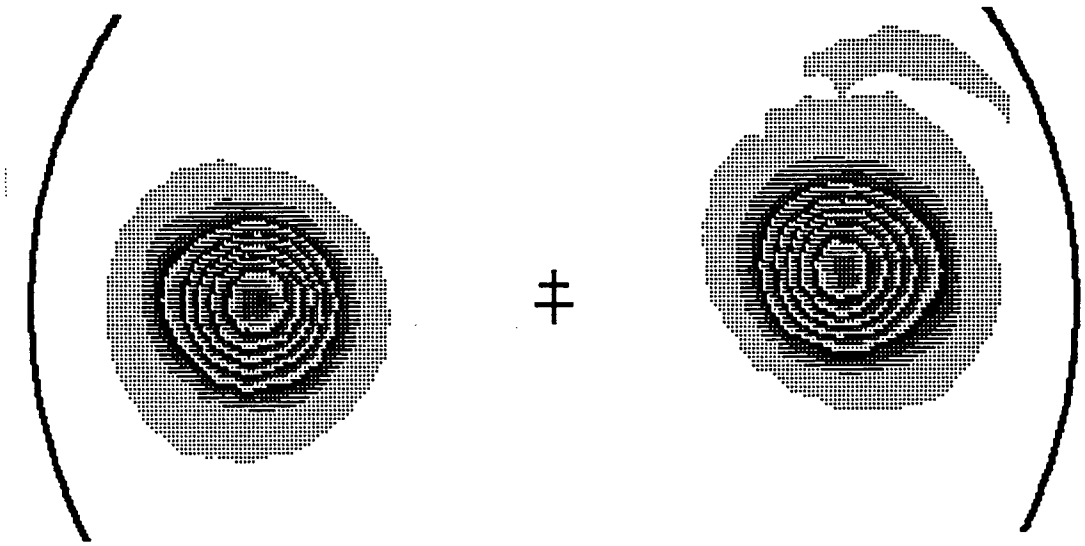

Figure 4.2: Measured plot of $\hat{\mathbf{z}}$-averaged density (or vorticity) showing two vortices. The small + marks the center-of-vorticity of the vortices, and the large + is the axis of the cylindrical conducting wall. The arcs indicate the wall radius. For these columns, $L_p \sim 21.8$ cm. Density between solid contours: $5.6 \times 10^5 \text{cm}^{-3}$.

one column with respect to the other is then changed so as to produce the desired initial condition when the columns are cascaded together. The position change is accomplished either with additional $l = 1$ feedback, or with a temporary reduction of V_c on an end ring, which will lengthen the column contained by it, thus lowering its $l = 1$ frequency and resulting in dephasing between the columns.

Finally, the cut gate is quickly ($\sim 0.7\mu$sec) lowered, and the 2 columns cascade into the original containment region and begin interacting with each other. The cascading results in a heating of $T_{\|}$ to ~ 1.8 eV. Figure 4.2 is a contour map at one time of z-averaged density $n(r,\theta)$ (i.e. vorticity) for typical columns, showing bell-shaped vorticity profiles extending over a radius R_v ~0.5 cm. The density $n(r,\theta)$ gives rise to a potential $\phi(r,\theta)$ through Poisson's equation. This results in $\mathbf{E} \times \mathbf{B}$ drift velocities $v_E(r,\theta)$ (see section 2.8). Mutual advection in this flow field results

in the two vortices orbiting around the cylinder axis, with typical frequencies $f_{orb} \approx$ 10 kHz. Additionally, each column rotates about its center of mass, at a frequency $f_{rotation} \approx 100$ kHz.

Immediate merger of the 2 symmetric vortices is observed if they are put together with a separation less than 1.6 times their diameter [29, 48]. At larger separations, the vortices are observed to orbit about each other, in a complicated fashion, until merger occurs at times up to >100,000 orbit periods after injection. I have extensively studied these orbital motions of well-separated vortices, using 2 complementary diagnostics: measurements of wall sector signals and time series of $n(r, \theta)$ density plots.

The wall sector signals are measurements of the charge induced on the sectors by the electron vortices. Their analysis gives a fast determination of the frequencies of the two-vortex state, as well as useful qualitative information on the dynamics of the two vortices. In Appendix B I describe the interpretation and analysis of wall sector signals induced by two vortices. Unfortunately, solving for the 2 vortex positions from the sector signals is a non-trivial exercise in signal processing and calibration, and accurate position measurements have yet to be extracted from this approach.

The density plots give direct measurements of the positions and shapes of extended vortices. The basic measurement here is of the z-averaged electron density which flows along B_z through a collimator hole after the end gate has been quickly brought to ground. As discussed previously in section 2.4.2, I build up plots of $n(r, \theta, t)$ from many measurements; the temporal dependence is obtained by varying the evolution time t, and the spatial dependence is obtained by varying the position r of the radially scanning collimator hole and the θ-phase of the initial condition.

After the creation of the two vortex state, I am able to create density plots

for several orbital periods, after which uncertainty in the initial conditions results in loss of phase-coherence and consequent noisiness in the plots. In my analysis of vortex motions using these plot, I reduce them by characterizing the positions of the spatially extended vortices by the coordinates $(r_1, \theta_1), (r_2, \theta_2)$ of the centers-of-vorticity. A time series of vortex positions can then be examined and fit as desired; the details of this analysis are in Appendix C.

4.3 Equilibrium Orbit Observations

I have observed equilibrium orbits about the center of the cylinder, with either $r_1 = r_2$ or $r_1 \neq r_2$, but always with $\theta_2 = \theta_1 + \pi$. In equilibrium, each vortex orbits the center of the cylinder at a constant radius and with the same frequency f_{orb}, so the two vortices remain diametrically opposed. For $r_1 = r_2$, both stable and unstable equilibria are observed. That is, if the vortices are initially displaced from the equilibrium positions, they either oscillate around the equilibrium points with frequency f_{osc}, or diverge from the equilibrium points at an exponential rate γ.

Figure 4.3 shows the observed equilibrium points r_1, r_2 for two identical vortices with $\theta_2 - \theta_1 = \pi$. Both stable ($\circ$) and unstable ($\diamond$) equilibrium points are observed. Two conventions are used here: the positions r_i are normalized to R_w, i.e. $r_i \equiv R_i/R_w$; and for the equilibrium points with $r_1 \neq r_2$ I specify $r_1 > r_2$. The lines indicate the predictions of point vortex theory, discussed below in section 4.4. The dashed line indicates stable $r_1 = r_2$ equilibria, the solid line unstable $r_1 = r_2$ equilibria, and the dotted line stable $r_1 > r_2$ equilibria.

I plot 3 examples of observed center-of-vorticity positions, relative to a frame rotating about the axis, in figure 4.4. The three classes of equilibria, two stable and one unstable, are each represented. The positions have had the orbital motion about the cylinder axis subtracted out as described in Appendix C. The directions (i.e. time

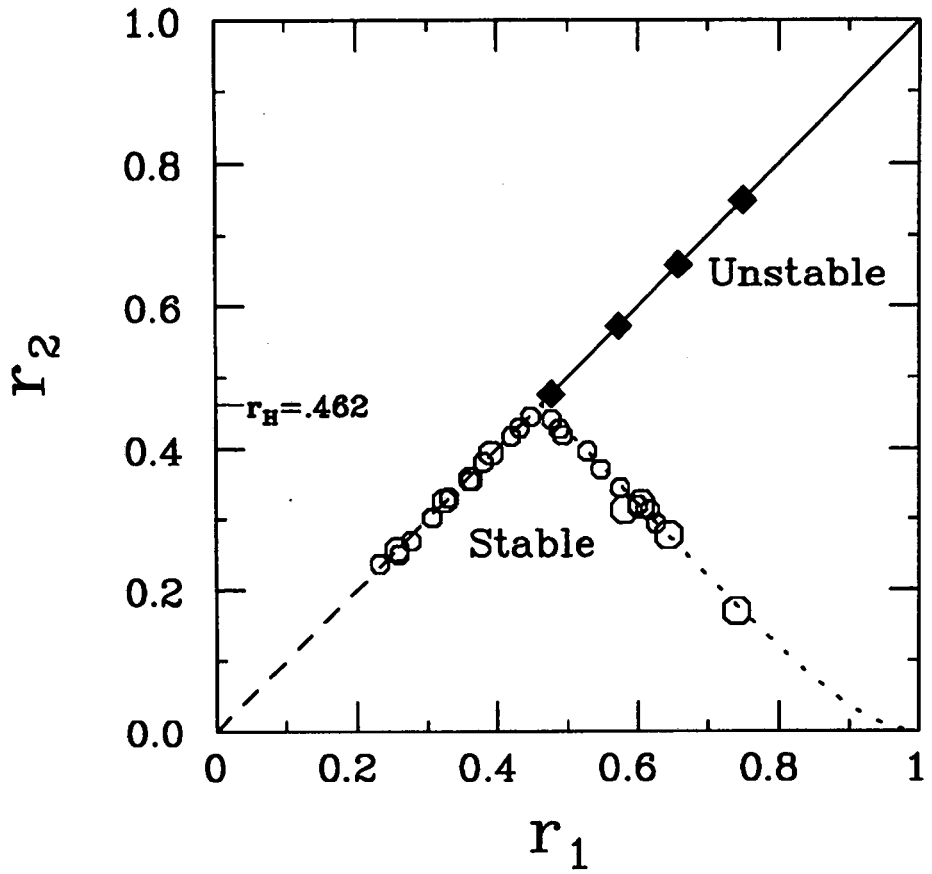

Figure 4.3: Equilibrium points for two identical vortices in a cylindrical boundary. The radial coordinates are normalized to R_w, and $\theta_2 - \theta_1 = \pi$. The symbols indicate observed stable (o) and unstable ($\diamond$) points. The lines are the predictions of point vortex theory, with the solid line indicating instability and the dotted and dashed lines stability.

ordering) of the oscillations about, or exponentiation away from, equilibrium points are indicated with arrows. The dashed line at radial position $r_H \equiv 0.462$ marks the theoretically predicted (and observed) boundary between stable and unstable $r_1 = r_2$ equilibrium points [34].

I have measured the frequencies f_{osc} at which vortices oscillate about the $r_1 = r_2$ and $r_1 > r_2$ stable equilibria. Similarly, for the $r_1 = r_2$ unstable equilibria I have measured the rates γ at which the vortices exponentiate away from the unstable points. In figure 4.5 I plot these frequencies and rates, as measured in the frame rotating about the axis, versus r_1. Data points from both density plot analysis and

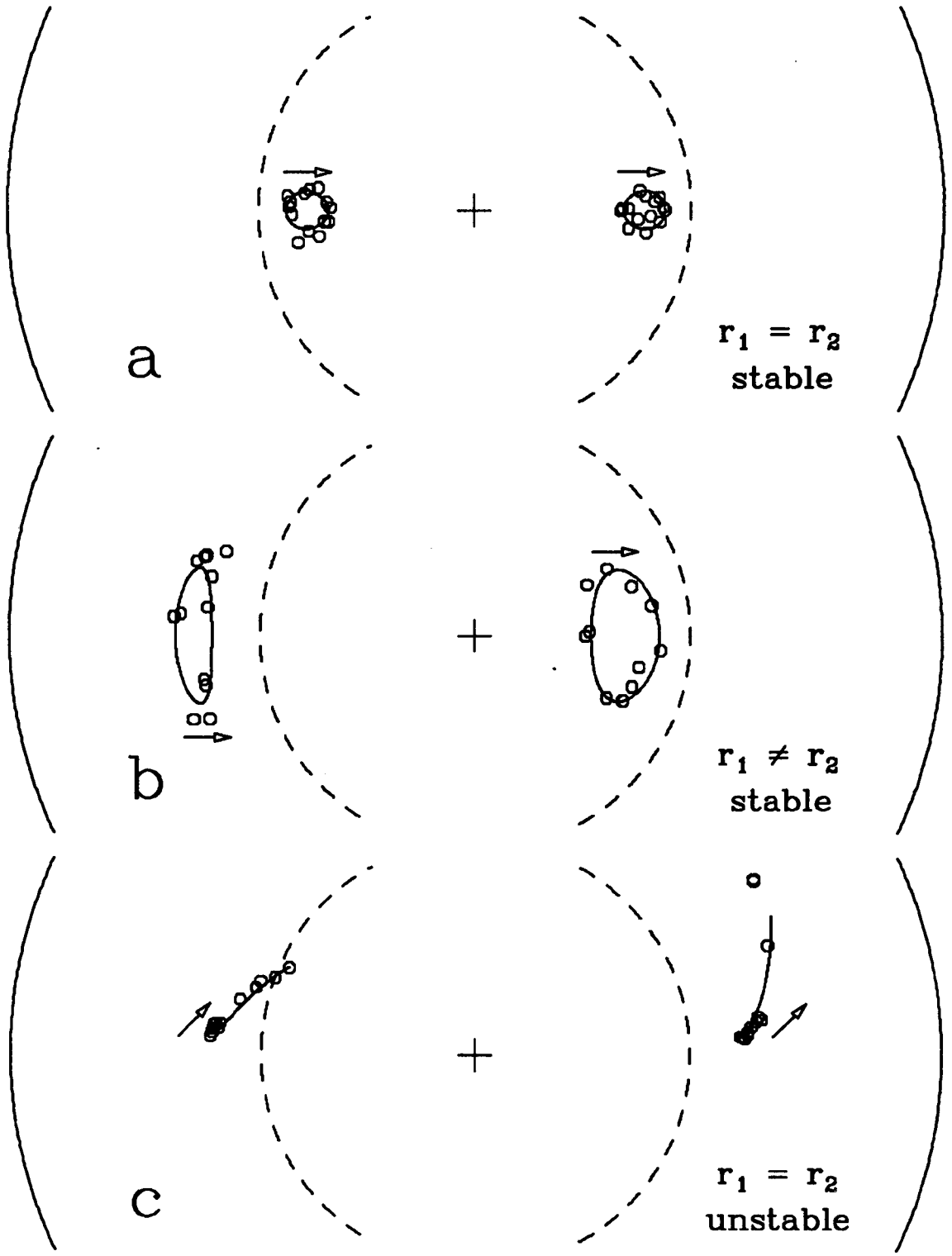

Figure 4.4: Observed center-of-vorticity positions, in a rotating frame, of vortices orbiting about three classes of equilibria. The lines are fits to the motions, as described in Appendix C, and the arrows show the directions of motion. The dashed line is $r_H = 0.462$.

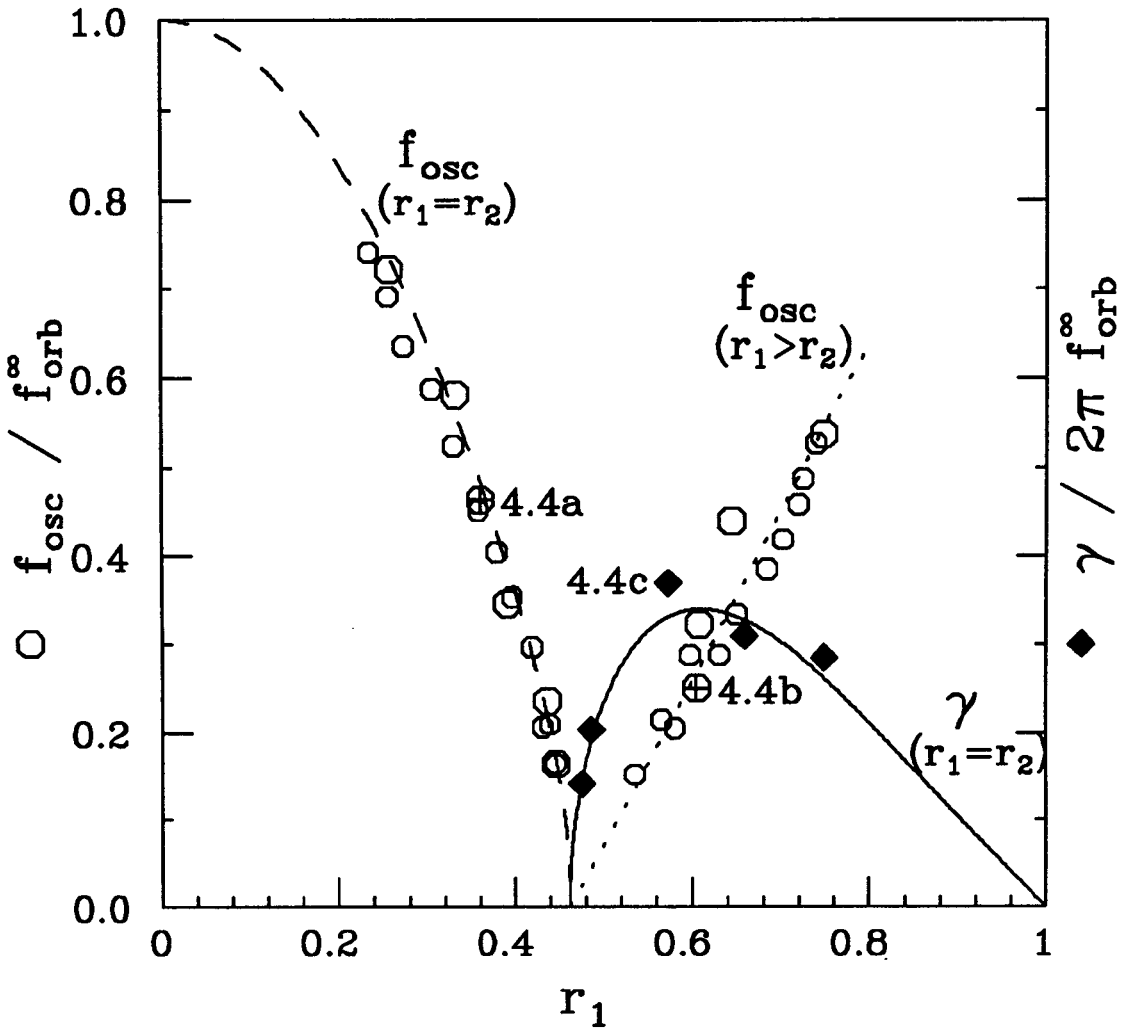

Figure 4.5: Normalized measured oscillation frequencies $f_{osc}(\circ)$ and exponential growth rates $\gamma(\diamond)$. The curves are the predictions of an analytic point vortex model, where the solid line indicates exponential growth and the dashed and dotted lines indicate oscillation frequencies. The motions corresponding to the three marked rates have been shown in figure 4.4.

wall sector signal analysis are included, as are the predictions of point vortex theory (dashed, dotted and straight lines).

The plotted frequencies and rates are normalized by the theoretical orbit frequency f_{orb}^{∞}, defined below in eq. 4.2. For $r_1 = r_2$, f_{osc} varies from approximately f_{orb}^{∞} down to zero as r_1 is increased from 0.23 to r_H. (With separations $r_1 = r_2 < 0.23$, merger occurs in a few orbits.) For small r_1, f_{osc} is approximately f_{orb}^{∞} because the vortices orbit about the center of (total) charge, independent of where this center is relative to the cylindrical wall. As r_1 approaches r_H, f_{osc} approaches 0, since the restoring forces go to zero as the influence of the images charges in the walls becomes important. For $r_1 = r_2 > r_H$, initial displacements $\Delta\mathbf{x} \equiv (\Delta r, r\Delta\theta)$ from an equilibrium point are observed to grow exponentially as $\Delta\mathbf{x} = A\mathbf{x}_+ e^{\gamma t} + B\mathbf{x}_- e^{-\gamma t}$, where $\mathbf{x}_+(\mathbf{x}_-)$ is the growing (decaying) eigenvector. Over the accessible range of unstable equilibria, I observe growth rates $\gamma/2\pi f_{orb}^{\infty} \approx 0.2$ to 0.4, as shown by the diamonds of figure 4.5. For $r_1 \neq r_2$, f_{osc} increases monotonically as r_1 increases, due to the increasing forces from the image charges.

4.4 Point Vortex Model

The observed motions of the spatially extended electron vortices are well-described by a point vortex model, where each extended vortex is replaced by a point vortex of the same circulation Γ placed at its center-of-vorticity. (A useful review of point vortex dynamics, which has been studied for over 100 years, is given by [1].) The circulation is given by

$$\Gamma \equiv \left(\frac{2\pi ce}{B}\right) 2N_L \,. \tag{4.1}$$

where the line density N_L is obtained experimentally either from a Gauss' law measurement or an integration of a 2D $n(r,\theta)$ distribution.

The point vortex model ignores the degrees of freedom describing extended

vortex distortions and surface waves, since distorted vortices would have external fields which differ from the fields of a point vortex. As can be seen in the figures of the previous section, the agreement between the predictions of the point vortex model and the observed equilibrium positions and frequencies/growth rates is quite good. This suggests that surface waves and shape distortions of the extended vortices do not significantly couple to the center-of-vorticity motion, at least when the vortices are sufficiently well separated that they are not susceptible to merger.

4.4.1 Predictions for Equilibria

The equilibrium positions for point vortices in a cylindrical boundary of radius R_w are easily solved for. For a point vortex of circulation Γ_1 at position (R_1, θ_1), the method of images says that the image charges on the cylindrical wall give the same fields as those of a fictitious point vortex of circulation $-\Gamma_1$ at $(R_w^2/R_1, \theta_1)$. Thus, the velocities of the point vortices can be readily calculated.

In equilibrium there are no radial velocities, and both vortices have the same orbit frequency about the axis of the cylinder. These requirements can only be satisfied if the two vortices are at opposite sides of the axis, i.e. $\theta_2 - \theta_1 = \pi$. Using this, one can solve for the radial positions which give the same orbit frequencies. The orbit frequency f_{orb}^{∞} of point vortex 1 is given by

$$f_{orb}^{\infty}(r_1, r_2) = \frac{\Gamma}{2\pi} \frac{1}{2\pi r_1} \frac{1}{R_w^2} \left[\frac{1}{r_1 + r_2} - \frac{1}{r_1 + 1/r_2} + \frac{1}{r_1 - 1/r_1} \right], \qquad (4.2)$$

where the three terms in the square brackets are the contributions from vortex 2, vortex 2's image, and vortex 1's image respectively. The orbit frequency of point vortex 2 is given by the interchange of the subscripts 1 and 2. The equilibrium points are therefore those which satisfy $f_{orb}^{\infty}(r_1, r_2) = f_{orb}^{\infty}(r_2, r_1)$, or equivalently the

expression

$$\frac{1}{r_1}\left[\frac{1}{r_1+r_2}-\frac{1}{r_1+1/r_2}+\frac{1}{r_1-1/r_1}\right]-\frac{1}{r_2}\left[\frac{1}{r_2+r_1}+\frac{1}{r_2+1/r_1}-\frac{1}{r_2-1/r_2}\right]=0\,. \tag{4.3}$$

Putting the left hand expression over a single denominator gives the numerator

$$(r_1-r_2)\left(1-r_1r_2-2r_1^2-2r_2^2+r_1^2r_2^2+r_1^4+r_2^4-2r_1^4r_2^2-2r_2^4r_1^2-3r_1^3r_2^3\right)\,, \tag{4.4}$$

and the roots of this expression are the equilibrium positions.

One set of roots is given by $r_1 = r_2$, but there are additional equilibrium points where $r_1 \neq r_2$. All of the physical equilibrium points (i.e. $0 \leq r_1 \leq 1$, $0 \leq r_2 \leq 1$, and r_1, r_2 real) have been previously plotted in figure 4.3 as lines (solid, dotted and dashed), with the convention $r_1 \geq r_2$. To first order in x, these new roots are given by $r_1 = .4623 + x$ and $r_2 = .4623 - x$, where x is an arbitrary value.

4.4.2 Predictions for Frequencies and Growth Rates

The stability of circular orbits of two (or more) point vortices within a circular boundary was first analyzed by Havelock in 1931 [34]. He did a linear stability analysis of the $r_1 = r_2$ equilibrium points. For two vortices, Havelock found oscillations about stable equilibria when $r_1 = r_2 < r_H$, and exponentiation from unstable equilibria when $r_1 = r_2 > r_H$, where $r_H \equiv 0.4623$. Specifically, he found that perturbations from the $r_1 = r_2$ equilibrium points evolved as $e^{\lambda t}$, where

$$\lambda^2 = \left(\frac{\Gamma}{4\pi R_1}\right)^2\left(1-\frac{4r_1^2}{(1+r_1^2)^2}\right)\left(7-\frac{8}{1-r_1^4}+\frac{4r_1^2}{(1-r_1^2)^2}\right)\,, \tag{4.5}$$

which is negative (giving stability) for $r_1 < .4623$ and positive for r_1 greater than this. Havelock's predictions for frequencies and growth rates have been previously shown, in figure 4.5.

I have extended Havelock's analysis to the equilibria with $r_1 \neq r_2$, and find stable oscillations about these points. The details of the calculation are in

Appendix D. While in principle it is possible to display analytic expressions for these oscillation frequencies, as in equation 4.5, it is not practical to do so here. The reason for this is that the analytic expression for the $r_1 \neq r_2$ equilibrium points, about which the analysis is done, is given by the roots of the fourth order polynomial of equation 4.4. The analytic expression for these roots alone is too large to be worth reprinting! However, the stable oscillation frequencies predicted by the linear analysis are shown in figure 4.5.

4.4.3 Extension To Temperature Asymmetric Case

I have found that $T_{||}$ asymmetries between the two electron columns can have a strong impact on their dynamics. For example, I have injected columns with an asymmetry of $\Delta T_{||} \approx 1.0$ eV onto $r_1 = r_2 = 0.36$ stable equilibrium points. The columns were found to oscillate not about these points, as would be expected for point vortices and for $T_{||}$-symmetric columns, but about $r_{cold} = .319$ and $r_{hot} = .405$. The effect of temperature asymmetries can be incorporated into the point vortex model, however, and good agreement is seen between the predictions of this extended model and the observed dynamics.

As has been discussed in section 3.2.1, changing the $T_{||}$ of a column will change the frequency shift between the measured and infinite-length $l = 1$ frequency, $\Delta f_{l=1} = f_{l=1} - f_{l=1}^{\infty}$, due to finite length effects. The simplest model for $T_{||}$-asymmetric columns, therefore, is one which uses the point vortex approximation but additionally gives the hotter vortex a frequency shift $\Delta f_{l=1}^{hot}$, arising from the difference in the orbit velocities of the columns.

The equilibrium points (r_{hot}, r_{cold}) predicted by this extended model are found, as in the $T_{||}$-symmetric case, by solutions to

$$f_{orb}^{\infty}(r_{hot}, r_{cold}) - f_{orb}^{\infty}(r_{cold}, r_{hot}) = \Delta f_{l=1}^{hot} \,. \tag{4.6}$$

When the measured frequencies of the experimental example were plugged in, the predicted equilibrium points were at $r_{cold} = .323$ and $r_{hot} = .393$, in reasonable agreement with the measured values.

I have also checked the agreement of the extended model for the orbit shapes about the new equilibrium points. This was done using a numerical simulator of point vortex motions, which integrates the equations of motion forward in time using a Bulirsch-Stoer algorithm [59]. I found that adding the measured frequency offset to one of the two vortices results in orbit shapes very similar to the ones observed.

Temperature asymmetries can obviously play a large role in the dynamics, and it is one which has no counterpart in the fluid analogy. In the experiments of this dissertation involving several vortices, I have always been careful to put the vortices together such that they both have the same frequency shifts. With the symmetric vortices of this chapter, this is done automatically if the vortices have the same lengths before and after they are cascaded together. With the asymmetric vortices of Chapter 5, it was found necessary to measure the frequency shifts and equalize them by adjusting the confinement potentials, which alters the column lengths.

4.4.4 Energy and Angular Momentum Plots

Interestingly, the fully nonlinear motion of 2 point vortices within a cylindrical boundary can be understood from 2D phase space maps, since the system is integrable. This is because there are four variables $(r_1, \theta_1, r_2, \theta_2)$ and two constants of the motion $(\mathcal{P}_\theta, \mathcal{H})$, the angular momentum and the interaction energy per unit length.

Angular momentum conservation [52] has been discussed in section 2.6.1. One can define a simple scaled angular momentum P_θ for two point vortices by

$$P_\theta \doteq \frac{\mathcal{P}_\theta}{\mathcal{P}_0} = \sum_{i=1,2} (1 - r_i^2) \,, \tag{4.7}$$

where $\mathcal{P}_0 = (eB/2c)R_w^2 N_L$ is the angular momentum of an on-axis line charge (point vortex). Similarly, from the 2D energy $\mathcal{H}_\phi$ (equation 2.8) of point vortices one can define a scaled interaction energy H with

$$H = \frac{\mathcal{H}_\phi}{\mathcal{H}_0} = \sum_{i=1,2} \ln(1 - r_i^2) + \ln\left[1 + \frac{(1 - r_1^2)(1 - r_2^2)}{r_{12}^2}\right], \tag{4.8}$$

where $r_{12} = |\mathbf{r_1} - \mathbf{r_2}|$ and $\mathcal{H}_0 = e^2 N_L^2$ is a characteristic energy. H and P_θ are, of course, also conserved for fluid point vortices [1].

The predicted motions of the point vortices can be visualized from representations of $H(r_1, \theta_1 - \theta_2, P_\theta)$. For a contour map at a given P_θ, the 2D contours of energy H display the $(r_1, \theta_2 - \theta_1)$ values that a two-vortex system with that energy will trace out during its evolution. (There is no information on the absolute θ-positions, since as a consequence of the rotational symmetry of the system, only the difference in the θ-coordinates matters in H.)

There are three distinct map topologies over the accessible range of $0 < P_\theta < 2$. I display examples of these in figures 4.6 through 4.8. For $P_\theta > 2(1 - r_H^2)$, there is a minimum energy stable equilibrium (an O-point) with the two vortices symmetrically opposite each other, at $\theta_1 - \theta_2 = \pi$ and $r_1 = r_2$. There is also an infinite energy point where the vortices are at the same radial and θ coordinates. This topology can be seen in figure 4.6.

When P_θ is decreased (i.e. the vortices are moved radially outward), the O-point becomes shallower. For $1 < P_\theta < 2(1 - r_H^2)$, the symmetric equilibrium has become an unstable saddle point (an X-point), with two new O-points existing at $r_1 \neq r_2$ values (see figure 4.7). As P_θ is decreased further, the O-points move further from the X-point, until for $P_\theta < 1.0$ there are no stable equilibria (as in figure 4.8).

Also plotted on the phase space maps are the experimentally measured center-of-vorticity coordinates $(r_i, \theta_i - \theta_j)$ for evolutions with the corresponding P_θ. (When these coordinates are plotted, the two sets of vortex coordinates are distinguished

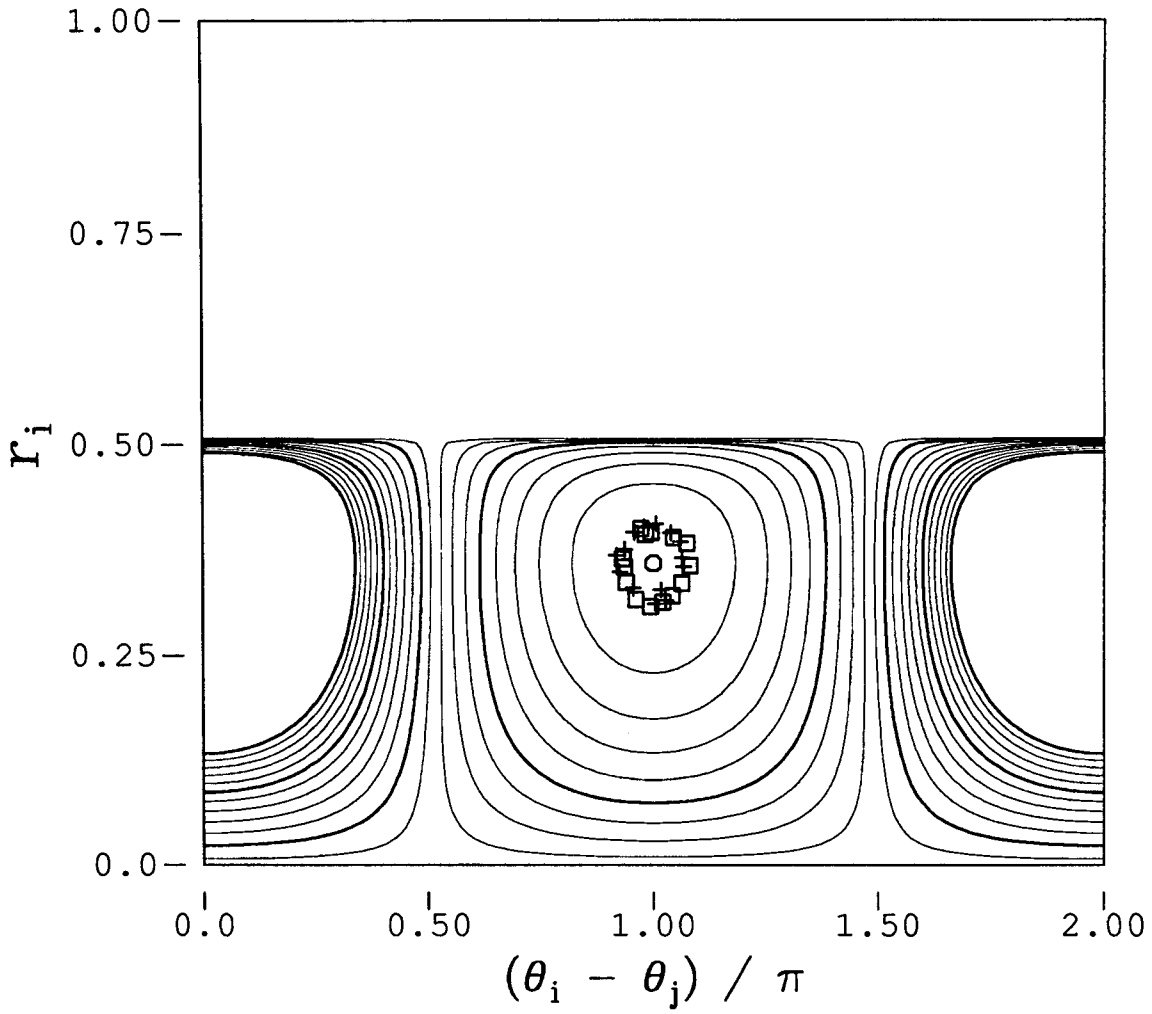

Figure 4.6: Contours of scaled energy $H(r_i, \theta_i - \theta_j)$ for $P_\theta = 1.74$. The contour interval is $\Delta H = 0.05$. The symbols $(\square, +)$ show measured center-of-vorticity values for an initial condition of $P_\theta = 1.74$. The O-point is also shown.

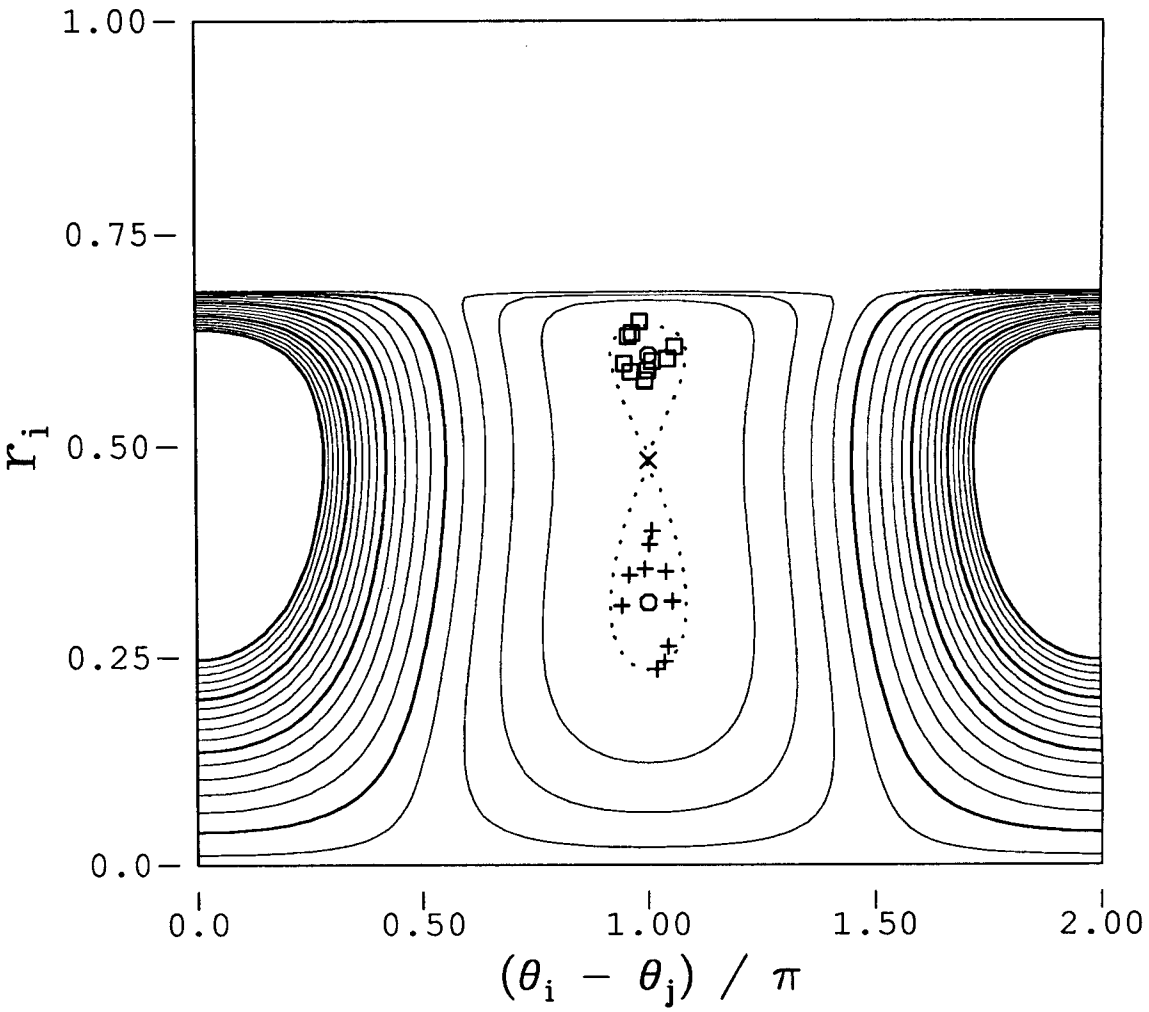

Figure 4.7: Contours of scaled energy $H(r_i, \theta_i - \theta_j)$ for $P_\theta = 1.53$. The contour interval is $\Delta H = 0.05$, but one additional energy contour (dots) at the value of the saddle point is shown. The positions of the two O-points and one X-point are shown.

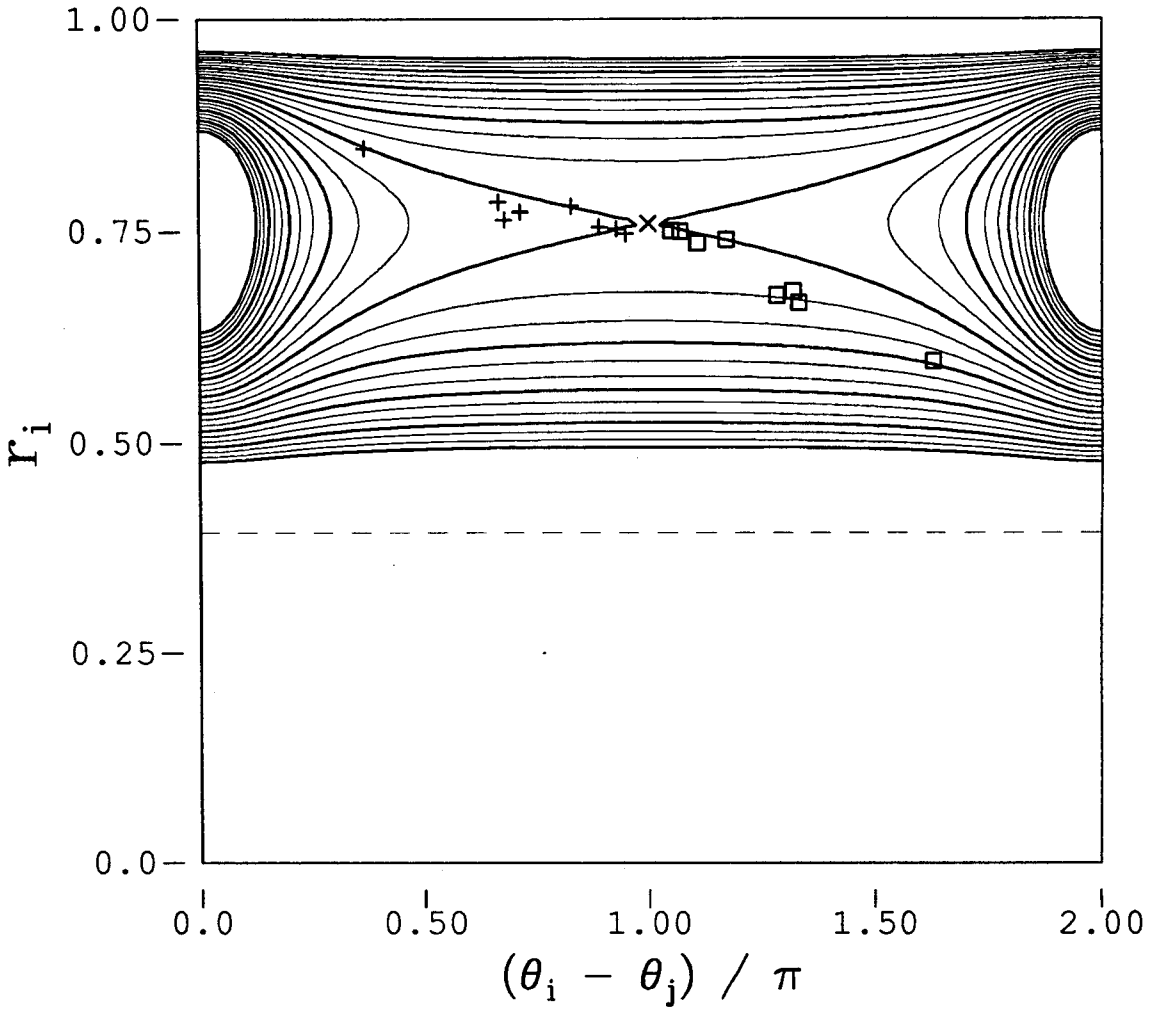

Figure 4.8: Contours of scaled energy $H(r_i, \theta_i - \theta_j)$ for $P_\theta = 0.85$. The contour interval is $\Delta H = 0.05$. The dashed line indicates the boundary of accessible regions.

by using different symbols.) In figure 4.6, the centers are observed to oscillate once around the stable equilibrium while the vortices orbit 2.7 times around the cylindrical center, with a measurement error corresponding to $\delta H \leq .01$. In figure 4.7, 3/4 of an oscillation about an asymmetric equilibrium is observed, with a larger measurement error of $\delta H \sim .02$ due to the additional uncertainties introduced while creating the $r_1 \neq r_2$ initial condition. In figure 4.8, the vortices exponentiate away from the unstable equilibrium, with the displacements being largely in the θ-direction. The large measurement errors at long times reflect the difficulty in repeatably following the exponentially unstable trajectories with density plots.

Distortion Energies

For spatially extended vortices, the 2D energy $\mathcal{H}_\phi$ will include self-energy and interaction energy terms which depend on the shapes of the vortices. Experimentally, I observe elongations away from circularity of $\leq 10\%$ in general, and up to 30% for $r_1 = r_2 \sim 0.23$ (near merger). These time-varying eccentricities have not, however, been observed to cause noticeable departures from the predictions of the point vortex model. This result is perhaps because the energies involved in elongations are relatively small: using a moment model [48], I estimate $\delta H \sim 0.002$ and 0.02 for elongations of 10% and 30% respectively.

I have additionally found that intentionally induced elongations do not significantly affect the orbit dynamics, as diagnosed by the wall sector signals. Before putting the two vortices together, I grew an $l = 2$ diocotron wave on one vortex, on both, or on neither. The wave gave elongations of about 5%. I then looked for changes in the sector signals depending on whether or not the $l = 2$ mode was present. I failed to discern any changes in the wavesignal resulting from the $l = 2$ perturbation.

Energy and Angular Momentum Manipulations

The double vortex state can be manipulated by external control of the overall energy and angular momentum of the system. Previous work on the dynamics of a single vortex has established that resistive destabilization [71] and active feedback [70], which change P_θ and H, cause the observed motions to evolve accordingly. I find similar effects for the double vortex state.

For example, a resistance between azimuthal sections of the wall will dissipate the energy of the system. If a resistance is switched on when two vortices are near stable equilibrium points, the vortices will remain near stable equilibria while the equilibrium orbit radii vary with time. During an evolution with initial vortex positions of $r_1 = r_2 \sim 0.3$, the radii were observed to increase to $r_1 = r_2 = r_H$, after which r_1 increased until vortex 1 was pressed against the wall, while r_2 had decreased to $r_2 \sim 0.1$. This technique has been used to shift two vortices from one stable equilibrium to another with lower P_θ.

4.5 Lifetime of the Two-Vortex State

I observe that, depending on the initial conditions, the two-vortex state can last anywhere from less than one orbit period to $> 10^5$ orbits. It is terminated by merger of the two vortices, resulting in a single vortex core surrounded by filaments which eventually form a low-density halo about the core. It is straightforward to diagnose the time it takes to merge, τ_{merge}. For short merger times ($< 300\mu$sec), τ_{merge} is defined from density plots as the time where the vortex cores have fused; at longer times, it is defined to be the time at which the f_{orb} components of the sector probe signal abruptly disappear.

In figure 4.9, I plot τ_{merge} versus r_1 for two symmetric vortices injected at equilibrium positions $r_1 = r_2$, at a magnetic field of $B_z = 188$ Gauss. For the

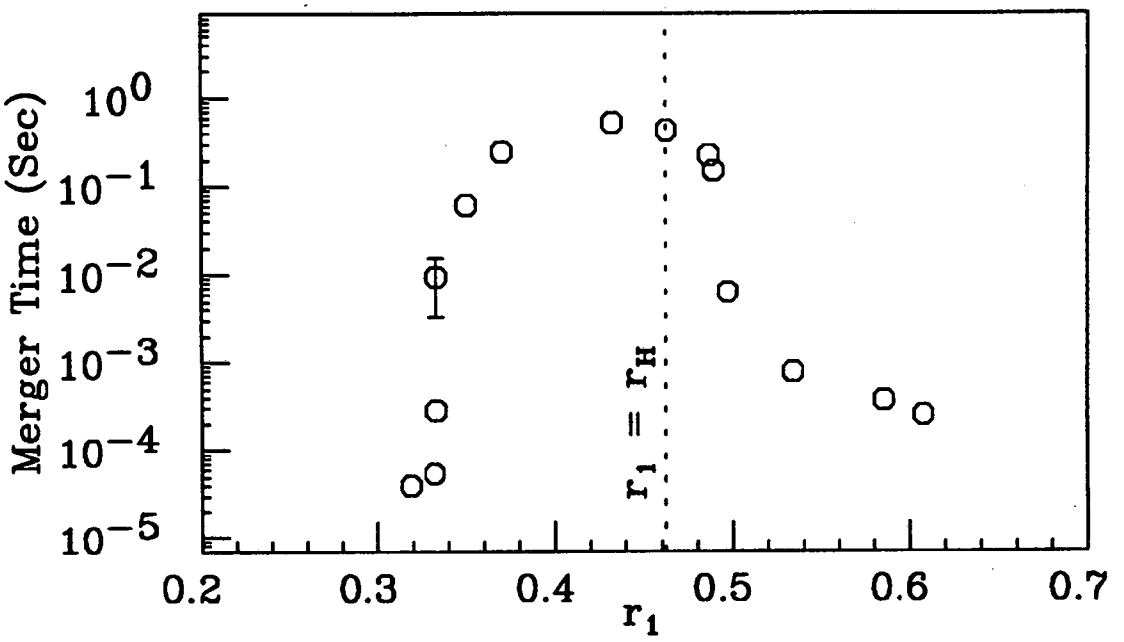

Figure 4.9: Merger time versus separation for two vortices injected at $r_1 = r_2$. The observed statistical scatter was smaller than the symbols except for the separation with the displayed error bar. $B_z = 188$ Gauss.

smallest separations, the vortices are immediately susceptible to a pairing instability (see section 4.5.1). As the separation is increased, the lifetime jumps up 4 orders of magnitude, reaches a maximum near $r_1 \approx r_H$, and then precipitously drops. At these separations, the two-vortex state is terminated by the previously discussed (section 3.2.2) column expansion, which results in the expanded columns becoming susceptible to the pairing instability. The drop above r_H is believed caused by a strong increase in the rate of the expansion, due to motions of the columns in the radial direction. These points will be discussed in section 4.5.2. At the largest separations, the previously discussed Havelock dynamical instability results in trajectories which have the vortices quickly approaching each other close enough to merge. This boundary effect, as well as other influences the boundary can have on merging, will be discussed in section 4.5.3.

4.5.1 Pairing Instability

Merger is a fundamental vortex property. When two like-signed spatially extended vortices approach close enough, they are susceptible to a pairing instability which causes them to wrap into a single larger core, accompanied by the ejection of filaments. There have been many theory papers on this instability (see, for example, [61, 64, 48, 49]), which have used analytic theory, moment models and numerical simulations to investigate it. These have established that the equilibrium solution of closely-separated vortices consists of them elongating towards and orbiting about each other. As the separation between them is decreased, the elongation becomes more pronounced until ultimately a separation is reached where there isn't any stable equilibrium. At this point, the two vortices flow towards and wrap around each other, ejecting narrow filaments of vorticity in the process. This merger of inviscid vortices is, in theory, predicted to conserve the energy, angular momentum, and all moments of the density. The enstrophy Z_2 is the second moment, given by

$$Z_2 \equiv \frac{\int dr \int r\, d\theta\; n^2(r,\theta)}{\left[\int dr \int r\, d\theta\; n(r,\theta)\right]^2} \,. \tag{4.9}$$

Figure 4.10-4.11 is a series of density plots showing the merger of two electron vortices initially placed close together. There is close agreement between these plots and the results of simulations [48, 68]. Note that the merger is a 'wrapping around', and that the cores of the merging vortices at $t = 76$ μsecs still retain their separate identities.

For these merging vortices, I have plotted the observed variations versus time of total electron number N_e, angular momentum P_θ, energy H_ϕ, and enstrophy Z_2 in figure 4.12. The solid symbols correspond to the density plots shown in figures 4.10 and 4.11, and the quantities have been normalized to the values measured at $t = 0$.

The energy, angular momentum, and total density all appear to be conserved within the scatter ($\pm 1\%$) of the experimental measurements – there is a hint that

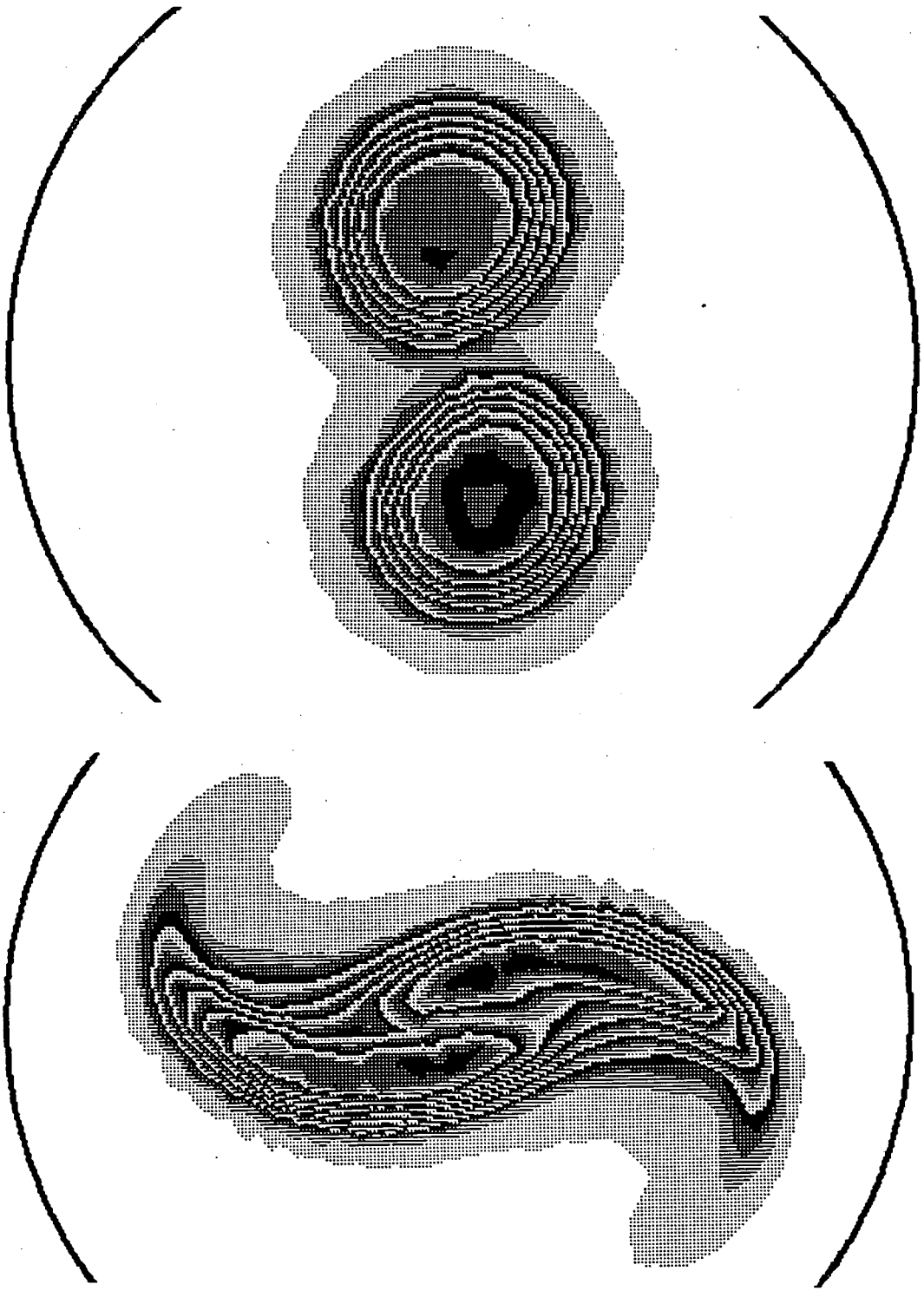

Figure 4.10: Density plots of two symmetric vortices unstable to the pairing instability. Times: t = 0 and 16 μsecs. Density between solid contours: $2.9 \times 10^5 \mathrm{cm}^{-3}$.

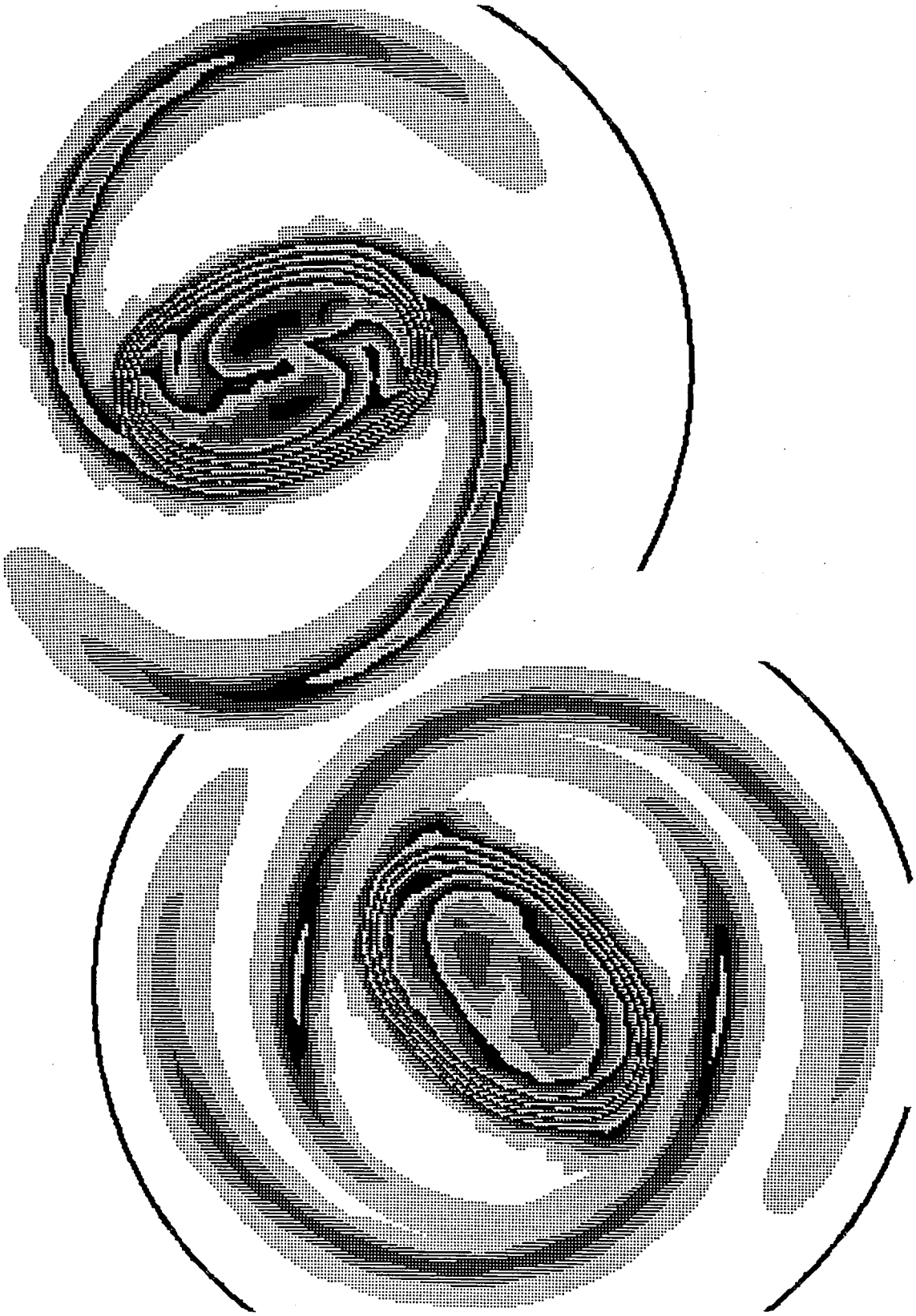

Figure 4.11: Pairing instability at t = 41 and 76 μsecs.

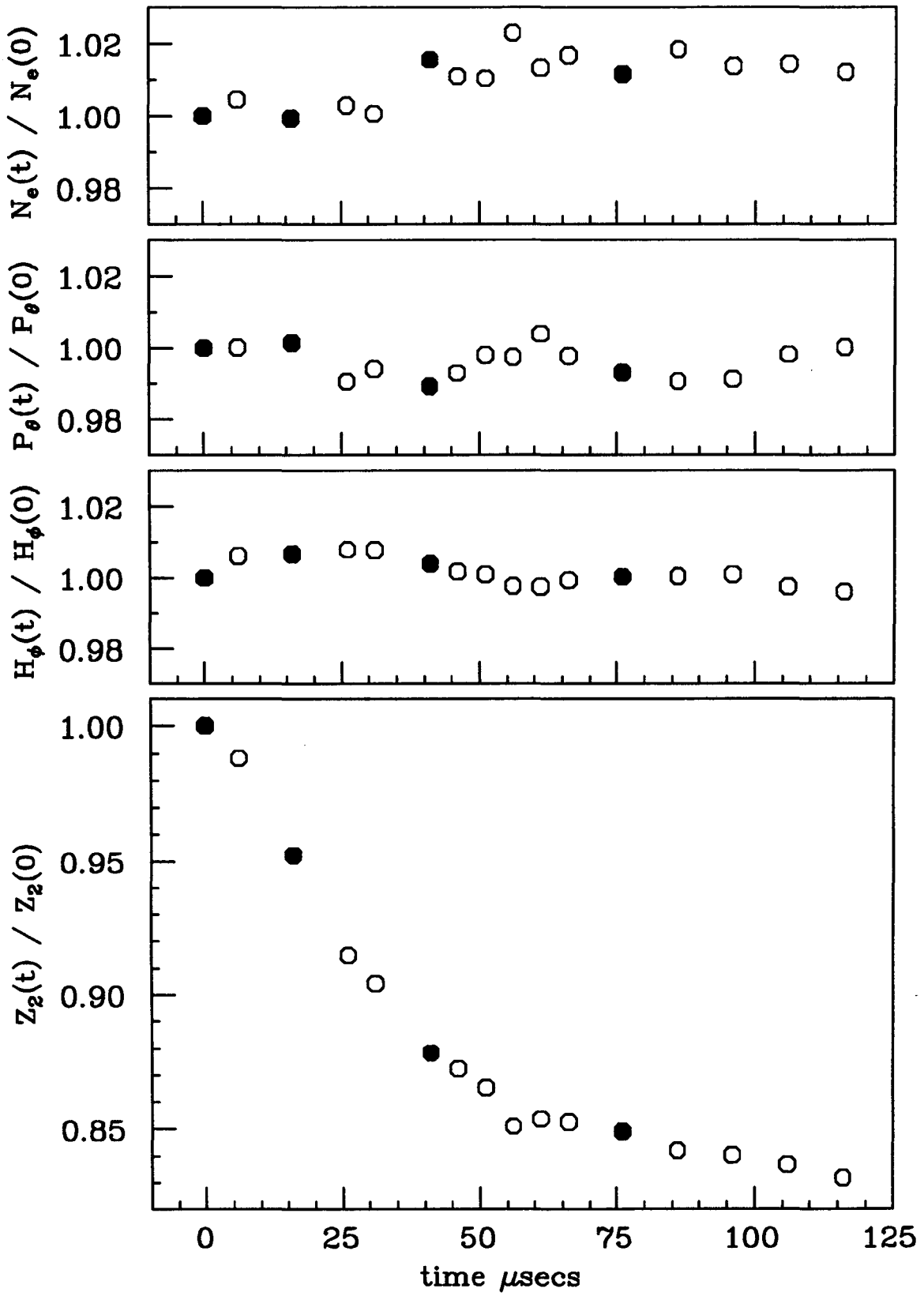

Figure 4.12: Total density, angular momentum, energy and enstrophy variations during merger. The solid symbols indicate values measured from the plots of 4.10 to 4.11.

total density drifts upward a percent or two, but this is certainly instrumental. The enstrophy, however, decreases to 82% of its initial value. Much, if not all, of this decrease is due to the 'coarse-graining' of the increasingly fine spatial scales by the collimator hole. The size of this hole is indicated in figure 5.2; its size sets the minimum spatial scales resolved. The evolution of enstrophy in electron vortices undergoing instabilities is an interesting topic which I do not have the space to go into here – see, however Huang [36].

Two simulations of vortex merger, with very similar initial conditions to those of figure 4.10, have been published in the literature. They are figure 1 of Melander *et. al.* [48], from a high-resolution direct numerical simulation, and figure 1 of Waugh [68], from a contour dynamics simulation featuring 8 contour levels. These simulations closely resemble figures 4.10-4.11.

While vortex pairing has been often observed in conventional fluids experiments, with perhaps the first clear evidence for it from Freymuth [30], viscous and boundary effects have usually resulted in non-ideal behavior being observed. One example of this is the experiments of Cardoso, Marteau and Tabeling [7], who used thin layers of electrolyte to study decaying quasi-2D turbulent flows and found strong dissipation of energy and peak vorticity to occur. Another example is the rotating water tank experiment of Griffiths and Hopfinger [32], where for one sign of vorticity merger was observed to occur for all initial separations. In contrast, a merger experiment with electron vortices has found significantly better agreement with the predictions of theory [29].

This experiment, which studied the onset of the pairing instability for electron vortices, injected vortices of varying radii onto Havelock-stable (i.e. $r_1 = r_2 < 0.46$) equilibrium point, and measured τ_{merge} as the separation was increased. The vortices were observed to merge immediately for separations of less that 1.4 vortex diameters,

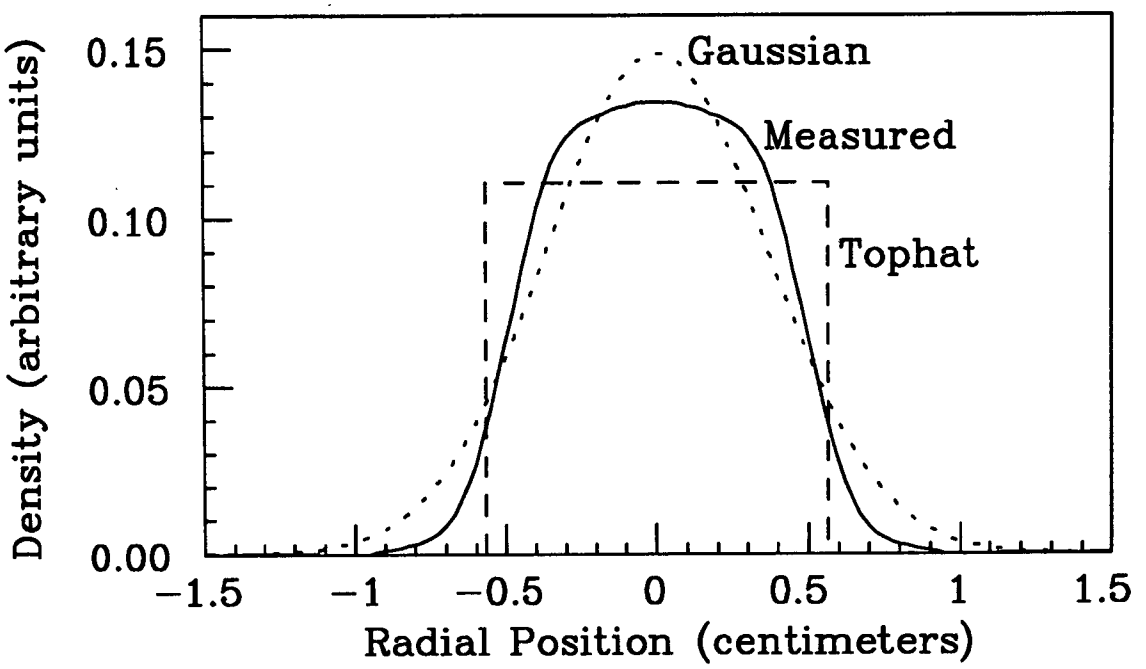

Figure 4.13: Typical measured radial profile of an electron vortex before merger, plus top hat (dashes) and Gaussian (dots) profiles fitted to it.

and to orbit for more than 10^5 orbits for separations greater than 1.8 diameters. The theory work has predicted critical separations for this instability in the range of 1.43 to 1.7 vortex diameters [64, 62].

The experiments also established that the vortex diameter was the relevant lengthscale, since the merger curves for vortices with different radii overlay each other when the separation between them was scaled by their radius. Before showing this result, it is necessary to discuss how the radius of a vortex is determined. In figure 4.13 I show a typical measured radial profile, plus the top hat (step function) and Gaussian profiles that are the best fit to this profile. One can see that the observed profile is neither Gaussian nor top hat; I call it a 'bell-shaped' profile.

There is no obvious uniformly applicable definition for the radius of a vortex with a profile like the one shown. The vortex radius R_v definition of a 2D distribution

$n(r,\theta)$ decided upon by Fine *et.al* [29] is

$$R_v \equiv \frac{3}{2}\frac{1}{N_L}\int_0^{r_{cut}} r'\, dA\, n(r,\theta)\ , \tag{4.10}$$

where the $(r-\theta)$ integral is over the area of the vortex and r' is centered on the center-of-vorticity of it. This is simply a density-weighted radial integral from the center of the vortex, ending at r_{cut}, defined to be the vortex edge. With sharp-edged profiles the position of r_{cut} is given as the point where the density goes to zero; in Chapter 5 I discuss r_{cut} for less sharp profiles. The factor of 3/2 is included to ensure that a top hat profile with radius R has $R_v = R$. The symbol I use for R_v normalized to R_w is not r_v, but $\rho_v \equiv R_v/R_w$, since r_v could be confused with center-of-vorticity positions, and since ρ is a symbol which has been commonly used for vortex radius.

Figure 4.14 shows merger curves for vortices with different values of ρ_v, where the separation D_{ij} between the vortices has been scaled by $2\rho_v$. I define d_{ij} to be the (normalized) distance between vortices i and j, i.e. $d_{ij} \equiv D_{ij}/R_w$. The vortex radius is indicated by the different symbols. The data shown had $B_z = 375$ Gauss and $r_1 = r_2 < 0.46$, except for the circles, which is the $r_1 = r_2 < 0.46$ data of figure 4.9, and had $B_z = 188$ Gauss.

It is apparent that the scaled merger curves for different ρ_v overlay each other, and give a critical separation for immediate merger of $d_{12} \sim 1.6 \cdot (2\rho_v)$. As the separation is increased, the two-vortex state lifetime increases dramatically until it reaches a maximum and levels off. In the next section I discuss the lifetime of vortices not immediately unstable to the pairing instability.

4.5.2 Column Expansion and Lifetime of the 2 Column State

I have determined that the lifetime of columns injected into stable equilibrium points opposite each other is limited by expansion of the individual columns, which

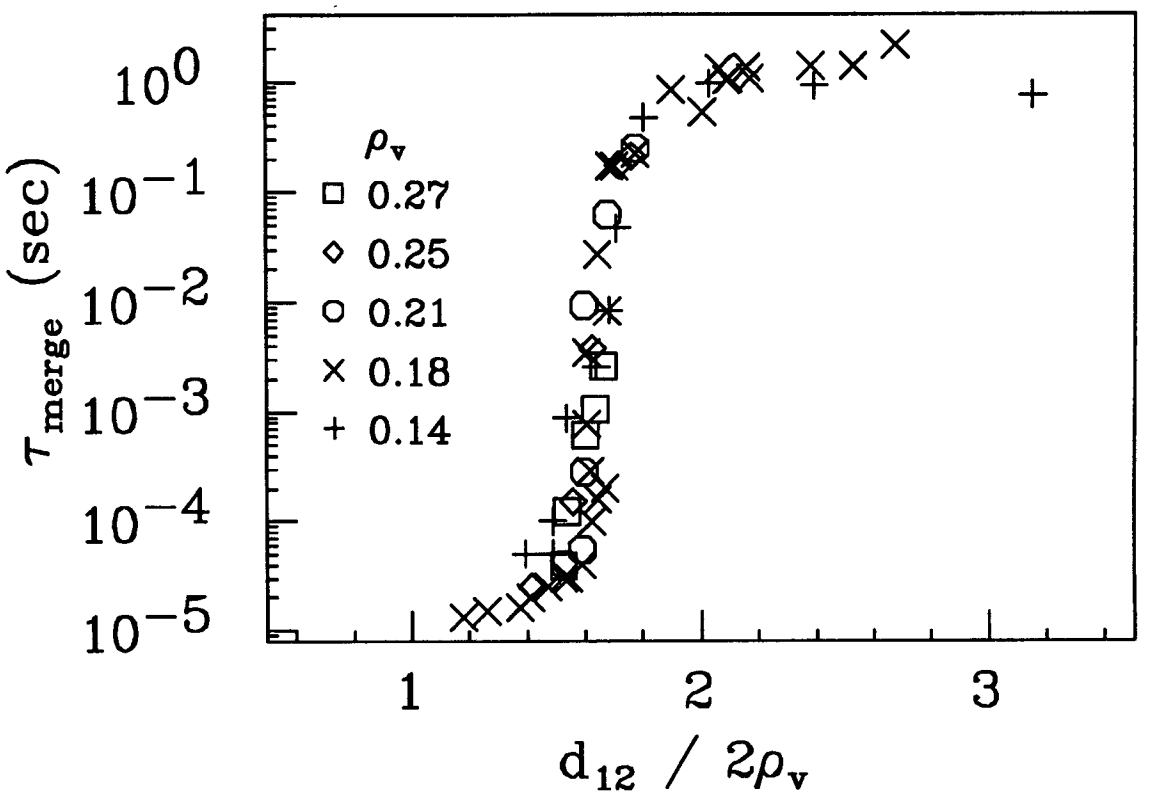

Figure 4.14: Merger time versus separation d_{12}, scaled by vortex diameter $2\rho_v$. The vortex radius of each symbol is indicated. $B_z = 375$ G and $r_1 = r_2 < 0.46$ except for the circles, for which $B_z = 188$ G.

ultimately causes them to be susceptible to the pairing instability. The process can be directly imaged under certain conditions. For stably orbiting vortices, the sector probe signal is a sinusoid at frequency $2f_{orb}$ (as shown in figure B.1). By switching all sectors and containment rings to ground, and only at a later time switching a sector to an amplifier, it is possible to monitor the evolution of the wall signal without unnecessarily perturbing the two-vortex state. I have found that no other frequency components develop, which means that it is possible to extend the density imaging technique to late times by phasing off $2f_{orb}$.

Figure 4.15 show a plot of two vortices injected at $r_1 = r_2 = 0.33$, and the same vortices 3 seconds later. During the containment time, column expansion and movement towards the axis has occurred to the vortices, exactly as has been

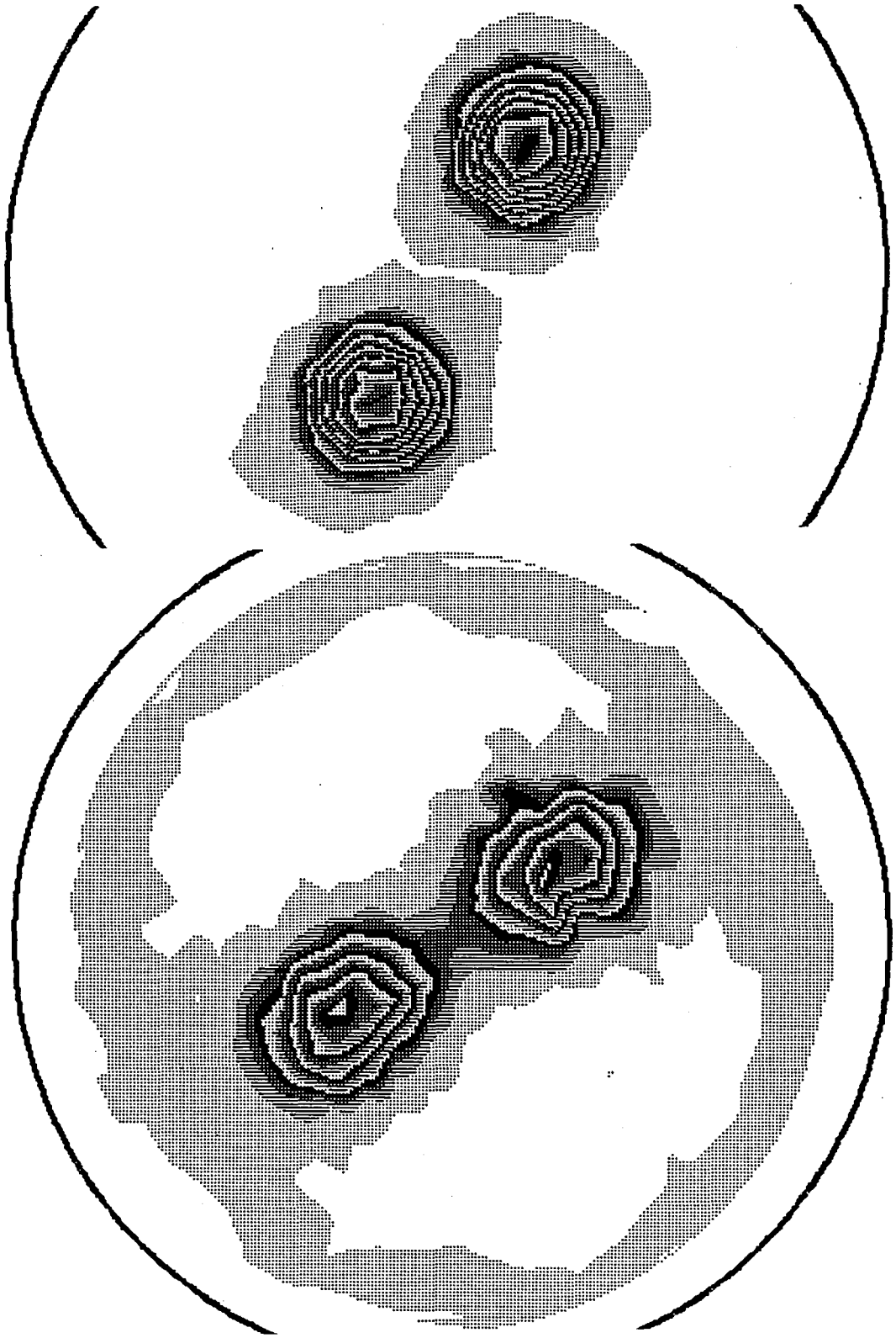

Figure 4.15: Density plots showing the long-time evolution of the stable two vortex state. The first shows the vortices after injection, and the second is 3 seconds later. Density between solid contours: $7.3 \times 10^5 \mathrm{cm}^{-3}$.

described for single columns in section 3.2.2. At $t = 3$ seconds, low-density arms and a 'bridge' between the vortices have formed, characteristic of vortices barely stable to the pairing instability. Measurements of the scaled separation $d_{12}/2\rho_v$ show that it has decreased from 2.24 at $t = 0$ to 1.60 at $t = 3$ seconds. Merger was observed to take place ~ 3.15 seconds after injection.

The observed rates of column expansion for the stable 2 column case are consistent with those measured for one column. Since column expansion was found to increase very strongly with r_1, it is to be expected that the stable two-vortex lifetime curve will show the leveling off it does beyond immediate merger. This is because columns further apart will have a greater initial separation, inhibiting merger, but the d_{12} increase will be more than offset by the faster radius expansion rates.

4.5.3 Boundary Effects

Merger From Point Vortex Motions

The presence of a cylindrical boundary in the experiment can greatly decrease the lifetime of the two-vortex state. For example, vortices injected near Havelock unstable equilibria may move on trajectories which bring the two closer together. The vortices essentially drift into each other.

The phase space plots of $H(r_1, \theta_2 - \theta_1, P_\theta)$ discussed in section 4.4.4 allow one to visualize an example of this. Figure 4.8 showed the energy contour map for point vortices injected at $r_1 = r_2 = 0.758$. After injection at $\theta_1 = \theta_2 + \pi$, the vortices will move along the energy contour passing through the X-point. When the vortices drift in θ towards $\theta_2 = \theta_1$, the separation d_{12} between the two will drop from the initial value of $d_{12} = 1.516$ to $d_{12} = .36$. With vortex radii of $\rho_v = 0.12$, one then has $d_{12}/2\rho_v = 1.5$, so one expects that merger will occur; in fact, this was observed

to happen in the data set of figure 4.8. It is thus the Havelock dynamical instability which is responsible for the short (< 1 msec) lifetimes seen at large initial separations in figure 4.9.

Merger From 'Orbital Pumping'

I have found strong, but indirect, evidence that the rate of column expansion is greatly enhanced when the column trajectories move periodically in radius. Evidence for this can be seen in figure 4.9, where τ_{merge} drops by a factor of 70 when the initial placement of two columns is shifted from $r_1 = r_2 = .46$ to $r_1 = r_2 = .5$. As we have seen, single column expansion rates increase strongly with radial displacement, but not enough to account for this factor of 70. Similarly, the dynamical instability can not account for it: the point vortex model predicts that the columns will execute large orbits from their initial points, but in such a way that the minimum d_{12} decreases only 9%, as compared to the $r_1 = r_2 = .46$ initial condition.

Similar evidence can be seen in figure 4.16, which shows τ_{merge} versus scaled separation $d_{12}/2\rho_v$ for two different initial conditions. The circles were measured for columns injected at stable equilibrium positions, i.e. 'equilibrium placement'. The squares were injected with one column on-axis ($r_2 = 0$) and the other at a variable displacement $r_1 = d_{12}$, i.e. 'on-axis placement'. While the circles display a normal equilibrium placement τ_{merge} curve, the on-axis placement vortices never had lifetimes greater than 10 msecs. I have fleshed out the on-axis placement curve from memory (dotted line). The point vortex model again predicts that the separation as the vortices orbit about each other will not change that much, certainly not enough to explain decrease in lifetimes seen.

I believe that the effect causing this is an enhancement of column expansion produced by 'orbital pumping'. As was discussed in section 3.2.2, the cause of single

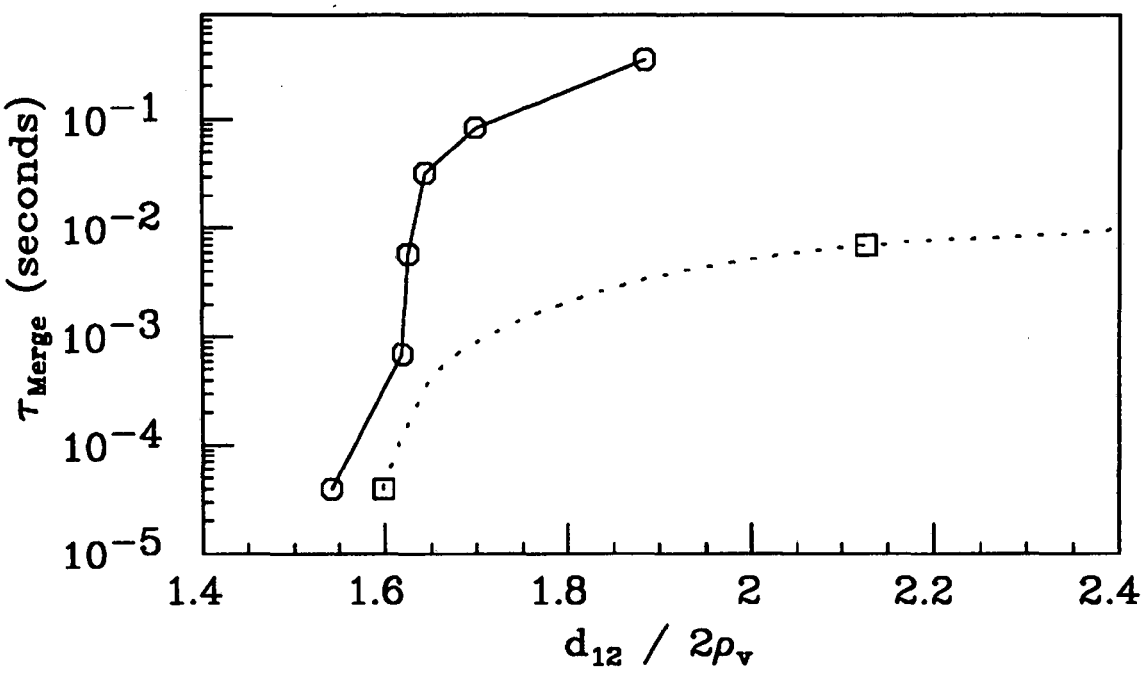

Figure 4.16: τ_{merge} vs. minimum scaled separation for vortices injected with $r_1 = r_2$ (o) and $r_2 = 0$ (□).

column expansion is believed to be 'rotational pumping' [11]. Rotational pumping occurs with single off-axis columns because as an electron rotates about the column center due to the self-field, the electrons confinement length will change due to the curved shape of the electrostatic confinement fields. This oscillatory change by an amount ΔL once each $\tau_{rotation}$ will result in heating [2]. The heating can only come from the electrostatic energy $\mathcal{H}_\phi$ of the column, which implies that column expansion should occur.

Radius expansion rates from rotational pumping have been calculated by Crooks [11] to go as $(\Delta L/L_p)^2$. An examination of the dependence of L_p on displacement (see figure 3.4) reveals that a column orbiting from $r_2 = 0$ to $r_2 \sim .5$ will have a pumping of its length given by $\Delta L/L_p \approx .013$. This is roughly a factor of 5 increase in $\Delta L/L_p$ compared to that experienced by a stationary column at $r_2 \sim .25$, which according to theory would increase its expansion rate by a factor of 25. This is the sort of increase in expansion rate which is required to explain

the experimental data. While my evidence for orbital pumping to date is indirect, I find the mechanism for it plausible, and believe it will shortly be proved to have an important effect on 2 vortex lifetimes.

Chapter 5

Asymmetric Double Vortex Studies

5.1 Introduction and Overview

In this chapter I describe experiments on two vortices which have different radii but equal central vorticity. The focus here is more on merger and less on equilibria, in large part because no discrepancies from point vortex theory were noted in these experiments on vortices asymmetric in circulation but symmetric in $T_{||}$. The object was not just to study the dynamics of two interacting asymmetric vortices, but also to obtain predictions about the more complicated system of many interacting vortices.

Experiments and simulations have long established that vortices can emerge from both laminar flows [30] and structureless initial conditions [46]. When sufficient time has passed, an undriven 2D turbulent state can therefore evolve to a conceptually much simpler system of many vortices (of both sign), sufficiently well-separated that merger takes place relatively infrequently. The subsequent evolution of this system will then be dominated by the dynamics of the vortices, which includes merger of like-signed vortices and mutual advection.

Recently, studies of this many-vortex state, using direct numerical simulations of the Euler equations, have supported the hypothesis that the essential fea-

tures of the evolution are contained in a simple 'punctuated Hamiltonian' model [8, 3]. In the punctuated Hamiltonian model, the motions of the spatially extended vortices are calculated by the point vortex approximation, and simple rules are used to replace two vortices with one bigger one when they occasionally approach close enough to merge. These models have resulted in predictions for timescales which are in qualitative agreement with the results of simulations [8, 3, 69]. However, the assumptions of the punctuated Hamiltonian model have not previously been supported by detailed studies (experimental or theoretical) of the validity of the point vortex approximation, or of the details of the asymmetric merger process. On the contrary, one recent paper [21] on this subject, where contour dynamics simulations of top hat (i.e. uniform vorticity) profile vortices were used to study the merger of vortices asymmetric in radius, found that the conditions for and the products of merger are very different than has been assumed in the punctuated Hamiltonian models.

In Chapter 4, I showed that the point vortex approximation results in accurate predictions for the equilibrium positions, oscillation frequencies, and instability rates of two spatially extended identical vortices. This result provides some support for the vortex motion hypothesis of the punctuated Hamiltonian model. In this chapter, I present the results of experiments on merger, where I have varied the radius of the vortices and studied both the time to merger and the final state produced by merger. I find that merger, once started, quickly results in a central core surrounded by a diffuse halo. The peak vorticity of the core is observed to be roughly the same as that of the merging vortices. The fraction of the total circulation entrained into the central core varies from 70% to 90% as the initial vortex radii are varied from 1:1 to 2:1. This fraction, as well as the time required before merger (τ_{merge}), depends on the initial placement of the two vortices. I also find that the self-energy of the central core is roughly equal to the sum of the self-energies of the merging vortices. These

results are in reasonable agreement with the premises of the punctuated Hamiltonian models, but disagree with the contour dynamics results in that partial merger events (where two cores persist after merger) are not observed.

The chapter is organized as follows. I first show density plots of two asymmetric vortices undergoing rapid merger, and a radial profile of the final merged state. Section 5.3 presents results on merger time versus initial position. I display merger curves (i.e. τ_{merge} vs. separation d_{12}) for vortices with different relative radii. Very long lifetimes ($> 10^4$ orbit periods) can be achieved for well-separated vortices injected at stable equilibrium positions, but as was seen in the symmetric case (section 4.5.3), the placement of the initial condition impacts the time required to merge.

The evidence that merger events are complete and not partial is discussed in section 5.4. In section 5.5 I quantify the evolution of the two-vortex system during merger. Since the vortex profile after a merger is monotonic but does not have a sharp edge, it is necessary to determine a cutoff length for the purpose of calculating the quantities of interest for the merged core. In section 5.5.1 I present a simple algorithm for establishing this cutoff, and present experimental evidence that this algorithm yields radii that are physically reasonable. Then, in section 5.5.2 I show how the central vorticity, self-energy and bound circulation of the vortices change after a merger.

5.2 Example of Asymmetric Vortex Merger

In figures 5.1 and 5.2 I show an example of two vortices, asymmetric in radius but with the same peak vorticity ζ_{peak}, merging. The initial placement is 'vortex on-axis', and the ratio of radii is 2:1. The final plot has dots which indicate where the data has been taken – the plot is then generated by interpolation between the data

grid. I've also indicated on that plot the size of the collimator hole. These plots are quite similar to those of figure 7 of McWilliams [46], which shows a numerical simulation of an asymmetric merger event where, however, the ζ_{peak} of the two vortices is not the same.

After the merger had taken place, I allowed the system to evolve for 5 msec, then damped the l=1 wave for 15 msec to move the merged core on-axis. (I have established that this movement does not appreciably affect the radial profile.) The resultant radial profile of $n(r)$ versus radial position is shown in figure 5.3. This is a typical example of the profile resulting from an asymmetric merger event.

Several features should be noted about these merger pictures. First, the smaller vortex is strained out into a filament whose observed width is about the same as that of the collimator hole. This observed filament width is the result of convolution, by the hole, of a substantially narrower filament. Although the actual structure of the filament is not resolved, when deconvolution is done on the 2D plots, it has been found that the data is consistent with filaments being as narrow as a delta function. It is clear that the effects of the collimator hole size and of the density of data points have to be taken into account when interpreting the 2D plots.

Second, it is apparent that the smaller vortex has been pretty well dissipated (i.e. merged) by 60 μsecs. The largest vorticities measured in the filamentary structure at this point are about 12% of the initial ζ_{peak}. There is no indication of a long-lived secondary core in the subsequent evolution, either in the later-time radial profiles (which would reveal the presence of a large ζ_{peak} core) or in the observed sector probe signals. This result is in disagreement with the prediction of Dritschel and Waugh [21] from contour dynamics simulations of isolated top hat vortices. For the initial conditions of figure 5.1, they found that a secondary core with a radius 65% that of the smaller vortex's radius persisted after merger. I will return to this

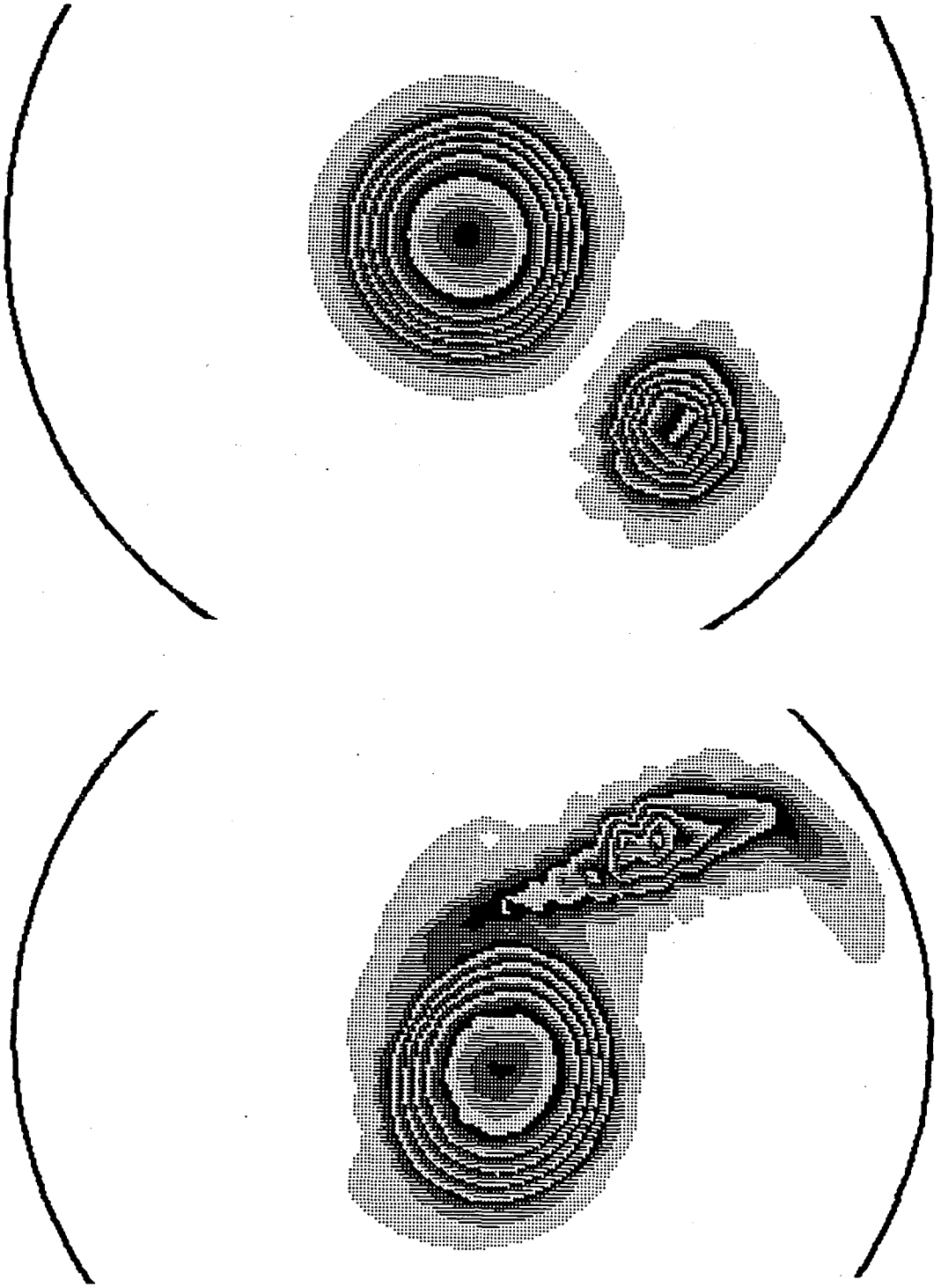

Figure 5.1: Density plots of two asymmetric vortices merging. Times: t = 0 and 15 μsecs. Density between solid contours: $4.9 \times 10^5 \text{cm}^{-3}$.

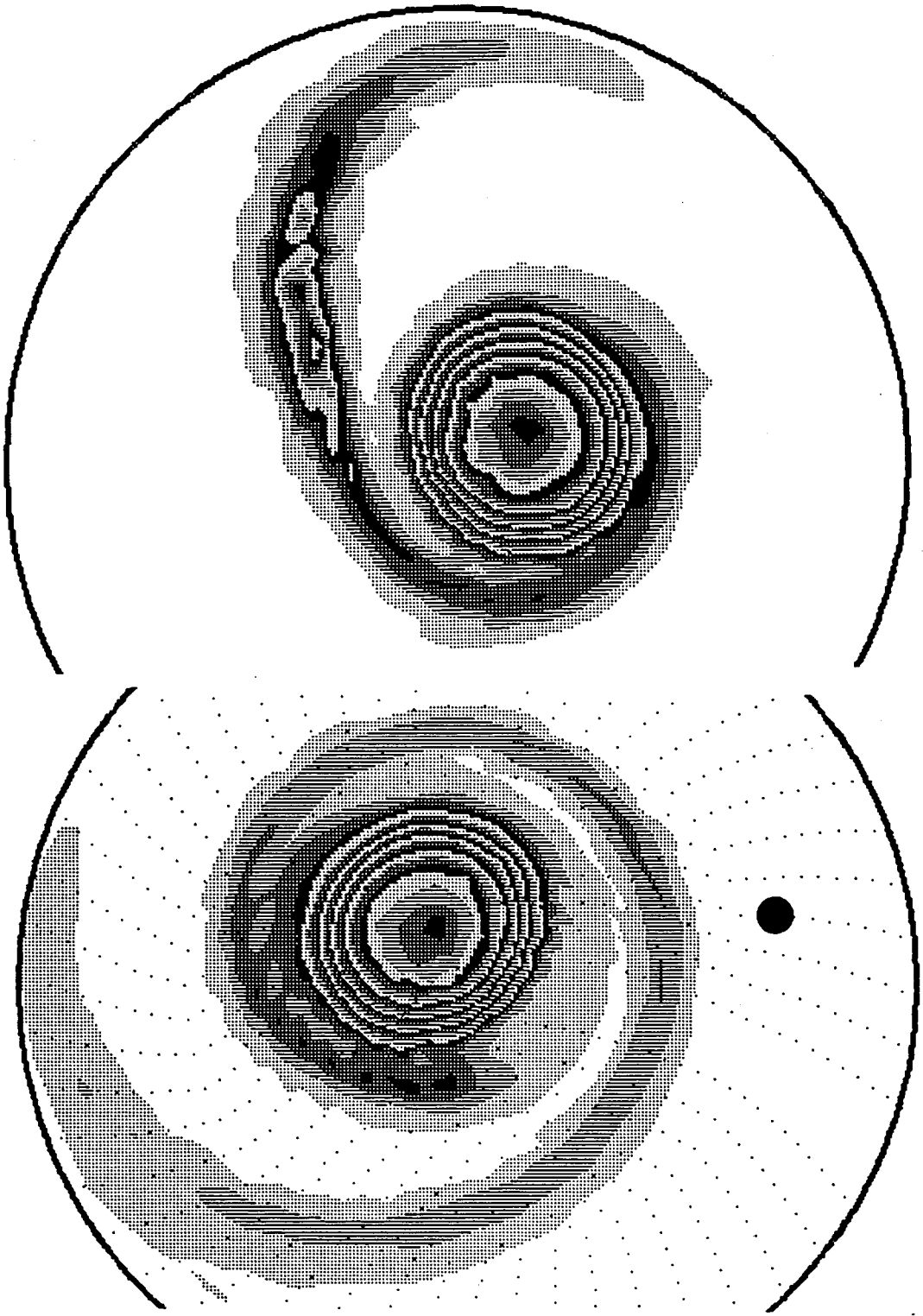

Figure 5.2: Asymmetric merger at t = 30 and 60 μsecs. The positions where the data has been taken, and the collimator hole size, are indicated on the t = 60 μsecs plot.

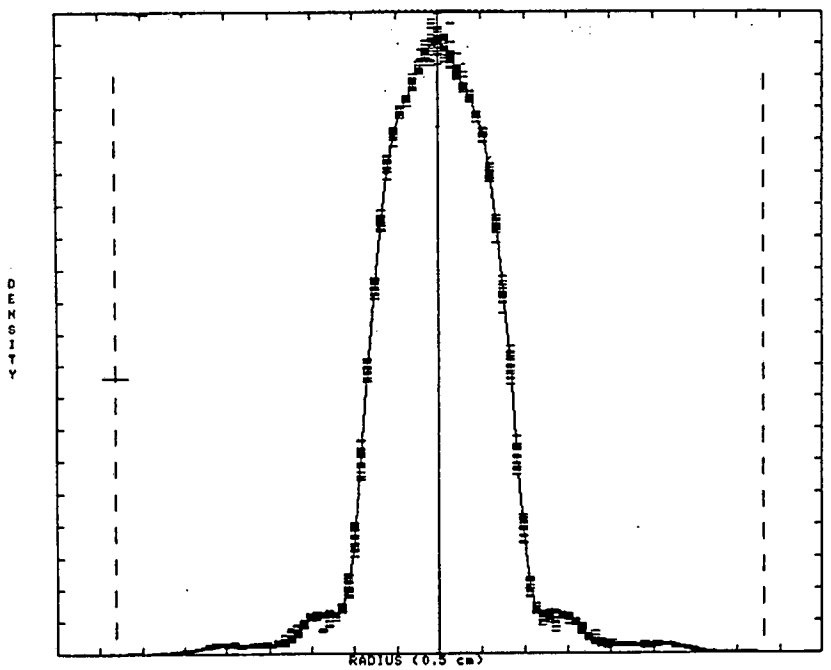

Figure 5.3: Non-phase-locked radial profile taken 20 msecs after merger shown in figures 5.1 and 5.2. 21 measurements of density were taken at each radial position.

question of the completeness of merger again in section 5.4.

Finally, note that the final profile (figure 5.3) consists of a core surrounded by a low-density halo. If this profile were surrounded by many other vortices, the halo would be stripped away by vortex interactions, while the core would remain intact unless merger takes place. To answer such questions as how much circulation is bound in a merged profile, it is necessary to have an algorithm for defining what constitutes the core. This problem is addressed in section 5.5.1.

5.3 Merger Times for Asymmetric Vortices

Merger curves (τ_{merge} vs. separation d_{12}) have been measured for five different initial conditions. The initial conditions are tabulated in table 5.1, where the corresponding symbol is also indicated. As was seen in the symmetric merger case (section 4.5.3), the initial placement of the vortices has an important impact

ρ_2/ρ_1	ρ_1	initial placement	symbol
1.0	0.147	equilibrium	□
0.92	0.173	equilibrium	x
0.65	0.228	equilibrium	+
0.85	0.176	vortex on-axis	▽
0.67	0.181	vortex on-axis	△

Table 5.1: Initial conditions for merger curve data.

on τ_{merge}. Vortices injected in stable equilibrium positions have significantly longer lifetimes than those injected with the same separation, but with one vortex on-axis. Two of the initial conditions have the same radius asymmetry of $\rho_2/\rho_1 \sim .66$, but differ in the initial placement, which permits the effect of the placement to be isolated. As previously discussed, the decrease in lifetime is conjectured to be from orbital pumping.

In figure 5.4 I plot the measured τ_{merge} versus $d_{12}/(\rho_1 + \rho_2)$. These merger curves clearly do not overlay each other. The great difference in lifetime caused by the initial placement can easily be seen here - for the same scaled separation of $\sim 2.4(\rho_1 + \rho_2)$, vortices with $\rho_2/\rho_1 \sim .66$ injected into equilibrium positions had a lifetime 350 times greater than vortices injected with one vortex on-axis.

In two papers on the punctuated Hamiltonian model, the critical separation d_c for immediate merger used was $d_c = 1.7(\rho_1 + \rho_2)$ by Benzi *et. al.* [3] and $d_c = 1.65(\rho_1 + \rho_2)$ by Carnevale *et. al.* [8]. These criteria for merger are indicated (dashes and dots) on figure 5.4. A more recent paper by Weiss and McWilliams [69] has used an elliptical moment model to determine the critical separation d_c for merger, and found a good fit to the results of the numerical integrations with

$$\frac{d_c}{\rho_1 + \rho_2} = 1.6\left(1 + \frac{\rho_1 - \rho_2}{\rho_1 + \rho_2}\right) . \tag{5.1}$$

I can use my data to compare these competing predictions for d_c directly.

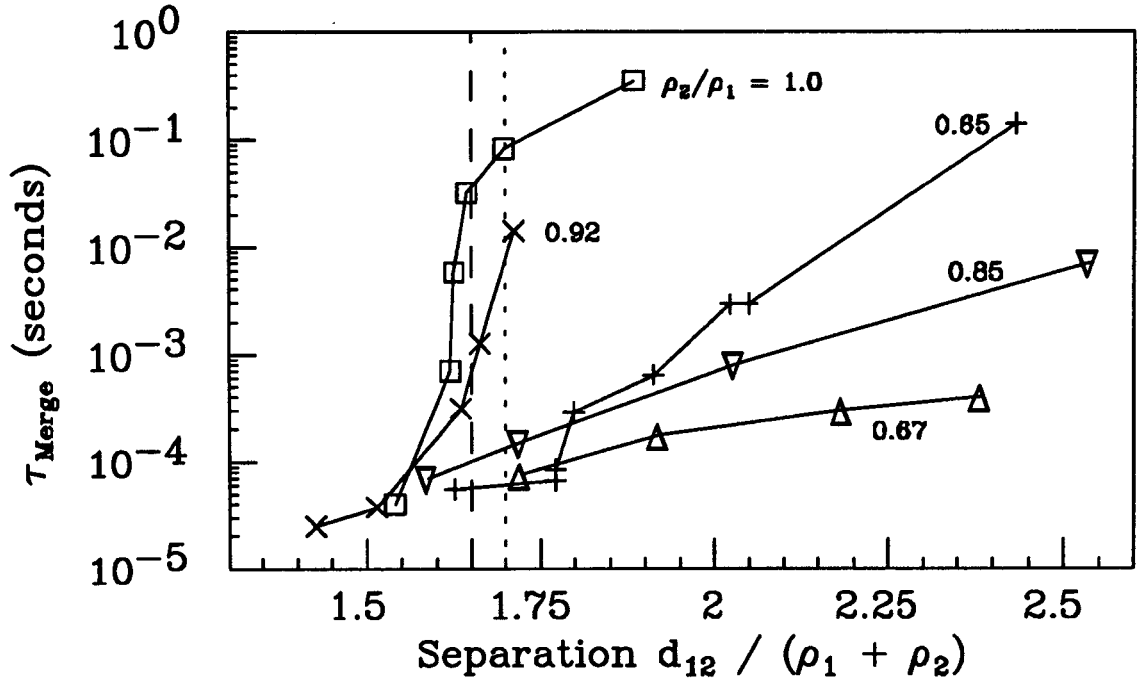

Figure 5.4: Merger curves, where the separation d_{12} has been normalized to $(\rho_1 + \rho_2)$. The radius ratio ρ_2/ρ_1 is indicated.

Experimentally, I consider the critical distance to be that which results in merger in about one orbit. In figure 5.5 I have plotted the measured separations, as a function of relative radii, which bracket the critical distance. The smaller distances (at each ρ_2/ρ_1 value) resulted in merger in less than one orbit period, while the larger distances resulted in at least one orbit before merger. The merger predictions of Weiss and McWilliams, Carnevale *et. al.* and Benzi *et. al.* are shown, and the data shows better agreement with Weiss and McWilliams' prediction than with the others.

5.4 Completeness Of Merger

The question of whether there are significant differences between merger of symmetric vortices and merger of vortices asymmetric in radius is an important and controversial one. Dritschel and Waugh [21] recently used contour dynamics

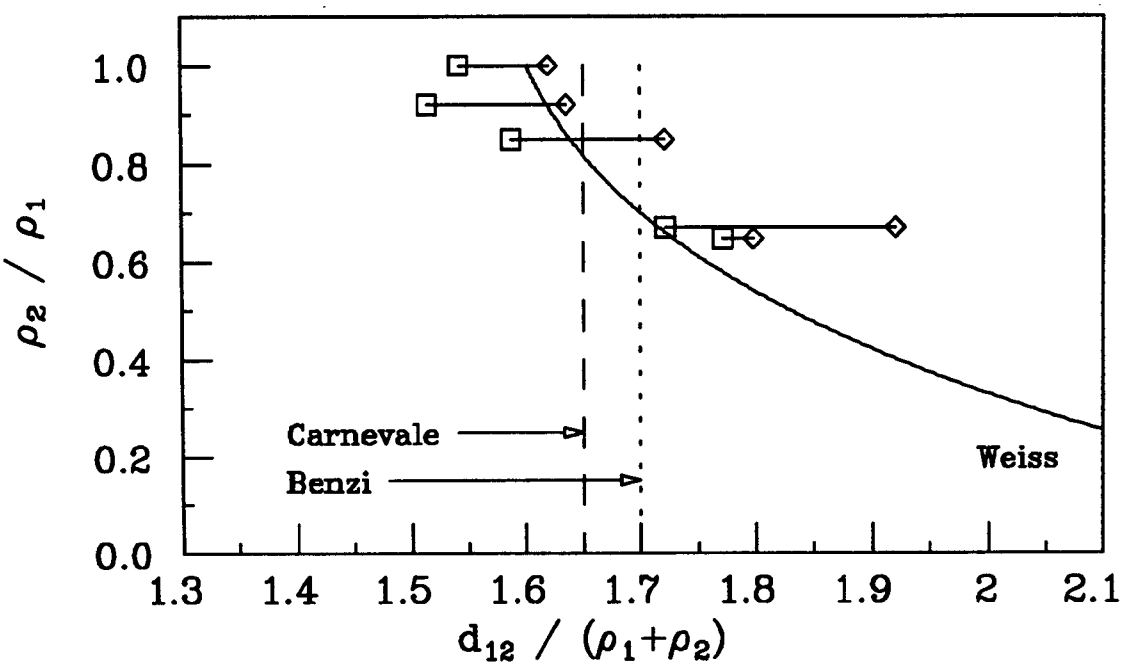

Figure 5.5: Separations giving merger in less than an orbit period (□), and in more than an orbit period (◇), versus relative radii ρ_2/ρ_1. The merger criteria used by Weiss and McWilliams (line), Benzi *et. al.* (dots) and Carnevale *et. al.* (dashes) are also shown.

simulations of two isolated top hat profile vortices to investigate this, and found that many unexpected interactions were seen. The picture of asymmetric merger expected from the symmetric studies was that either two vortices would stably orbit about each other (elastic interaction) or merge, forming a merged core larger than either vortex (complete merger). Dritschel and Waugh found that for some separations, partial merger took place where vorticity would be exchanged, but both vortices survive and elastically interact after the partial merger event. In addition, they also found that there could be both partial and complete straining out events, where the vorticity ejected by the smaller vortex does not become associated with the larger vortex. They thus found that smaller vortices were often produced by asymmetric merger, and concluded that it "is therefore inappropriate to talk of the 'merger' of unequal vortices, since over a large range of initial conditions the two vortices do not

join together to form a single compound vortex."

The electron vortex experiments obviously have many differences from the ideal theoretical system investigated by Dritschel and Waugh. To enumerate some of these:

1. The electron vortices are not isolated, but are contained in a circular boundary and thus interact with image forces.

2. The vortices do not have top hat profiles, but rather have bell-shaped radial profiles (figure 4.13).

3. The system is bounded (contained) in $\hat{\mathbf{z}}$.

4. The individual electrons execute Larmour orbits about their guiding center.

Because of these differences, little correspondence is seen between the experiments and the predictions of Dritschel and Waugh. In particular, I have found little evidence for partial merger events resulting in two altered and stable vortices. Additionally, while I do find that the structure of the merged vortex core depends on the initial separation, I have always found merger to result in the merged core being larger than the larger vortex, and hence do not observe 'straining out' events. Merger of asymmetric vortices thus is not observed to be significantly different from merger of symmetric vortices.

Since the EV apparatus does not have a camera diagnostic, our knowledge of merger will be improved when merger is studied on the new Cam-V machine. The evidence from EV, however, appears fairly conclusive that our asymmetric vortex merger is a quick and complete process. The density plots are able to follow merger for several orbit periods before they become too noisy to be useful. These plots always show merging vortices to join, and any filaments to rapidly become strained and reduced in ζ_{peak}. Occasionally, small coherent patches of vorticity become ejected: an

example of this for symmetric merger can be seen in figure 4.10, where the filaments show maxima. These maxima, however, are observed not to persist as the filaments wind about the merged core.

If persistent vortex cores were common stable structures of the post-merger system, I would expect to detect them on the non-phase-locked radial profiles, where they would show up as higher values of density seen intermittently in the halo. Such anomalously higher values have not been seen, either in the many profiles taken to characterize the final state of merger (i.e. after $\sim$ 20 msecs), or profiles taken just after merger specifically to look for this effect.

Finally, I would expect the presence of persistent cores after a partial merger to show up on the sector probe signals. What is actually seen on the signals is the complicated but unevolving waveform of the two asymmetric vortices orbiting about each other, followed by a single l=1 frequency after merger. The transition between the orbit waveform and the l=1 waveform occurs in about one orbit period, and the waveform after merger only rarely shows frequencies in addition to the l=1 frequency.

In figure 5.6 I have replotted my asymmetric merger data, along with the predictions of Dritschel and Waugh. The symbols mark my data, with the squares indicating (complete) merger with one orbit period, and the diamonds indicating merger at time greater than one period. The curves are from figure 5 of [21], transformed to my variables, showing the predicted region of non-merger events. One can see that many of my data points are in regions where partial merger or partial straining out is predicted, yet only complete mergers were observed.

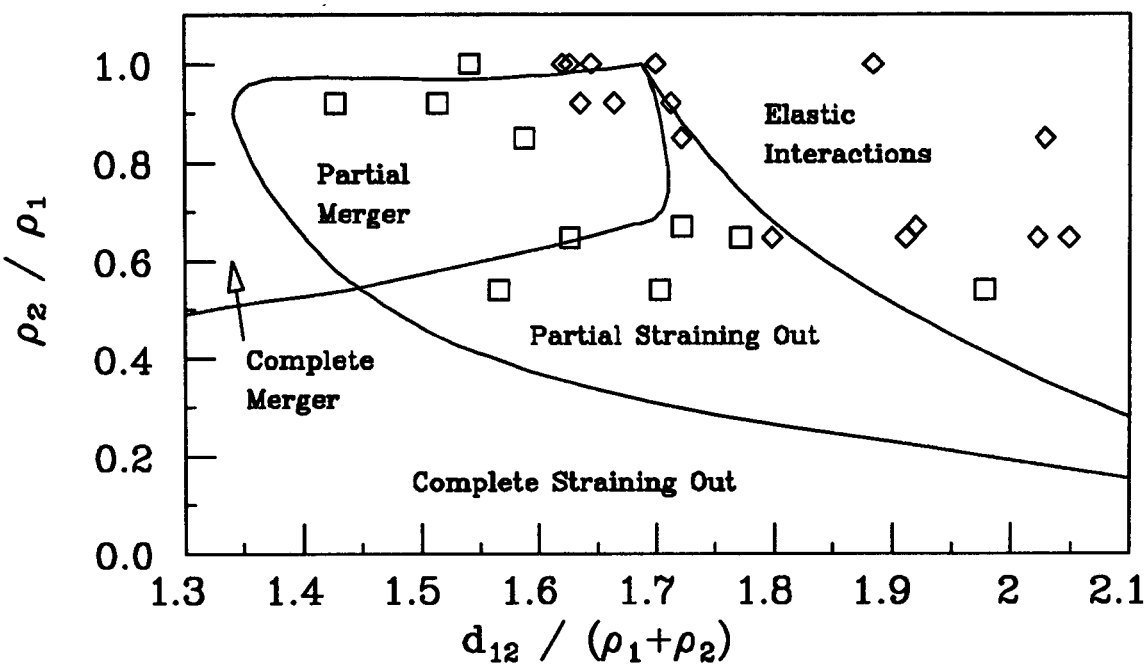

Figure 5.6: Merger curve data plotted with the predictions of Dritschel and Waugh for top hat isolated vortices from contour dynamics simulations. Squares (□) indicate complete merger observed within one orbit period, and diamonds (◇) lifetimes greater than this.

5.5 System Evolution During Merger

5.5.1 Definition of Vortex Radius

The density plots of merger that I have taken, of which figures 5.1 and 5.2 are an example, reveal that the detailed evolution during merger sensitively depends on the initial conditions, but always results in a central core surrounded by filaments winding about it. This distribution then axisymmetrizes, on a timescale of tens of rotations (msecs), into a core surrounded by a halo. Figure 5.3 is an example of a typical merged profile.

In order to quantify the evolution of the system during merger, for each initial condition detailed in table 5.1 above I have taken radial profiles of the vortices both before and $\sim$ 20 msecs after the merger. (This particular time after merger was selected because the noise then was sufficiently low to allow a good average of the

merged profile to be taken with 20 shots at each radial position.) This approach to studying the merged state can be contrasted with the method used by Waugh [68], who quantified the efficiency of symmetric merger by integrating contour dynamics simulations of top hat profile merger forward in time until the filaments began to 'pinch off' the central vortex. He then considered the filaments to have been ejected from the core, and removed them. I feel this procedure adds an arbitrariness to the measurement, since the filaments can be seen to wrap tighter around the core as time progresses, and can reattach.

The final state profile depends on the sizes and separations of the two vortices. In figure 5.7 I show the radial profiles resulting from merger with $\rho_2/\rho_1 = .67$ and three different initial separations (with one vortex on-axis). The initial radial profile of the larger vortex before merger is also shown by the dotted line. One can readily see the effect of the initial separation: the smaller d_{12} is, the more compact the merged profile.

It is useful to conceptually divide the profiles into a 'core' and a lower density 'halo'. The distinction between the two is that fluid in the core is bound, while the fluid in the halo is sufficiently far from the core that it may be advected away by subsequent near encounters with other vortices. Merger will result, therefore, in some initially bound vorticity being ejected into the background. To quantify this process, it is necessary to define an algorithm for determining the cut-off point (r_{cut}) between the core and halo. The profile resulting from $D_{12} = 2.67$ in figure 5.7 is a case where one could perhaps determine a cut-off point by inspection at about 1 cm. In general, however, the merged profiles do not have obvious cut-off points, and inspection for minima is therefore an unsatisfactory prescription. However, a self-consistent algorithm has been developed for determining r_{cut}.

The algorithm uses the idea that the onset of the pairing instability can be

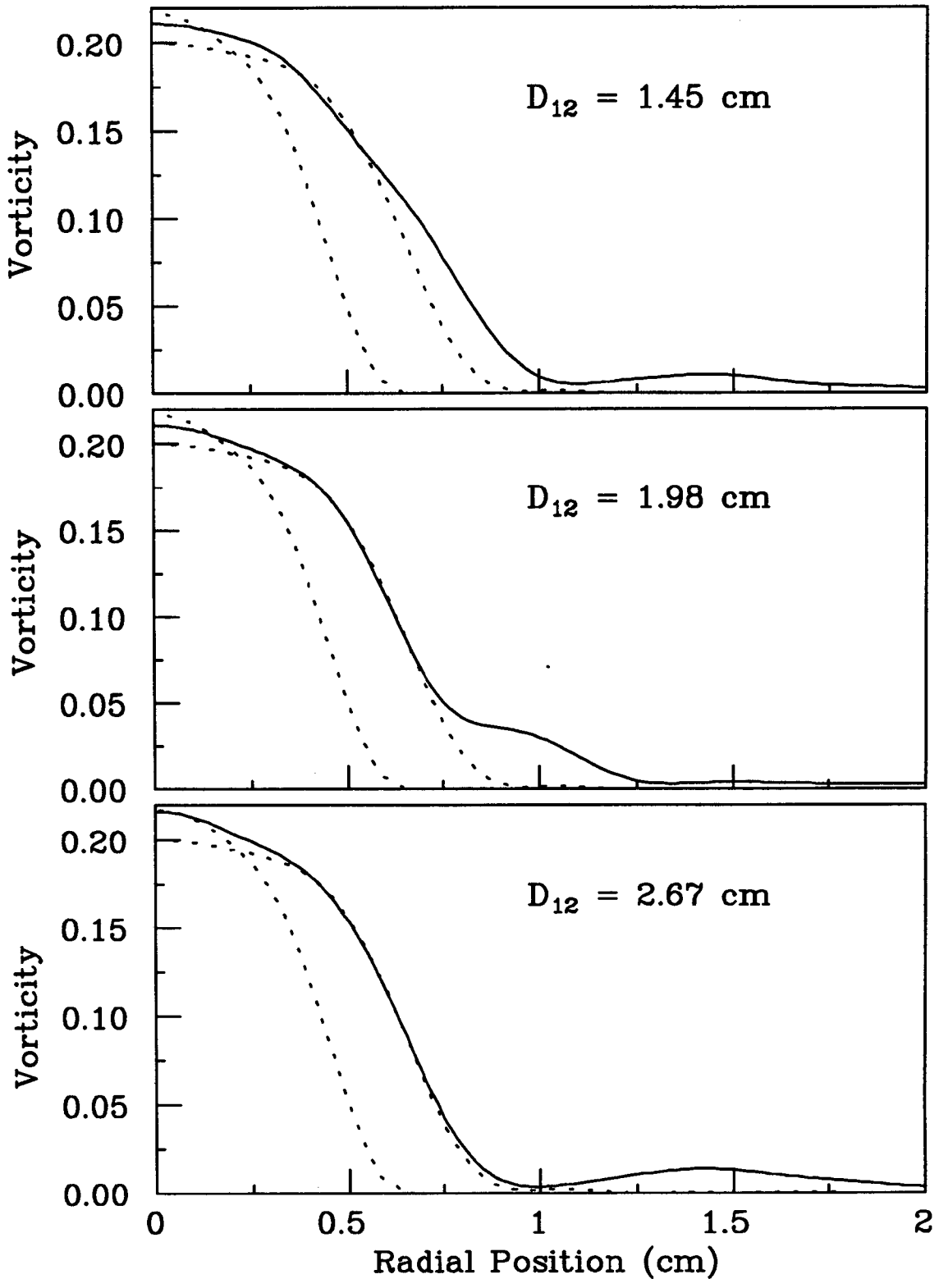

Figure 2.6: Radial profiles after merger (lines), and for the large and small vortices before merger (dots). The relative radii were $\rho_2/\rho_1 = 0.67$ and the initial separation D_{12} is indicated.

used to define the dynamically important regions of vorticity. In section 4.5.1, the vortex radius R_v was defined by

$$R_v \equiv \frac{3}{2}\frac{1}{N_L}\int_0^{r_{cut}} r'\, dA\, n(r,\theta) \ , \tag{5.2}$$

where r_{cut} was defined to be (for sharp profiles) the point where the density went to zero. With this definition, symmetric vortices were observed to be immediately unstable to the pairing instability when the separation $d_{12} < 3.2\rho_v$. Given this fact, it seems intuitive that fluid at separations greater than $1.6\rho_v$ from a vortex center should not be considered bound: a second like-signed vortex can pass by at a separation greater than would cause merger, but such that it will be close enough to advect or capture the distant fluid. I therefore define r_{cut} for a haloed profile by

$$r_{cut} \equiv 1.6\rho_v \ . \tag{5.3}$$

Of course, since ρ_v depends on r_{cut} through equation 5.2, equations 5.2 and 5.3 must be self-consistent.

While this definition is based on considerations of merger with other vortices symmetric in ζ_{peak} and radius, and an evolving many-vortex system will in general have vortices of arbitrary ζ_{peak} and radius, this algorithm is perhaps the most logical one which yields a single value for the vortex radius.

Figure 5.8 shows a determination of ρ_v (and r_{cut}) for a haloed profile which has itself resulted from a prior merger. The solid line is the vorticity profile, and the dashed line is ρ_v from equation 5.2, where the integration is done out to normalized radius $r = r_{cut}$. The dotted line is r/ρ_v, and is a monotonically increasing function which has the value 1.6 at the point where the arrow is. The arrow is thus at r_{cut}. Using this cut-off, we find that this particular profile has about 85% of its vorticity in the core.

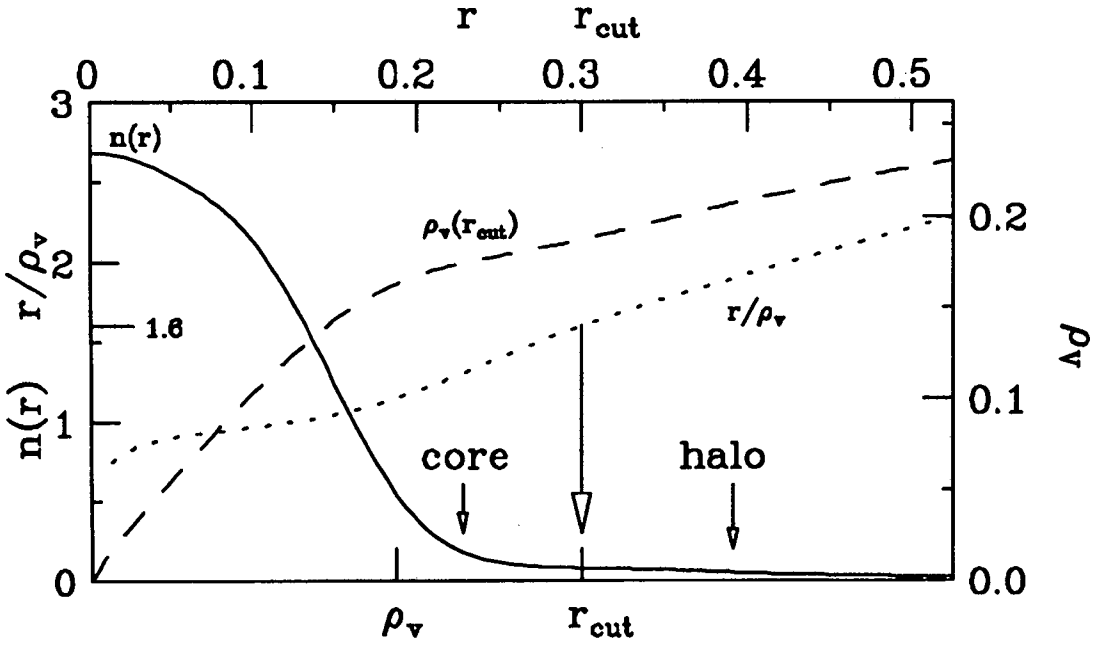

Figure 5.8: Determination of cut-off between core and halo for a haloed vortex profile.

Experimental Test of Vortex Radius Definition

As a test of the vortex radius definition, I have measured the τ_{merge} vs. separation curve resulting from using the haloed vortex with the profile of figure 5.8 as the initial condition. This profile has a radius of $\rho_v = 0.192$ for $r_{cut} = 1.6\rho_v$, and would have a radius of $\rho_v = 0.303$ for $r_{cut} = \infty$. In figure 5.9 I have plotted the measured merger curve with the separations scaled by both of these values. In addition, I've also included the merger data of figure 4.14. It can be seen that the vortex radius algorithm leads to an accurate prediction of when a haloed vortex will be susceptible to the pairing instability, as the merger curve overlays the other data for short τ_{merge} values when the cut-off is imposed.

5.5.2 Measurements of Asymmetric Vortex Merger

In this section I discuss how peak vorticity ζ_{peak}, core circulation Γ, and core electrostatic self-energy H_ϕ are observed to change after a vortex merger event. The

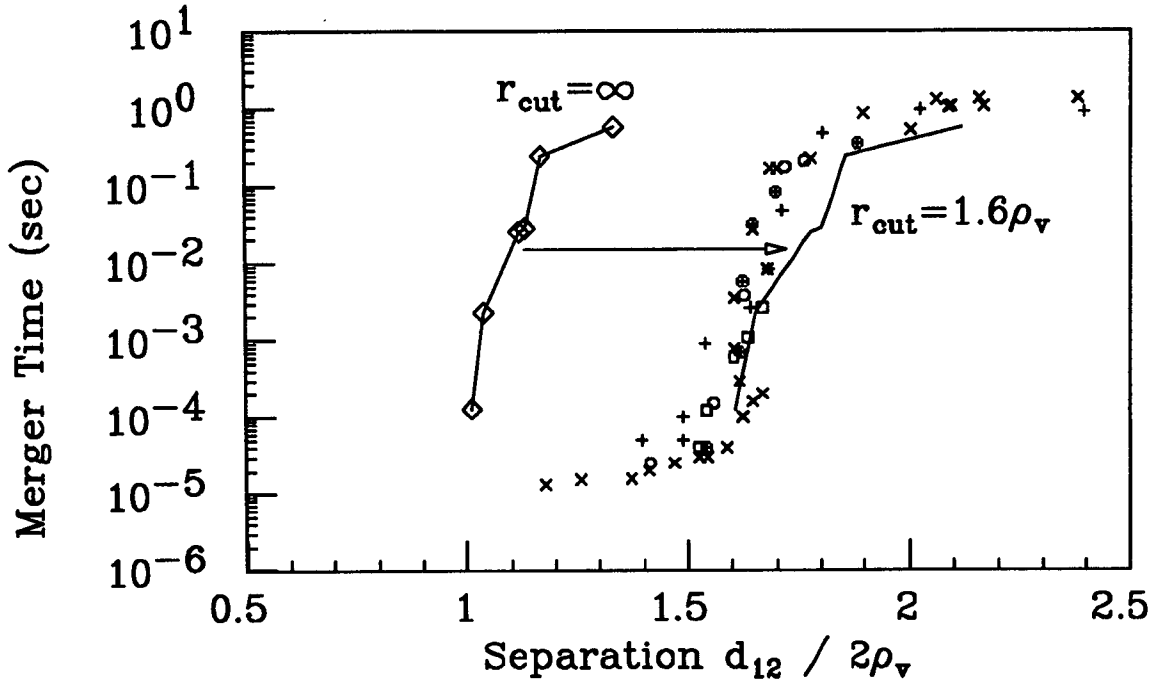

Figure 5.9: Measured merger curve using a haloed profile as the initial condition. The diamonds $\diamond$ are the separations scaled to a vortex radius calculated without using a cut-off. Use of $r_{cut} = 1.6\rho_v$ generates a smaller vortex radius which shifts the merger curve, as indicated by the arrow.

values are quantified from radial profiles measured before and after merger. The data set is the same as discussed in the previous sections on asymmetric merger and tabulated in table 5.1.

Peak Vorticity Measurements

In figure 5.10 I plot the ratio of the measured ζ_{peak} after merger to its value before merger. (Before merger, the two vortices had the same ζ_{peak}.) While there is a fair amount (up to 8%) of scatter, there is no strong evidence that it is anything except measurement noise, as the average of the data yields $0.994 \pm .026$.

A theory prediction for the evolution of ζ_{peak} for asymmetric merging vortices is that ζ_{peak} should be the same after merger. In a study of merger using both numerical and contour dynamics simulations, Melander *et. al.* [47] found that the

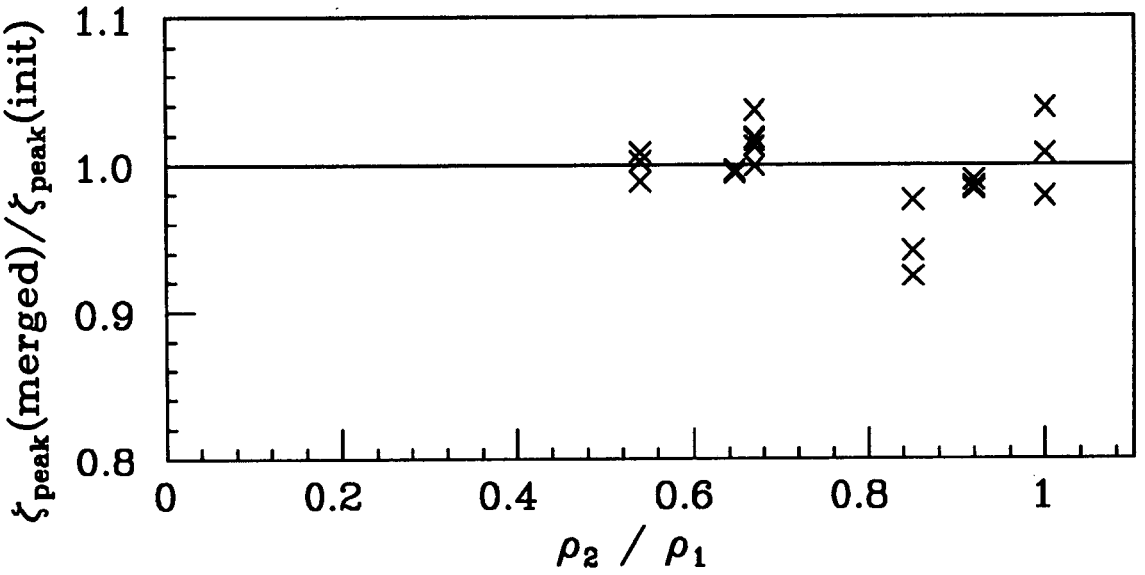

Figure 5.10: Ratio of peak vorticity ζ_{peak}, measured after and before merger, versus ρ_2/ρ_1.

core after symmetric merger has a 'jelly roll' structure with entrained lower vorticity, as can be seen in figure 4.11. However, for asymmetric merger the larger vortex (which they dubbed the 'victor') becomes the central region of the core, which implies that its original ζ_{peak} will be the final ζ_{peak} of the core.

Bound Circulation Measurements

The line density $N_L(r)$ contained with r is given by the total line density N_L of a z-averaged density $n(r,\theta)$ profile is given by

$$N_L(r) \equiv \int 2\pi r' dr'\, n(r') \tag{5.4}$$

and the circulation is $\Gamma(r) \equiv (2\pi ce/B)\, 2N_L(r)$. For the merged core, I designate the circulation within $r = 1.6\rho_v$ by Γ_{core}, and the total circulation by Γ_{total}. Hence, $\Gamma_{halo} = \Gamma_{total} - \Gamma_{core}$.

In figure 5.11 I plot the ratio of the measured circulation after merger with the value before merger. The data marked by (X) indicate $\Gamma_{total}/(\Gamma_1 + \Gamma_2)$, and are thus expected to be equal to 1, since vorticity (charge) is well conserved. The

measurement of Γ_{total} is noisy because the final profile has a significant amount of charge at very low densities. The average of the data is 1.00 ± .02, which suggests that the scatter is random noise.

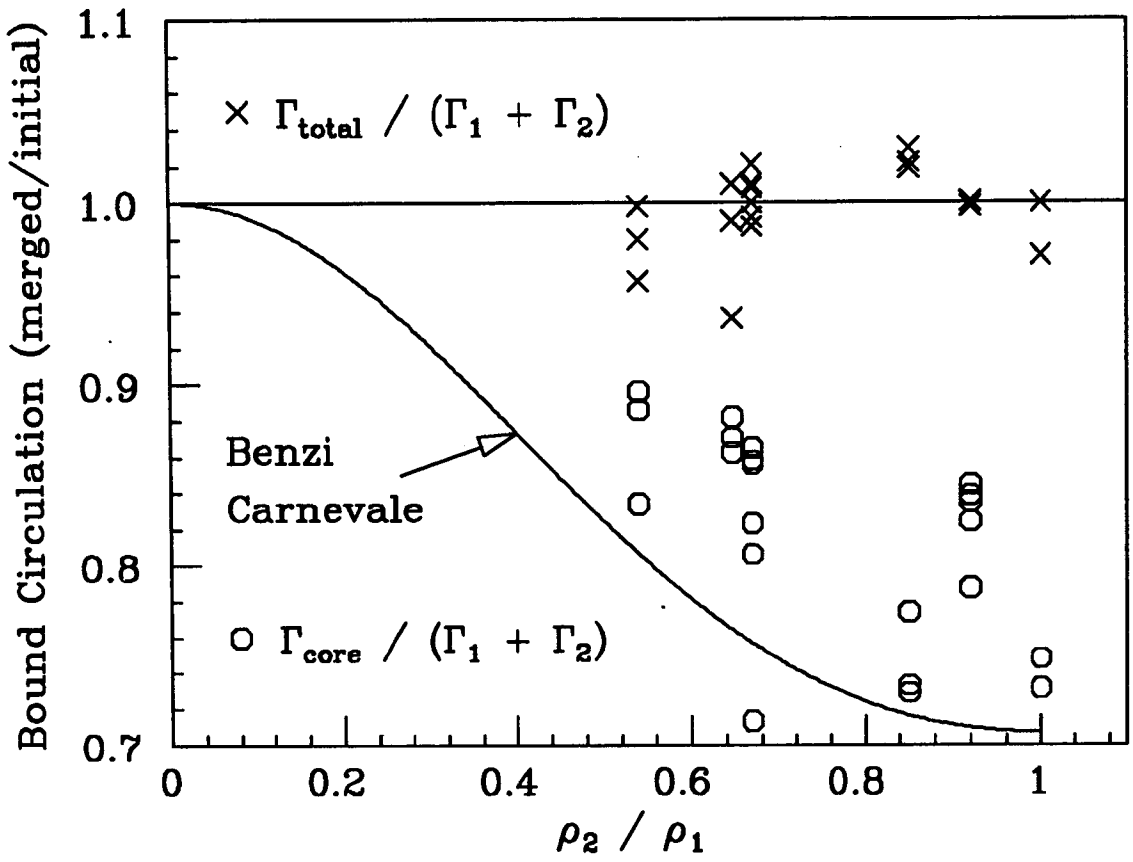

Figure 5.11: Ratio of the circulation measured after and before merger, versus ρ_2/ρ_1. The line is a prediction used by Carnevale *et.al.* and Benzi *et.al.*

The data marked by circles indicates $\Gamma_{core}/(\Gamma_1 + \Gamma_2)$, and thus indicate how much circulation is bound by the core after merger. I find that between 70% and 90% of the circulation remains bound in the core after merger, with some indication that this percentage increases as ρ_2/ρ_1 decreases. The scatter at each ρ_2/ρ_1 value is systematic, depending on the initial separation of the vortices.

These results can be compared with the merger rules used by Carnevale *et. al.* [8] and Benzi *et. al.* [3]. Using arguments involving conservation of kinetic energy

per unit area [8], or involving enstrophy dissipation [3], these authors independently came up with a simple merger rule of

$$\rho_{core}^4 = \rho_1^4 + \rho_2^4 \,. \tag{5.5}$$

This gives that the ratio of circulation bound in the core is given by $\rho_{core}^2/(\rho_1^2+\rho_2^2)$. I have plotted this prediction (solid line) in figure 5.11, as well as a prediction (dashed line) based on a merger rule of

$$\rho_{core}^4 \left[\frac{1}{4} - \ln \rho_{core}\right] \;=\; \rho_1^4 \left[\frac{1}{4} - \ln \rho_1\right] \;+\; \rho_2^4 \left[\frac{1}{4} - \ln \rho_2\right] \,. \tag{5.6}$$

This latter rule takes into account the effect of the wall on the energies of top hat vortices.

While the data shows a large amount of scatter, it is apparent that the measured values are systematically higher than those predicted by the merger rules for top hat vortices. I discuss a possible reason for this discrepancy in the next section.

Self-Energy Measurements

Merger is observed (and predicted) to conserve the total electrostatic energy H_ϕ of the system. Before merger, the energy can be conceptually broken into 'self-energies' of the vortices, $H_{\phi 1}$ and $H_{\phi 2}$, and terms due to their interaction with each other and with the image charges, summing to $H_{\phi int}$. After merger, there are no interaction energy terms between vortices, but we can consider both a total electrostatic energy of the merged system $H_{\phi e}$, and a core self-energy $H_{\phi core}$ where r_{cut} is used to discard the halo.

Carnevale *et.al.* [8], in order to derive their above merger rule (equation 5.5), used as a conserved quantity the self-energy of the merging vortices, i.e. $H_{\phi 1} + H_{\phi 2} = H_{\phi core}$. This is equivalent to asserting that the interaction energy between the merging vortices gets dispersed into the halo.

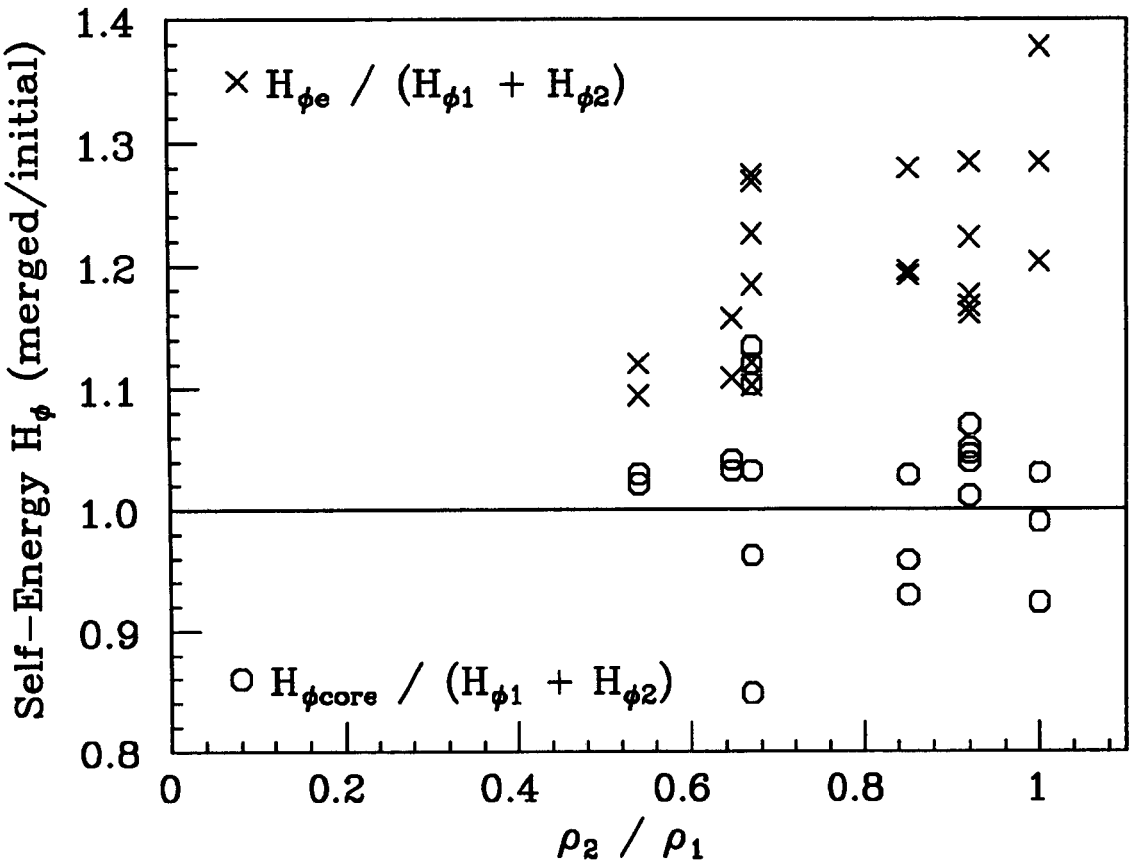

Figure 5.12: Ratio of the electrostatic self-energy H_ϕ measured after and before merger, versus ρ_2/ρ_1.

I have tested Carnevale's conjecture with my data, by calculating the self energies of the merging vortices, and of the merged profile with and without using r_{cut} to discard the halo. The self-energies are calculated as described in section 2.4.2: the 3D potential $\phi(r,\theta,z)$ and density $n(r,\theta,z)$ distributions were solved for using the measured on-axis axisymmetric density profiles, and the energies were then given by eq 2.6.

In figure 5.12 I plot the quantities $H_{\phi\epsilon}/(H_{\phi 1}+H_{\phi 2})$ and $H_{\phi core\epsilon}/(H_{\phi 1}+H_{\phi 2})$. As in the bound circulation data, the scatter at each ρ_2/ρ_1 value is systematic. As expected, the initial interaction energy is missing: from all the points, $H_{\phi\epsilon}/(H_{\phi 1}+H_{\phi 2}) = 1.20 \pm .07$. I find, however, that the mean of the $H_{\phi core\epsilon}/(H_{\phi 1}+H_{\phi 2})$ points is

$1.02 \pm .07$. While the measurements show a great deal of scatter, and are of course dependent on my particular definition for the core and halo, this result seems to indicate that Carnevale's conjecture is not an unreasonable one.

Returning now to the question of the amount of circulation bound in the halo, I note that merger rules 5.5 and 5.6 are derived from the principle that the self-energy of top hat vortices is conserved during merger. Since self-energy is found experimentally to be roughly conserved, this suggests that the discrepancy seen in figure 5.11, between the measurements and predictions based on these merger rules, might be simply due to the non-top hat profile of the electron vortices.

Appendix A

Heating from Cascading

A.1 Introduction

In this appendix I present the results of studies on the heating done by 'cascading'. The objective was to understand the heating done as a function of the cut gate rise time (τ_{cut}), and of the length of the region the column has been cascaded into.

Cascading has been described previously in section 2.5.4, and a schematic of the process is shown there in figure 2.4. In order to put two (or more) columns together when only one filament source is available, it is necessary to lower a cut gate between them and let them stream into a common containment region. Unless the two are at the same θ-position (which will result in only one column after cascading), they freely expand into the vacuum beyond the cut gate. This free expansion causes heating of the parallel temperature, and can additionally cause $r-\theta$ density transport. This heating is acceptable for vortex interaction experiments as long as the same heating occurs for all the columns, since the fluid analogy breaks down when the electron columns have different parallel temperatures.

Figure A.1 shows the experimental setup used to study cascading. The column is initially confined in electrode S, with temperatures $T_{\|} \sim T_{\perp} \sim 0.3$ eV, density $n \sim 6.5 \times 10^6 \mathrm{cm}^{-3}$ and length $L_p \sim 5.3$ cm. The cut gate L4 initially is at a con-

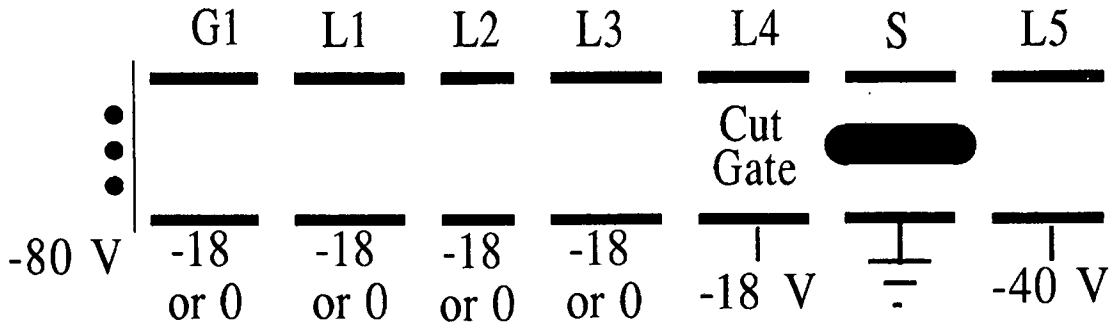

Figure A.1: Experimental setup for study of cascading.

fining potential -18 V, and can be linearly raised to ground with any desired rise time greater than $\sim 0.23\mu$ sec. The electrodes G1 through L4 are either at confining potentials or grounded, while the front grid is at -80 V.

A.2 Variations with Speed of Expansion

This first study examined the effect of the speed of expansion by varying the cut gate rise time (τ_{cut}). L1-L3 were kept at -20V, so the column expands only from S to S-L4. (This is not a cascade because the column does not 'fall' into a grounded ring beyond the cut gate.) After expansion, the column was held until $T_{||}$ and $T_{\perp}$ had equilibrated, and then $T_{\perp eq}$ was measured. Since $T_{\perp}$ is known at the beginning of the equilibriation, knowledge of $T_{\perp eq}$ permits a calculation of $T_{||}$ from equipartition of energy: $T_{||} = 3T_{\perp eq} - 2T_{\perp}$.

There are two extremes of rise time where simple predictions can be made. For τ_{cut} very long compared to τ_{bounce}, the axial bounce adiabatic invariant is good, and the column will adiabatically expand (and cool) such that [37]

$$T'_{||} \approx T_{||}\left(\frac{L_p}{L'_p}\right)^2 . \tag{A.1}$$

At the other extreme, for τ_{cut} very short compared to τ_{bounce} there should be no work

done on or by the electrostatic gates. In this case, energy conservation requires that $\mathcal{H}_{\phi e} + \mathcal{H}_{||} =$ constant, where $\mathcal{H}_{\phi e}$ is the electrostatic potential energy and $\mathcal{H}_{||} \equiv \frac{1}{2}mv_{||}^2 = \frac{1}{2}k_B T_{||}$ is the thermal energy in the parallel direction. Since the initial plasma has about 10 times more energy in $\mathcal{H}_{\phi e}$ than in its initial $\mathcal{H}_{||}$, a great increase in $T_{||}$ will occur as $\mathcal{H}_{\phi e}$ decreases.

In figure A.2 I show the measured total thermal energy ($\frac{3}{2}\mathrm{k}T_{\perp eq}$) of the expanded and equilibriated column, as a function of τ_{cut}. The dashed line marks the estimated τ_{bounce}. The behavior of the curve is as expected: for short τ_{cut} the column has been greatly heated, while for long τ_{cut} the thermal energy reaches a plateau at a low thermal energy consistent with the column adiabatically expanding into S-L4. The bend between heating and cooling occurs for a τ_{cut} near the estimated τ_{bounce} of 0.47 μsec. I note that the shortest τ_{cut} (0.23 μsec) still resulted in some expansion cooling of the column, since energy conservation from the initial state would have resulted in a thermal energy of $\sim$ 2.4 eV/electron.

A.3 Energy Conservation during Free Expansion

This second study sought to verify the idea that beyond the cut gate the column freely expands, and thus $\mathcal{H}_{\phi e}$ and $\mathcal{H}_{||}$ will be conservatively exchanged. The initial conditions were as described above, with the shortest τ_{cut} (0.23 μsec) possible used to minimize density transport. Selected cylinders on the other side of the cut gate (G1-L3) were grounded to provide a progressively longer confinement region for the column to expand into. After expansion, the column was held long enough for the temperatures to equilibriate, and then its thermal energy ($\frac{3}{2}k_B T_{\perp eq}$) was measured with the perpendicular temperature diagnostic. The electrostatic energy ($\mathcal{H}_{\phi e}$) after the expansion was calculated using the 3D density solver previously described in section 2.4.2.

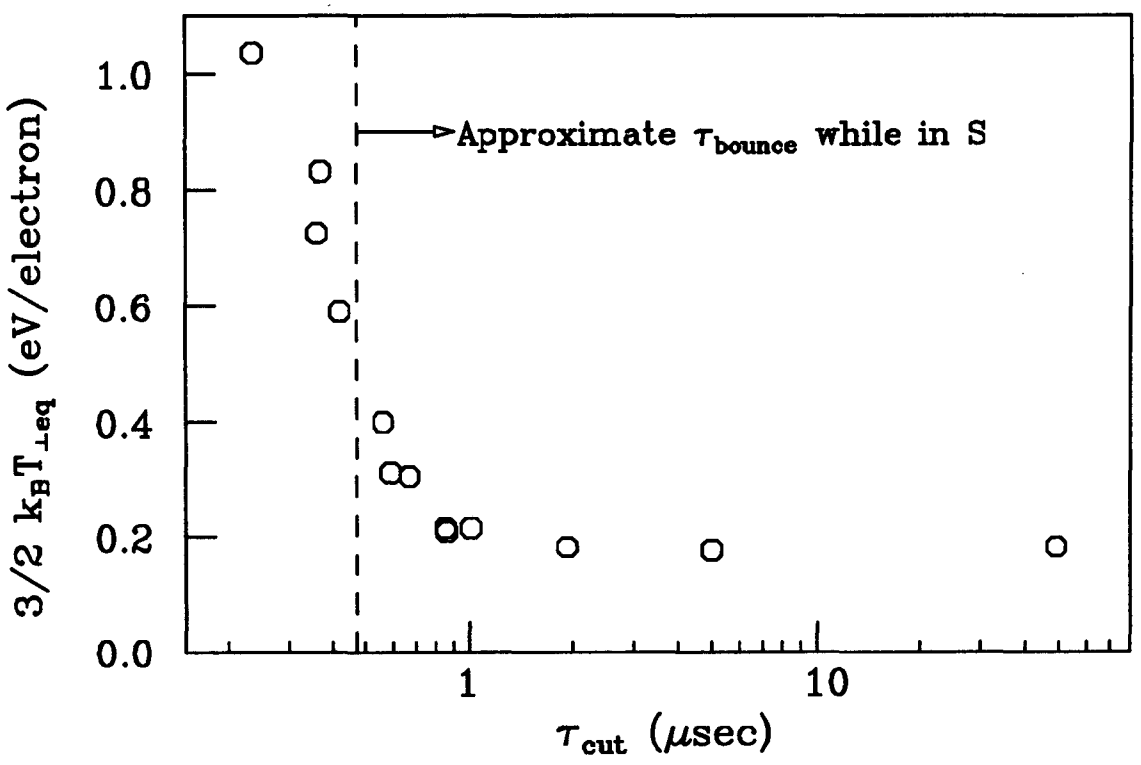

Figure A.2: Thermal energy ($\frac{3}{2}$k$T_{\perp eq}$) of column after expansion from S to S-L4 and equilibriation of T.

Figure A.3 shows the measured electrostatic and thermal energies before and after expansion to different final containment regions. The expansion from S to S-L4 does work on the confinement gates, resulting in some loss of total plasma energy. The final states S-L4 to S-G1 all have roughly the same total energy $\frac{3}{2}k_B T_{\perp eq} + \mathcal{H}_{\phi e}$, however, corroborating the idea that the free expansion into grounded cylinders beyond the cut gate conserves energy.

A.4 Cascade Heating When Two Columns Are Present

When setting up an initial condition for a two-vortex experiment, it is important to adjust the confinement gates such that the same amount of heating is done to both columns. For experiments with symmetric columns the setup is also

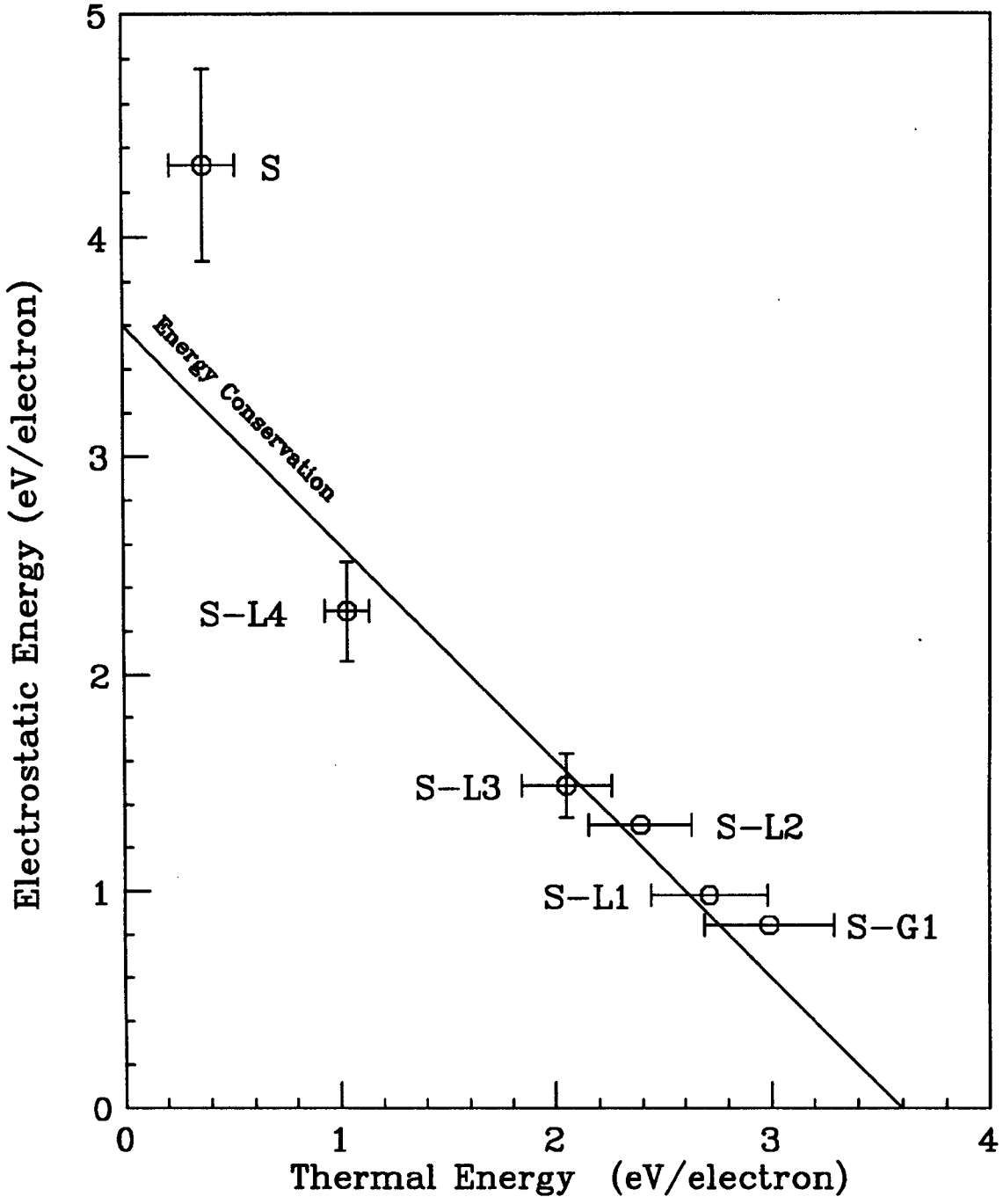

Figure A.3: Thermal energy ($\frac{3}{2}k_B T_{\perp eq}$) and electrostatic energy ($\mathcal{H}_{\phi e}$) of column before and after cascading from containment S to S-X, where X is as indicated. The line through the data has a slope of unity.

usually symmetric, which automatically results in equal heating. For experiments with asymmetric columns, such as those with different radii, it is necessary to adjust the confinement gates because the potential energies of the two columns will be different. The way this is done is by discarding one of the columns and measuring the $l = 1$ frequency offset of the other. By doing this repeatedly for different confinement voltages, these voltages can be adjusted to values which give both columns the same frequency offset and hence the same $T_{||}$.

One problem with this procedure is that during the actual experiment, the columns will be expanding into containment regions with another column present. In this section, I use a simple model to analytically estimate the reduction in the amount of heating done. I find that there is a decrease in heating of at most 11% (where the columns are put together very closely). While this is a significant correction, breaking the symmetry of the two columns line density or position does not break the symmetry of the reductions in heating, and I conclude that the presence of another column during cascading should not result in significant changes to the balancing of the parallel temperatures.

The three stages of the model are as shown in figure A.4. Before cascading, the two columns are in different cylinders, and do not interact with each other (shown in A). They have line densities N_L and radii ρ_v, and are circular and of uniform density. B shows one of the columns having freely expanded into the full containment region, when the second column has been dumped. The line density is now $N_L/2$, and the difference in potential energy between A and B gives the increase in thermal energy resulting from the expansion. C shows both of the columns having been cascaded together. The presence of column 2 increases the potential energy of column 1, thus lowering its increase in thermal energy. It is this difference in heating between B and C that I wish to estimate.

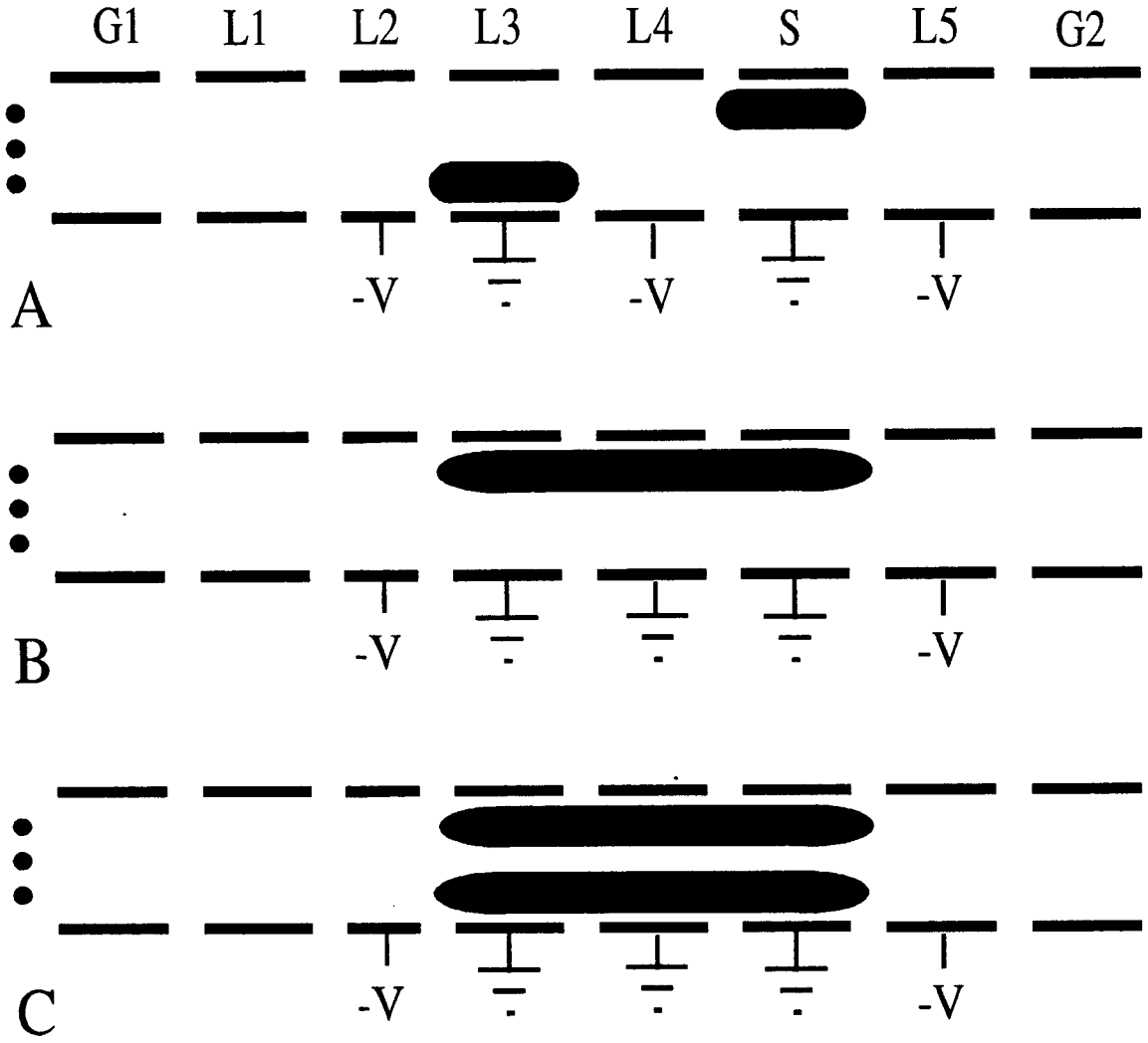

Figure 2.6: Model of Cascading. A: 2 columns before expansion. B: Final state of 1 column. C: Final state of 2 columns.

It is necessary to make some approximations in order to get a simple analytic estimate of the amount of heating done by cascade heating, and the effect on this of another column. I first make the approximation that the energy which goes into heating, as a result of a 3D cascade, is equal to the energy lost when the line density is halved. The idea behind this is that when the cut gate lowers in a time $\tau_{cut} = 0.75$ μsecs $\sim 2\tau_{bounce}$, the column will adiabatically expand until it is halfway through the cut gate, and then freely expand until its length doubles. This picture is consistent

with the above measurements.

This approximation greatly simplifies things by changing the problem into a 2D one. It is now merely necessary to calculate the electrostatic energy (per unit length) of a 2D column as a function of the relevant variables, and the amount of heating is given by the energy differences before and after cascading. For the one column case, the energy difference will be given by simply halving N_L. For the general two column case, however, there will be interaction terms between the two columns after (but not before) the cascade, which will have to be taken into account.

I model the columns as circular, constant density columns of radius ρ_v and line density N_L (hence density $n = N_L/\pi\rho_v^2$). The notation for lengths is the same as used in the previous chapters, and summarized in Appendix E. I use subscripts 1 and 2 to designate the two columns, and I use primes to designate their images. Normalized distances are labeled by d_{ij}, and displacements from the axis are labeled by r_i. With the density and shape constraints, it is straightforward to do the integrals to calculate the 2D electrostatic energy $\mathcal{H}_\phi$ of a single displaced column:

$$H_\phi = \frac{1}{2}\int dr \int r\, d\theta\, n(r,\theta)\phi(r,\theta)$$

$$= e^2 N_{L1}^2 \left[\left[\frac{1}{4} - \ln(\rho_1)\right] + \left[\ln(1-r_1^2)\right]\right]. \qquad (A.2)$$

The prediction of the amount of energy ΔH_ϕ going into heating of $T_{||}$, therefore, is

$$\Delta H_\phi = H_\phi(N_{L1}) - H_\phi(\frac{N_{L1}}{2}) =$$

$$\frac{3}{4}e^2 N_{L1}^2 \left[\left[\frac{1}{4} - \ln(\rho_1)\right] + \left[\ln(1-r_1^2)\right]\right]. \qquad (A.3)$$

Since the containment voltages are adjusted to give both columns the same $T_{||}$ after cascading without the other column present, it is the value ΔH_ϕ of equation A.3 which has been equalized for both columns. I now estimate the effect of cascading into a containment region with a second column present, to check both the magnitude of the effect and its asymmetry.

The first column after cascading will have an additional energy term $H_{\phi 12}$ due to interaction with column 2 and its image:

$$\Delta H_\phi = H_\phi(N_{L1}) - \left(H_\phi(\frac{N_{L1}}{2}) + H_{\phi 12}\right) \tag{A.4}$$

where

$$H_{\phi 12} = e^2 \left[\frac{N_{L1}}{2}\right] \left[\frac{N_{L2}}{2}\right] \ln \left[\frac{d_{12}}{r_2 d_{12'}}\right] . \tag{A.5}$$

Similarly, column two will have an additional term $H_{\phi 21}$ given by

$$H_{\phi 21} = e^2 \left[\frac{N_{L1}}{2}\right] \left[\frac{N_{L2}}{2}\right] \ln \left[\frac{d_{12}}{r_1 d_{21'}}\right] . \tag{A.6}$$

An examination of these terms reveals that the change in the amount of cascade heating will be the same for both columns, independent of either line density or displacement. The symmetry in r_1 and r_2 follows from the identity $r_2 d_{12'} = r_1 r_2 + 1 = r_1 d_{21'}$, which is valid when $\theta_2 = \theta_1 + \pi$. As an estimate of how large the effect can be, when $r_1 = r_2 = 0.26$ and $\rho_v = 0.15$ (i.e. the columns are near merger), the columns are heated about 11% less than predicted by equation A.3.

Impact of Electron Plasma Waves

In a recent relevant study, Moody and Malmberg [51] studied the free expansion of a single on-axis column with similar plasma parameters to mine. They observed that a rarefraction front propagates through the plasma, eventually emptying the confinement region, at the phase velocities of long wavelength electron plasma waves. I have observed that naturally damped electron plasma waves are set up in the final confined state by free expansion during cascading. However, I found that the dynamics after cascading were not changed when resistive damping of the plasma waves was added, and have concluded that these waves do not impact the subsequent 2D dynamics. Driscoll [16] has similarly studied the plasma waves set up

during the hollowing of a column, and found no impact on the subsequent instability evolution to be caused by the waves.

Density Transport During Cascading

Rearrangement of the $r - \theta$ density profile was often observed to occur as a consequence of cascading, with the amount dependent on the experimental parameters during the cascading. The mechanism, presumably, is that z-dependent drifts occur while part of the column is spilling over the cut gate. This suggests that increasing B_z or decreasing τ_{cut} should reduce the amount of transport, which has been seen to be the case. This is why a value of $\tau_{cut} \approx 0.75\mu$secs was used for the experiments of this dissertation: it is fast enough to keep the transport low, while slow enough to avoid unnecessary heating.

Appendix B

Analysis of the Wall Sector Signals From Two Vortices

I have described the sector probe signals resulting from a single vortex in section 2.4.3. The signal when two vortices are contained is simply the superposition of the signals from each. The more complicated dynamics of the two vortex system result in the signals being harder to interpret, yet with practice a qualitative knowledge of the state of the system can be had with a glance. In addition, spectral analysis of the signals permits a quick quantitative measurement of the frequencies of the motions.

Oscillations About Stable $r_1 = r_2$ Equilibria

Figure B.1 shows 2 examples of wall sector signals induced by vortices at or near stable $r_1 = r_2$ equilibrium points. The top signal is from two vortices very near the equilibrium points. In the rotating frame of the orbit motion, these vortices are stationary, and the resultant waveform is a sinusoid at twice the orbit frequency, $2f_{orb}$. The second signal is produced by two vortices injected somewhat away from stable equilibrium points. These then oscillate at frequency f_{osc} about the equilibrium points, and their oscillatory radial motion produces the amplitude modulation visible on the $2f_{orb}$ signal.

Below the second waveform is a Fourier transform of it; the two largest components are the $2f_{orb}$ peak and a peak at $f_{orb} - f_{osc}$. Fourier transforms of sector signals thus provide a fast determination of f_{orb} and f_{osc}. The values determined by this method have been compared with those derived from time series of density plots, and found to be consistent with them.

Oscillations About Stable $r_1 > r_2$ Equilibria

I have also observed equilibrium points where r_1 and r_2 are not the same. I use a convention that r_1 is the larger radial position, and term these $r_1 > r_2$ equilibrium points. Figure B.2, analogous to figure B.1, shows the sector signals resulting from unperturbed and perturbed motions about these equilibria.

The Fourier transform (also shown) of the perturbed motions has a large component at f_{orb} because of the asymmetry of the radial positions of the vortices. The oscillatory motions at frequency f_{osc} appear in the spectra here as as sidebands about the f_{orb} frequencies. The reason for this difference from the spectra of the $r_1 = r_2$ oscillatory motions it that the vortices oscillate differently in the rotating frame; this can be seen in figure 4.4 where I have indicated with arrows the directions of the oscillations.

Exponential Growth From Unstable $r_1 \neq r_2$ Equilibria

I show an example of a sector probe signal from vortices injected near unstable $r_1 = r_2$ equilibrium points in figure B.3. As the $H(r_1, \theta_1 - \theta_2, P_\theta)$ plots described in section 4.4.4 show, such vortices execute large orbits away from the unstable equilibrium points. Fourier transforms of these waveforms show many frequencies, but can not be used to determine the rates γ at which the vortices exponentiate away. I have marked the peak belonging to one of the vortices: the large changes in

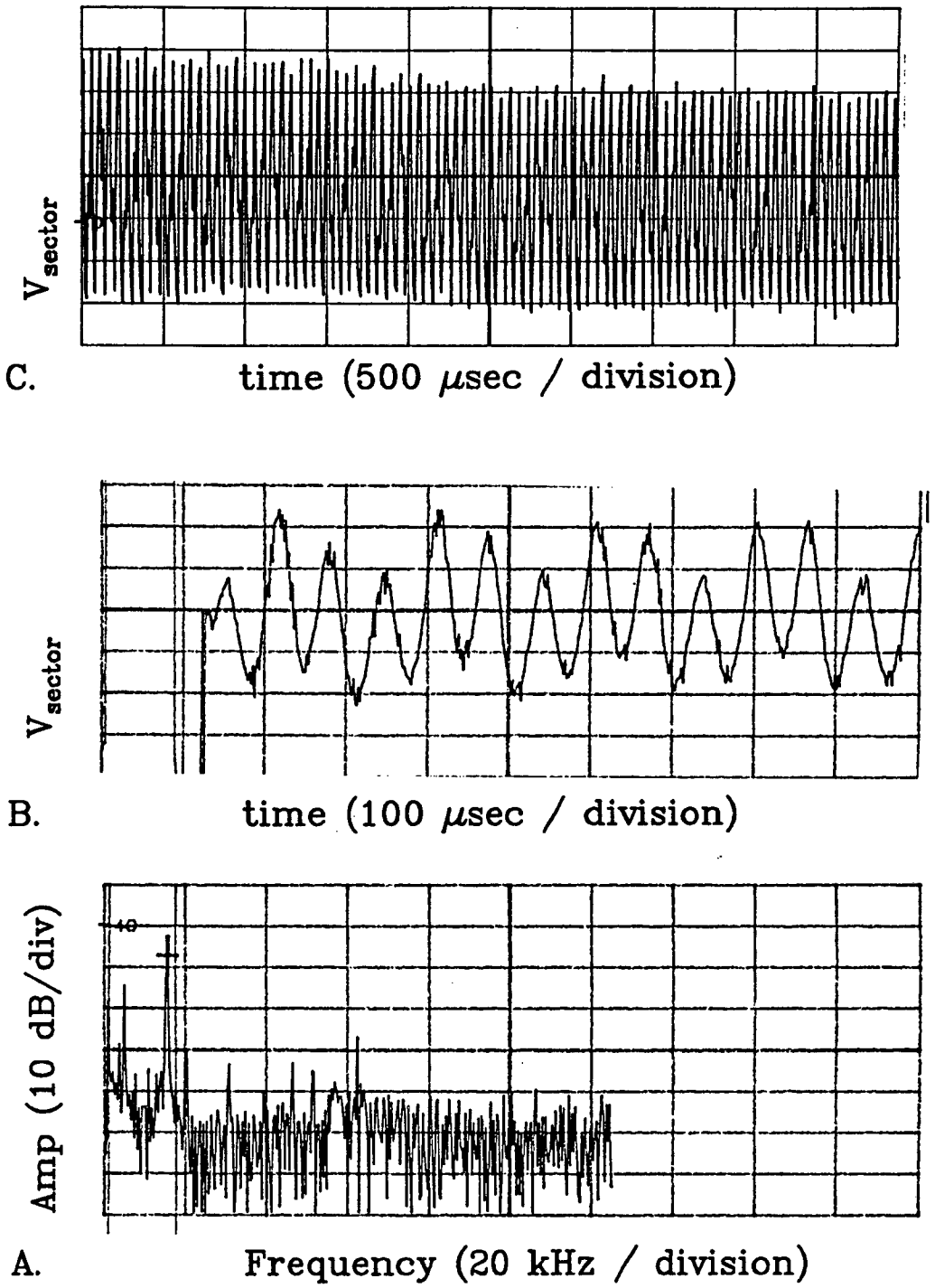

Figure B.1: Sector probe signals and Fourier transform, for two vortices at and near stable $r_1 = r_2$ equilibrium points. A: signals from vortices on equilibria. B: signals from vortices oscillating about equilibria. C: Fourier transform of B.

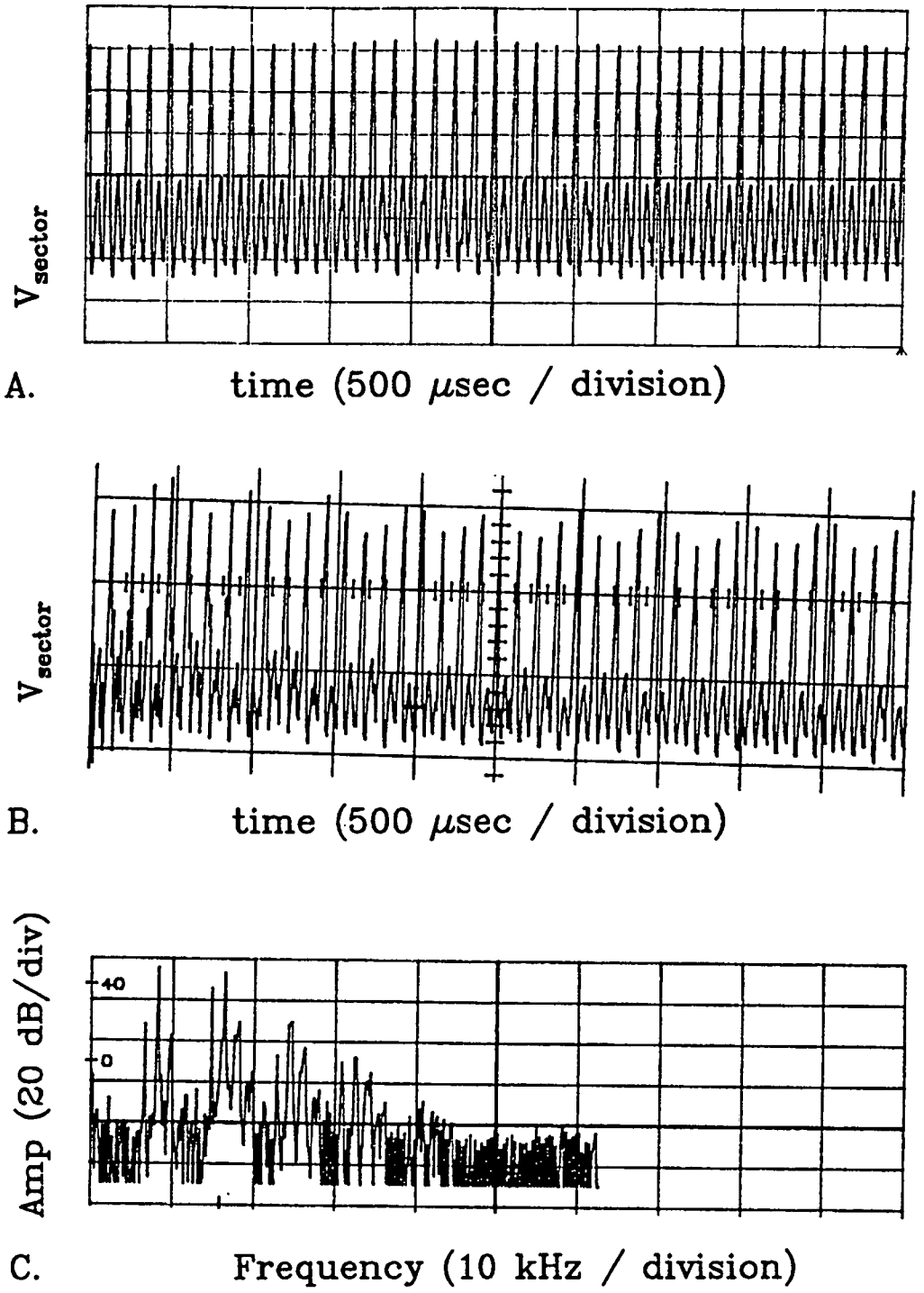

Figure B.2: Sector probe signals and Fourier transform, for two vortices at and near stable $r_1 > r_2$ equilibrium points. A: signals from vortices on equilibria. B: signals from vortices oscillating about equilibria. C: Fourier transform of B.

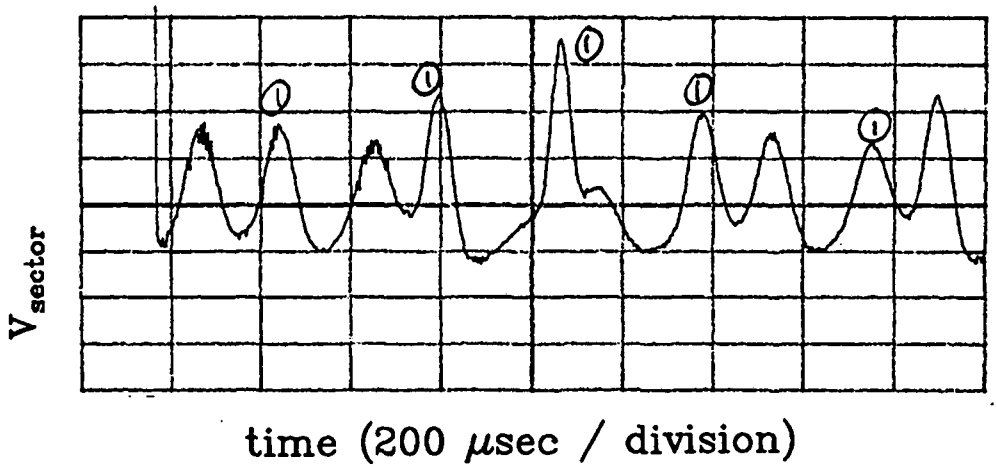

Figure 2.6: The sector probe signal when two vortices are injected onto unstable $r_1 = r_2$ equilibrium points.

r and $\theta_2 - \theta_1$ of the system are apparent.

The wall sector signals permit a determination of the position of the unstable equilibrium points. As the θ-phase of the initial condition is varied, the signals change accordingly. At a specific θ-phase, it is observed that the signal randomly displays one of two forms. This initial condition corresponds to the vortices being injected at the X-point of the energy contour plots; the shot-to-shot noise of the system determines which vortex moves out and which moves in radially. When the initial condition of this state is measured, it is found to be at $r_1 = r_2$ and $\theta_2 - \theta_1 = \pi$, within the measurement uncertainty.

Appendix C

Analysis of Vortex Motion Data

The most direct way of investigating vortex motions is to take a series of phase-locked plots showing the vortices at various times t_k. The 2D plots are then reduced to yield a set of center-of-vorticity positions $[r_i(t_k), \theta_i(t_k)]$, where the subscript i denotes vortex 1 or 2. This has been done for a wide variety of initial conditions with a focus, however, on vortices with small perturbations from known equilibrium points (r_i, θ_i) orbiting about the center with a frequency f_{orb}. The position data sets have then been analyzed to determine the time evolution of the perturbations $\delta r_i(t)$ and $\delta\theta_i(t)$:

$$r_i(t) = r_i + \delta r_i(t) \qquad \theta_i(t) = \theta_i + 2\pi f_{orb} t + \delta\theta_i(t) \; . \tag{C.1}$$

The analysis (as shown above in section 4.3) reveals that the evolutions of the perturbations are well-described as either oscillations about stable equilibrium points at a frequency f_{osc}, or as exponentiation at a rate $\pm\gamma$ from unstable points. This is in agreement with the predictions of point vortex theory. In this appendix I describe the reduction of the position data to yield frequencies and rates, and display examples of evolution about stable and unstable equilibrium points. The analysis consists of fitting a trial function to the data set, using a non-linear fitting subroutine (DNLS1) from SLATEC. DNLS1 uses a modification of the Levenberg-Marquardt algorithm to minimize the sum of the squares between the data set and the trial

function.

C.1 Oscillatory Motion Analysis

An example of data showing oscillatory motion about stable equilibrium points is shown in figure C.1. (This data set has previously been plotted in (r, θ) coordinates in a rotating frame in figure 4.4a, and on contours of $H[r_i(t), \theta_i(t) - \theta_j(t)]$ in figure 4.6.) The vortices were initially injected at the same radial position $r_1 = r_2 = .36$, but with a θ-perturbation from the stable equilibrium point at $\theta_2 = \theta_1 + \pi$. Oscillatory motion can clearly be seen.

In fitting an oscillatory motion at a single frequency f_{osc} to the data, there will be 18 unknowns since each of the four variables will have its own frequency, amplitude, phase, etc. However, an examination of the raw data suggests that the perturbations at each of the four coordinates are oscillating not only at a single frequency, but also with specific amplitude and phase relations between each other. It has in fact been found that a fit to a more constrained function, which imposes the symmetries seen in the data, results in residuals not significantly larger than those when these symmetries are not imposed. The constrained function is

$$r_i(t) = r_i + A_i \cos\left(2\pi f_{osc} t + \pi\phi_i\right) ,$$

$$\theta_i(t) = \theta_i + 2\pi f_{orb} t + B_i \cos\left(2\pi f_{osc} t + \pi\phi_i + \frac{\pi}{2}\right) \qquad \text{(C.2)}$$

with the constraints $A_1 = -A_2$, $B_1 = -B_2$, and $\phi_1 = \phi_2$. This is then a fit to 9 unknowns, the four equilibrium position variables $(r_1, \theta_1, r_2, \theta_2)$, two frequencies (f_{osc}, f_{orb}), 2 amplitudes (A_1, B_1) and one phase (ϕ_1). The function resulting from the fit has been plotted (lines) in figure C.1. I have also plotted there the $\theta_i(t)$ position residuals when the orbital motion and equilibrium positions are subtracted off. (This subtraction allows easier viewing of the θ oscillation motion.)

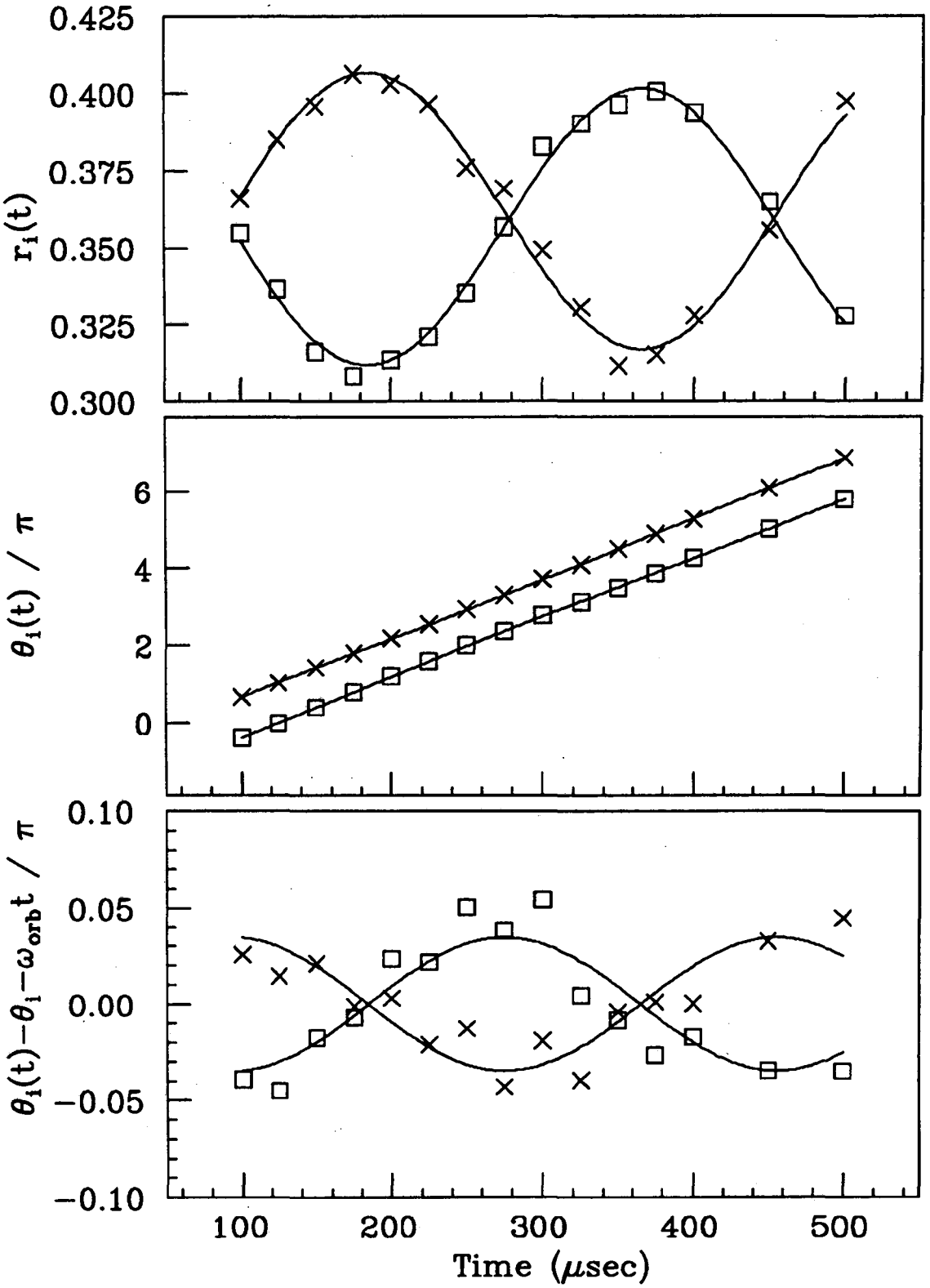

Figure C.1: Radial positions, θ positions, and θ residuals versus time, for two vortices oscillating about stable equilibrium points. The lines are fits to the data, as described in the text.

I can now make comparisons between the fitted motion and the predictions of point vortex theory. Let me first note that several point vortex predictions have automatically been incorporated into the fit by the constraints, such as the predictions that radial and θ perturbations will oscillate at the same frequency and be $\pi/2$ out of phase with each other, and that the two vortices will have equal perturbation amplitudes. For these predictions, the goodness of the fit (of the constrained trial function to the data) is the evidence that they are valid. When the constraints are relaxed, the resultant decrease in the fit residuals is not sufficiently great to indicate that the constraints are not appropriate.

One prediction of point vortex theory is that the equilibrium positions will be at $r_1 = r_2$ and $\theta_2 - \theta_1 = \pi$. The measured values are $r_1 = .362$, $r_2 = .358$, and $\theta_1 - \theta_2 = 1.000\pi$. These values agree, within the measurement uncertainties, with the theory prediction.

Another point of comparison is of the relative size of the perturbation amplitudes δr_i and $\delta\theta_i$. The fit gives a value $\delta r_i/\delta\theta_i = 0.4114$, which agrees with the point vortex theory prediction of 0.4109. In general, the experimental agreement of the measured eigenfunctions with theory is good.

C.2 Exponential Motion Analysis

In figure C.2 I show an example of two vortices moving away from unstable equilibrium points. This particular data set has previously plotted, in (r, θ) coordinates in a rotating frame, in figure 4.4c. The initial condition consisted of $r_1 = r_2 = .572$, and $\theta_2 - \theta_1 = 0.923\pi$.

When using an unweighted least-squares algorithm to fit an exponentially growing function, it is not feasible to keep the values from which the perturbations grow as free parameters: the fitter will typically reduce the residuals by moving the

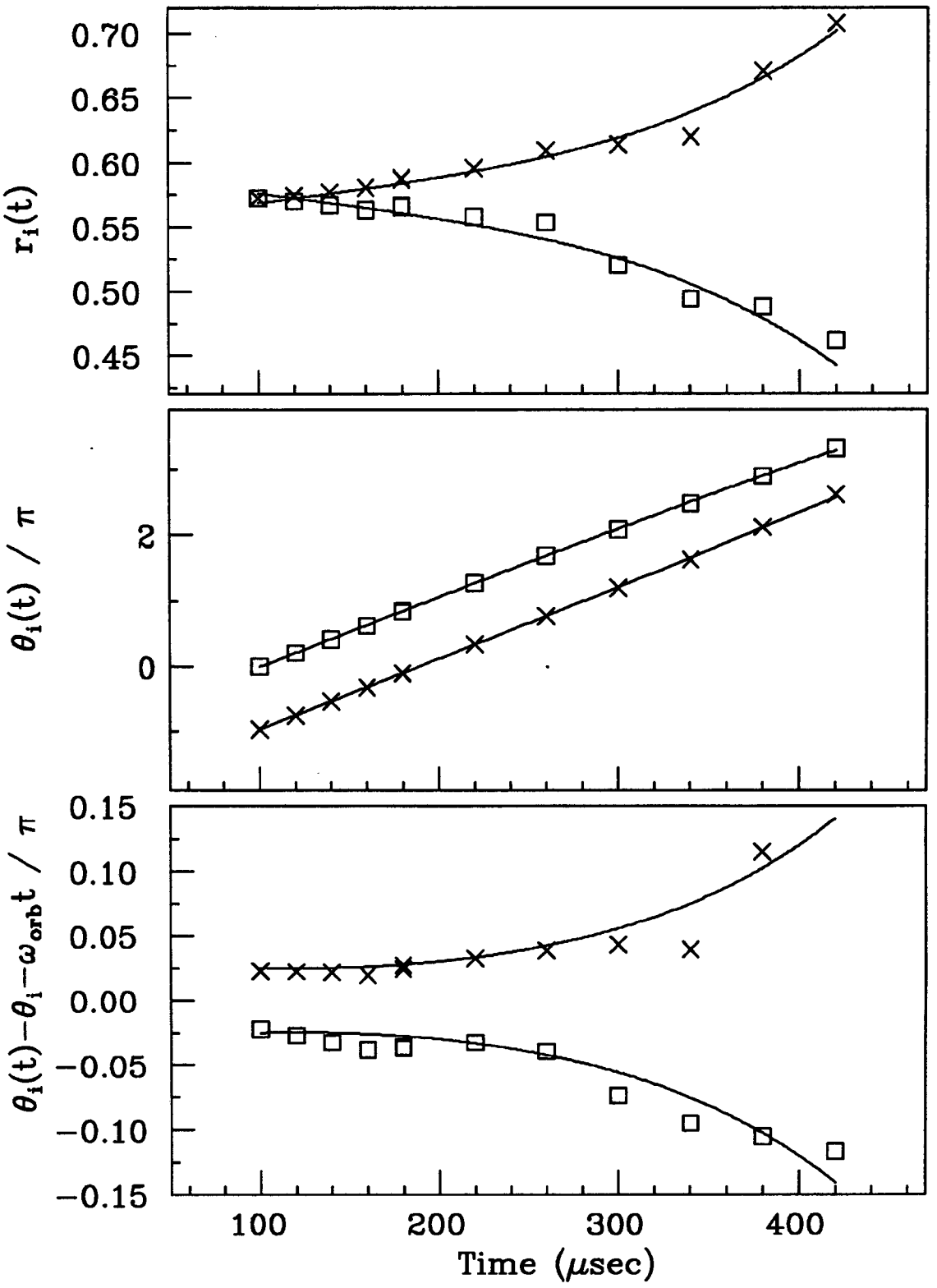

Figure C.2: Radial positions, θ positions, and θ residuals versus time, for two vortices exponentiating away from unstable equilibrium points. The lines are fits to the data, as described in the text.

solution away from the known initial values. However, the (unstable) equilibrium points have previously been determined to be at $r_1 = r_2$ and $\theta_2 - \theta_1 = \pi$ from other observations, as discussed in Appendix B.

The constrained fit function is then

$$r_i(t) = r_i + A_i \exp(\gamma t) + C_i \exp(-\gamma t)$$

$$\theta_i(t) = \theta_i + B_i \exp(\gamma t) + D_i \exp(-\gamma t) + 2\pi f_{orb} t \,. \tag{C.3}$$

In addition to not fitting to r_i, θ_i, an additional constraint has been applied by setting $A_i/B_i = C_i/D_i$. This constraint causes the growing and decaying eigenvectors to have the same form, which is a prediction from point vortex theory is seen to be valid in the data. The fit is thus to 5 unknowns, A_i, B_i, C_i, f_{orb} and γ. The function resulting from the fit is shown (lines) on figure C.2. Examining the eigenfunctions again, the fit shows that $\delta r_i/\delta\theta_i = 0.274$, while point vortex theory predicts 0.299.

Appendix D

Linear Stability Analysis of Two Vortices in a Circular Boundary

In this appendix I determine the stability of perturbations about the equilibrium points of two point vortices in a circular boundary. The analysis for the equilibria with $r_1 = r_2$ has been done previously by Havelock [34]. Here, I extend the analysis to include equilibria where $r_1 \neq r_2$. At the end, I additionally discuss two cases where workers have found results contradicting Havelock's. I have investigated these cases numerically, and find Havelock vindicated on both counts.

Point Vortex Statics

The velocity field generated by a single point vortex of circulation Γ, with no boundaries, is everywhere in the azimuthal direction $\hat{\theta}$ about the vortex, and with the magnitude inversely proportional to the distance d to the vortex:

$$| \mathbf{v}_\theta | = \frac{\Gamma}{2\pi d} . \tag{D.1}$$

The direction of the velocity vector is as given by the right hand rule. In the case of a line charge of line density N_L in a magnetic field B, the velocity field is similarly given by

$$| \mathbf{v}_\theta | = \frac{4\pi e c N_L}{B} \frac{1}{2\pi d} , \tag{D.2}$$

which displays the analogy between circulation and line density of $\Gamma = (4\pi ecN_L)/B$.

It is straightforward to include the effects caused by a circular boundary of radius R_w. The method of images provides a simple analytic way of calculating the fields required by the boundary condition, which requires an equipotential surface at $R = R_w$. It can be shown [26] that the image fields induced by a vortex of circulation Γ at an interior position (R, θ), are the same as those produced by an image vortex of circulation $-\Gamma$ at a position $(R_w^2/R, \theta)$. Here, the origin of the coordinate system is at the center of the boundary.

Equilibrium Positions

I have previously discussed the equilibrium positions of 2 vortices in section 4.4.1. Equilibrium for a vortex configuration requires that there be no net radial velocities V_r, and that the vortices have net azimuthal velocities V_θ which give the same orbit frequency for both vortices about the center. This results in the vortices remaining in the same relative positions while the configuration orbits about the central axis.

An examination of the geometry makes it clear that the only possible equilibrium positions for two vortices must be on opposite sides of the origin, i.e. $\theta_2 = \theta_1 + \pi$. The positions of such equilibria are easily solved for, and in addition to the $R_1 = R_2$ equilibria, equilibria with $R_1 \neq R_2$ are also found to exist. These equilibrium positions have been plotted in figure 4.3, using the convention $R_1 > R_2$.

Stability Analysis: Definitions

With the equilibrium positions known, one can do a linear stability analysis to determine their stability. I use the following conventions in the analysis:

- The indexing between vortices is done with subscripts, where images are indicated with primes on the respective index (i.e. $1, 1', 2, 2'$).

- The equilibrium positions are given by R_i, θ_i, and $\delta R_i, \delta\theta_i$ indicate perturbations about these positions.

- I designate distances between vortices/images by D_{ii} where the subscripts indicate which distance. An example is $D_{11'}$, which is the distance between vortex 1 and its image.

- I decompose the velocity vector $\mathbf{V} = V_r\hat{r} + V_\theta\hat{\theta}$ into components where the first subscript indicates which vortex has that velocity component, and the second indicates which vortex or image is causing that particular contribution. An example is $V_{\theta 12'}$, which is the azimuthal velocity of vortex 1, as caused by the presence of the image of vortex 2.

- The first order velocity components are distinguished from the exact ones by being lower-case, e.g. $v_{\theta 12'}$ is the same velocity as above, but to first order in δr and $\delta\theta$.

- In the analysis, lengths are normalized to the wall radius R_w. This normalization is similarly indicated with the use of the relevant lowercase variable.

Vortex	Radial Position	Azimuthal Position
1	$r_1 + \delta r_1$	$\theta_1 + \delta\theta_1$
$1'$ (image)	$(r_1 + \delta r_1)^{-1}$	$\theta_1 + \delta\theta_1$
2	$r_2 + \delta r_2$	$\theta_1 + \pi + \delta\theta_2$
$2'$ (image)	$(r_2 + \delta r_2)^{-1}$	$\theta_1 + \pi + \delta\theta_2$

Table D.1: Positions of perturbed vortices and their images.

The perturbed vortices and their images thus have the (normalized) positions tabulated in table D.1. I show the two vortex system coordinates in figure D.1.

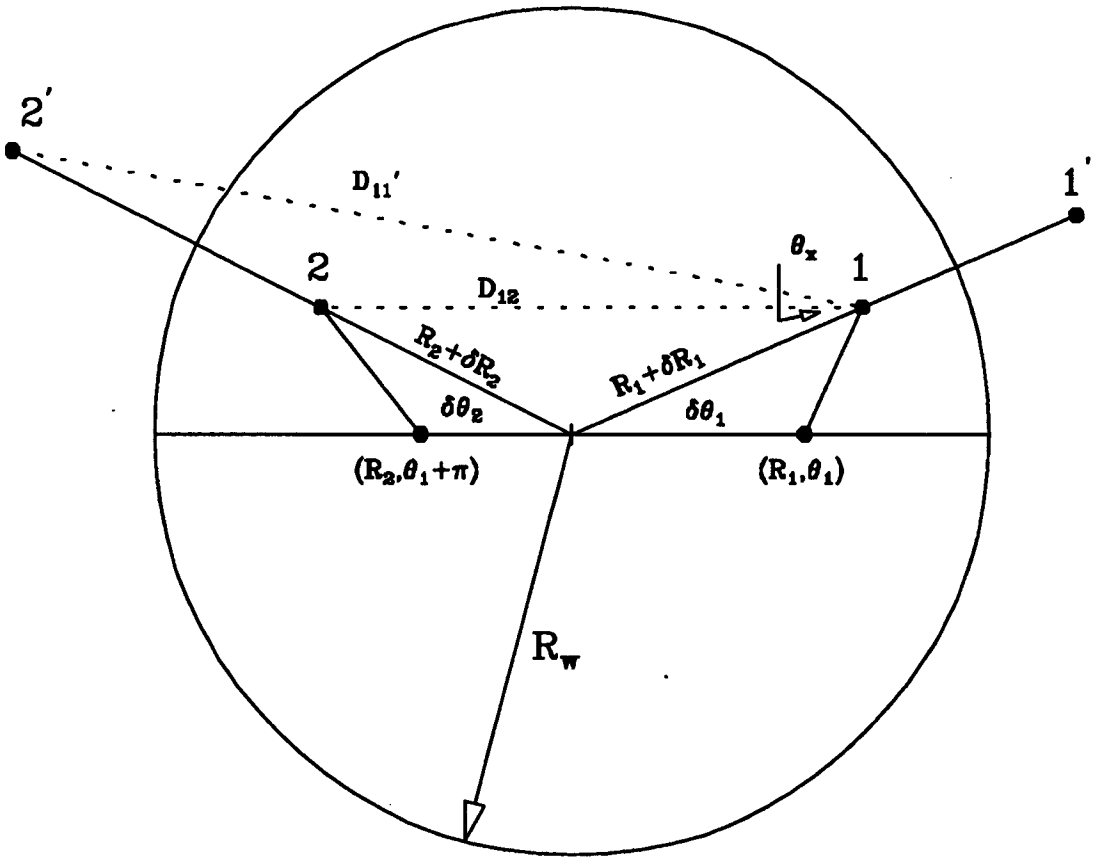

Figure D.1: Coordinates for the linear stability analysis of equilibria.

A needed quantity is the angular orbit frequency ω_{orb} with which vortex 1 will orbit about the origin:

$$\omega_{orb}(r_1, r_2) = \frac{\Gamma}{2\pi}\frac{1}{r_1}\left[\frac{1}{r_1 + r_2} - \frac{1}{1/r_2 + r_1} + \frac{1}{1/r_1 - r_1}\right] , \qquad \text{(D.3)}$$

where the 3 terms are from the velocity contributions of vortex 2, image 2 and image 1 respectively. The orbit frequency of vortex 2, which must equal that of vortex 1 at equilibrium points, is given by $\omega_{orb}(r_2, r_1)$. This is a general feature of the formulas calculated below: as a consequence of the symmetry of the vortices in Γ, the equations for the velocities of vortex 2 are given by interchanging the subscripts $1 \Leftrightarrow 2$. Therefore, I won't display the equivalent vortex 2 equations.

The strategy of the analysis is to work out the rate of change of the perturbations as a function of the relevant variables. I first work out the azimuthal velocity components of vortex 1, and then (taking into account the above orbital motion) its θ-perturbation will evolve (to first order) as:

$$\delta\dot{\theta}_1 = \frac{1}{r_1}\left[(v_{\theta 12} + v_{\theta 11'} + v_{\theta 12'}) - (r_1 + \delta r_1)\,\omega_{orb}\right] . \tag{D.4}$$

Next, I calculate the radial velocity components to get the first order evolution of the radial perturbation:

$$\delta\dot{r}_1 = v_{r12} + v_{r11'} + v_{r12'} \tag{D.5}$$

In order to decompose the velocities into radial and azimuthal components, it is necessary to first solve for the angle θ_x, which is the angle a line between the relevant vortices makes with the radial vector of the moving vortex. The angle is pointed out in figure D.1, for the case where the velocity components of vortex 1, resulting from vortex 2, are being calculated. I find

$$\cos(\theta_x) = \frac{(r_1 + \delta r_1) - (r_2 + \delta r_2)\cos(\pi + \delta\theta_2 - \delta\theta_1)}{d_{12}} \tag{D.6}$$

and

$$\sin(\theta_x) = \frac{(r_2 + \delta r_2)\sin(\pi + \delta\theta_2 - \delta\theta_1)}{d_{12}} . \tag{D.7}$$

Azimuthal Velocity Components

The azimuthal contribution from vortex 2 is then

$$V_{\theta 12} = \frac{\Gamma}{2\pi}\frac{\cos(\theta_x)}{d_{12}} = \frac{\Gamma}{2\pi}\frac{(r_1 + \delta r_1) - (r_2 + \delta r_2)\cos(\pi + \delta\theta_2 - \delta\theta_1)}{d_{12}^2} , \tag{D.8}$$

and to first order in δr and $\delta\theta$ this is

$$v_{\theta 12} = \frac{\Gamma}{2\pi}\frac{1}{r_1 + r_2}\left[1 - \frac{\delta r_1}{r_1 + r_2} - \frac{\delta r_2}{r_1 + r_2}\right] . \tag{D.9}$$

Similarly,

$$V_{\theta 11'} = \frac{\Gamma}{2\pi}\frac{1}{d_{11'}} = \frac{\Gamma}{2\pi}\left[\frac{1}{r_1+\delta r_1} - (r_1+\delta r_1)\right]^{-1} \tag{D.10}$$

and

$$v_{\theta 11'} = \frac{\Gamma}{2\pi}\left[\frac{r_1}{1-{r_1}^2} + \frac{(1+{r_1}^2)\,\delta r_1}{(1-{r_1}^2)^2}\right] .$$

The $V_{\theta 12'}$ term is similar to the $V_{\theta 12}$ term:

$$V_{\theta 12'} = \frac{-\Gamma}{2\pi}\frac{(r_1+\delta r_1) - (r_2+\delta r_2)^{-1}\cos(\pi+\delta\theta_2-\delta\theta_1)}{d_{12'}^2} ,$$

but the first order expansion is larger:

$$\begin{aligned} v_{\theta 12'} = \frac{\Gamma}{2\pi}\Bigg[& -\frac{r_1}{{r_1}^2+{r_2}^{-2}+\frac{2r_1}{r_2}} - \frac{1}{\left({r_1}^2+{r_2}^{-2}+\frac{2r_1}{r_2}\right)r_2} + \\ & \frac{2{r_1}^2\delta r_1}{\left({r_1}^2+{r_2}^{-2}+\frac{2r_1}{r_2}\right)^2} - \frac{\delta r_1}{{r_1}^2+{r_2}^{-2}+\frac{2r_1}{r_2}} + \frac{2\delta r_1}{\left({r_1}^2+{r_2}^{-2}+\frac{2r_1}{r_2}\right)^2{r_2}^2} + \\ & \frac{4r_1\delta r_1}{\left({r_1}^2+{r_2}^{-2}+\frac{2r_1}{r_2}\right)^2 r_2} - \frac{2\delta r_2}{\left({r_1}^2+{r_2}^{-2}+\frac{2r_1}{r_2}\right)^2{r_2}^4} - \frac{4r_1\delta r_2}{\left({r_1}^2+{r_2}^{-2}+\frac{2r_1}{r_2}\right)^2{r_2}^3} - \\ & \frac{2{r_1}^2\delta r_2}{\left({r_1}^2+{r_2}^{-2}+\frac{2r_1}{r_2}\right)^2{r_2}^2} + \frac{\delta r_2}{\left({r_1}^2+{r_2}^{-2}+\frac{2r_1}{r_2}\right){r_2}^2}\Bigg] \end{aligned} \tag{D.11}$$

Radial Velocity Components

The radial components of the velocity are given by:

$$V_{r11'} = 0 , \tag{D.12}$$

$$V_{r12} = \frac{\Gamma}{2\pi}\frac{(r_2+\delta r_2)\sin(\pi+\delta\theta_2-\delta\theta_1)}{d_{12}^2} , \tag{D.13}$$

$$v_{r12} = \frac{\Gamma}{2\pi}\frac{r_2(\delta\theta_1-\delta\theta_2)}{{r_1}^2+2r_1r_2+{r_2}^2} , \tag{D.14}$$

$$V_{r12'} = \frac{-\Gamma}{2\pi}\frac{(r_2+\delta r_2)^{-1}\sin(\pi+\delta\theta_2-\delta\theta_1)}{d_{12'}^2} , \tag{D.15}$$

and

$$v_{r12'} = \frac{\Gamma}{2\pi}\frac{\delta\theta_2-\delta\theta_1}{\left({r_1}^2+{r_2}^{-2}+\frac{2r_1}{r_2}\right)r_2} . \tag{D.16}$$

When the first order velocity components are assembled as shown in equations D.5 and D.4, we have expressions (which I will not write out) for the perturbations of the form

$$\delta\dot{r}_1 = f\left(r_1, r_2, \delta\theta_1, \delta\theta_2\right) \quad \text{and} \quad \delta\dot{\theta}_1 = f\left(r_1, r_2, \delta r_1, \delta r_2\right) , \tag{D.17}$$

and similar equations for the second vortex. We thus have 4 equations and 4 unknowns.

Angular momentum conservation, however, requires (to first order) $\delta r_1 = -\delta r_2 \left(r_2/r_1\right)$ and therefore $\delta\dot{r}_1 = \delta\dot{r}_2 \left(r_2/r_1\right)$. When the two radial velocities expressions are written out it is found that they are indeed dependent, and so there are 3 equations and 3 unknowns.

Symmetric ($r_1 = r_2$) Equilibria

These equilibria were first considered by Havelock in 1931 [34]. For these equilibria, the equations give $\delta\dot{r}_2 = -\delta\dot{r}_1$ and $\delta\dot{\theta}_2 = -\delta\dot{\theta}_1$, which implies symmetric perturbations of the form

$$\delta\theta_2 = -\delta\theta_1 \quad \text{and} \quad \delta r_2 = -\delta r_1 . \tag{D.18}$$

Writing out the equations for vortex 1 using $r_1 = r_2 \equiv d$, we find

$$\delta\dot{r}_1 = \frac{\delta\theta_1}{d}\left[\frac{1}{2} - \frac{2d^2}{\left(1+d^2\right)^2}\right] \equiv \delta\theta_1 \mathcal{A} , \tag{D.19}$$

and

$$\delta\dot{\theta}_1 = \frac{\delta r_1 \left(7d^6 - 3d^4 + 5d^2 - 1\right)}{2\left(d-1\right)^2 d^3 \left(1+d\right)^2 \left(1+d^2\right)} \equiv \delta r_1 \mathcal{B} , \tag{D.20}$$

where $\mathcal{A}$ and $\mathcal{B}$ are functions of d only. Equations D.19 and D.20 are the same as Havelock's equation 24, when the typographical errors noted by Campbell [6] are corrected.

Taking the time derivative of one of the relations, and plugging in the other, we find

$$\delta\ddot{r}_1 = \delta r_1 \mathcal{AB} \quad \text{and} \quad \delta\ddot{\theta}_1 = \delta\theta_1 \mathcal{AB} \,. \tag{D.21}$$

These have trivial solutions of the form

$$\delta r_1(0) e^{[\mathcal{AB}]^{1/2}} \quad \text{and} \quad \delta\theta_1(0) e^{[\mathcal{AB}]^{1/2}} \tag{D.22}$$

The stability of the perturbations is easily found: if $\mathcal{AB} < 0$ the perturbations will oscillate about the equilibrium points, with the δr and $\delta\theta$ oscillations $\pi/2$ radians out of phase with each other, and the oscillation frequency given by $\mid \mathcal{AB} \mid^{1/2}$. If $\mathcal{AB} > 0$, however, the perturbations will exponentially grow from the unstable points at a rate $\gamma = (\mathcal{AB})^{1/2}$. The quantity $\mathcal{AB}$ is negative for $0 < d < .4623$ and positive for $.4623 < d < 1$. The eigenfunctions are found from plugging the solutions of D.22 into equation D.19, which gives

$$\delta r_1(0) \, [\mathcal{AB}]^{1/2} = \delta\theta(0) \mathcal{A} \,, \tag{D.23}$$

indicating the relative size of the radial and azimuthal perturbations as a function of d.

Asymmetric ($r_1 \neq r_2$) Equilibria

If we do not have the condition $r_1 = r_2$, then the general result for the velocities of the perturbations is

$$\delta\dot{r}_1 = (\delta\theta_2 - \delta\theta_1)\, \mathcal{C} \qquad \dot{\theta}_1 = \delta r_1 \mathcal{D} \quad \text{and} \quad \dot{\theta}_2 = \delta r_1 \mathcal{E} \,, \tag{D.24}$$

where I have used $\delta r_2 = -\delta r_1 (r_1/r_2)$ to reduce the equations, and where $\mathcal{C}, \mathcal{D}$ and $\mathcal{E}$ are functions of r_1 and r_2. (I do not print these here because they are fairly large.)

The same eigenfunction stability analysis applies here as in the $r_1 = r_2$ case, with $\mathcal{C}(\mathcal{E} - \mathcal{D})$ the relevant quantity instead of $\mathcal{AB}$. As discussed in section 4.4.1,

the analytic expressions for the $r_1 > r_2$ equilibrium positions are large, but the positions are easily found to arbitrary precision numerically. Plugging in these values in order to evaluate $\mathcal{C}(\mathcal{E} - \mathcal{D})$ establishes that this quantity is negative for all $r_1 > r_2$ equilibrium points, indicating stability. I have previously plotted the predicted frequency $\mid \mathcal{C}(\mathcal{E} - \mathcal{D}) \mid^{1/2}$ of these oscillations, in figure 4.5.

In terms of the eigenfunctions, the symmetry of the oscillations is broken (as it must be to conserve angular momentum), and vortex 2 executes larger orbits than vortex 1. In addition, these oscillations also differ in having $\delta\theta_1$ and $\delta\theta_2$ of the same sign. An example of an $r_1 > r_2$ oscillation, as viewed in a rotating frame, can be seen in figure 4.4b, where both the theory (line) and the experimental results (symbols) are shown.

Subsequent Discrepancies with Havelock's Results

Havelock [34] worked out the stability of vortices in $r_1 = r_2$ equilibrium positions in a general form valid for an arbitrary number N of vortices. Among his findings was that a symmetric ring of vortices (with no boundary) is stable for $N < 7$, neutrally stable for $N = 7$ and unstable for $N > 7$. This particular result has relatively recently (1979) been contradicted by Katyshev *et. al.* [39], who using both linear perturbation theory and numerical simulations found the $N = 8$ case to be stable (and $N > 8$ to be unstable). Katyshev's results are erroneous, as will be discussed below. A previous similar discrepancy - Thomson's [67] finding that the $N = 7$ ring is unstable - has been found to be a consequence of a slight error.

Havelock also worked out the general forms, for the same ring stability problem, of the case where circular boundaries are present either inside or outside the ring. (The latter condition, with $N = 2$, is the $r_1 = r_2$ problem I worked out above in explicit form.) He found that the outside boundaries resulted in making unstable

the otherwise stable $N < 8$ cases, when the radii of the rings exceeded a critical value (normalized to R_w) $r_{critical}$. The critical value for the $N = 2$ case is $r_H = 0.4623$. Some of his predictions for $r_{critical}$ disagree with the 1981 results of Campbell [6], who found agreement with Havelock for the $r_{critical}$ of even number of vortices, but "for odd N Havelock's formulas predict larger critical radii than are found by the eigenfunction calculations. The source of this discrepancy, which far exceeds numerical uncertainty, is not known." The largest discrepancy cited was for 3 vortices, where Campbell found $r_{critical} = 0.55142$, while Havelock found $r_{critical} = 0.56682$.

To investigate these two discrepancies (and other issues), I wrote a vortex dynamics simulator utilizing a Bulirsch-Stoer algorithm integrator [59] to follow the evolution of an arbitrary number of vortices forward in time. The integrator has been checked by making sure that the usual conserved quantities, angular momentum and electrostatic energy, were conserved. I found that for the $N = 3$ ring within a circular boundary, vortices put at equilibrium points at radii up to and including $d = 0.56682$ remained there for (at least) tens of orbit periods, while vortices placed at $d = 0.5690$ had their perturbations from the equilibrium points grow quickly and exponentially. I concluded that these results support Havelock's prediction, and not Campbell's. I then removed the effects of the boundary, and examined the evolutions of $N = 7$ and $N = 8$ rings. I found that a ring of 7 vortices will stably orbit for (at least) many tens of orbits, while a ring of 8 vortices quickly breaks up. I concluded that Havelock had again been vindicated.

Appendix E

Frequently Used Symbols

********** **Energies** **********

$\mathcal{H}_\phi$	Eq. 2.8	2D electrostatic energy
H_ϕ	Eq. 4.8	scaled 2D electrostatic energy
$\mathcal{H}_{\phi e}$	Eq. 2.6	3D electrostatic energy
$\mathcal{H}_\perp$		kinetic energy perpendicular to magnetic field
$\mathcal{H}_\parallel$		kinetic energy parallel to magnetic field
T		plasma temperature
$T_\parallel$		temperature parallel to magnetic field
$T_\perp$		temperature perpendicular to magnetic field
T_{eq}	$(2T_\perp + T_\parallel)/3$	equilibrium temperature

********** **Densities** **********

$n_e(r,\theta,z)$		3D density
$n(r,\theta)$	Eq. 2.7	2D (z-averaged) density
$N_{Le}(z)$	Eq. 2.1	line density
N_L	Eq. 2.2	line density at $\hat{\mathbf{z}}$-center of column
N_e		total number of electrons
Q_{sector}		charge induced on a sector
Q_{coll}	Eq. 2.4	$\hat{\mathbf{z}}$-integrated density dumped through collimator hole

SYMBOLS continued

********** Frequencies and Times **********

$f_{l=i}$		$l = i$ diocotron frequency
$f_{l=1}^{\infty}$	Eq. 3.3	infinite length $l = 1$ diocotron frequency
$\Delta f_{l=1}$	$f_{l=1} - f_{l=1}^{\infty}$	finite length $l = 1$ frequency shift
f_{orb}		observed orbit frequency of two vortices
f_{orb}^{∞}	Eq. 4.2	infinite length orbit frequency of two point vortices
f_{osc}		oscillation frequency about a stable equilibrium point
γ		exponential growth rate
t		time
τ_{bounce}	Eq. 2.17	oscillation time for an electron along $\hat{z}$
τ_c	Eq. 2.16	time for electron to make a gyro-orbit
τ_{cut}		time for a cut gate to ramp between V_c and ground
τ_{ee}	Eq. 2.19	time for an electron-electron collision
τ_{eq}	Eq. 2.20	time for monotonic column to reach thermal equilibrium
$\tau_{i \to j}$		e-folding time for decay instability
$\tau_{l=i}$		e-folding time for a damping $l = i$ diocotron wave
τ_m	Eq. 2.21	mobility time: central density of column down 50%
τ_{merge}		time for two vortices to merge
$\tau_{rotation}$	Eq. 2.18	time for column to rotate about its own axis

********** Lengths **********

A_h	πR_{coll}^2		collimator hole area
D_{ij}		d_{ij}	distance between column (or image) i and j
L_c			containment length
L_{cyl}	7.89 cm.		length of EV apparatus cylinder
L_p	N_e/N_L		electron plasma column length
R_{coll}	1.59 mm.		collimator hole radius
R_H	0.4623 R_w	r_H	stability boundary for $r_1 = r_2$
R_i		r_i	displacement of column i from cylinder axis
R_{rms}	Eq. 3.7	r_{rms}	column radius (root-mean-squared)
R_v	Eq. 4.10	$\rho_v \equiv R_v/R_w$	column radius (radially-weighted integral)
R_w	3.81 cm.	$r_w \equiv 1$	cylinder wall radius

$\Rightarrow$ Lower case length variables are normalized to the wall radius R_w

SYMBOLS continued

********** **Velocities and Forces** **********

$v_\perp$		electron velocity perpendicular to the magnetic field
$v_\parallel$		electron velocity parallel to the magnetic field
v_E	Eq. 3.2	$\mathbf{E} \times \mathbf{B}$ drift velocity
Γ		circulation
$\zeta(r,\theta)$	$(4\pi ec/B)n(r,\theta)$	2D vorticity
ζ_{peak}		peak vorticity (normally at vortex center)

********** **Other** **********

V		applied or measured voltage (e.g. $V_c, V_{bias}, V_{sector}$)
$\phi_e(r,\theta,z)$		3D electric potential
$\phi(r,\theta)$		2D electric potential
$\mathbf{E}$		electric field
$\mathbf{B}$	$B_x + B_y + B_z$	main magnetic field
μ	$mv_\perp^2/2B$	gyromagnetic moment
$I_\parallel$	$\oint v_\parallel \, dz$	axial bounce adiabatic invariant
$\mathcal{P}_\theta$	Eq. 2.15	Canonical angular momentum
P_θ	Eq. 4.7	Scaled angular momentum for point vortices
L	Eq. 3.6	Normalized angular momentum per particle
ϵ	Eq. 3.10	eccentricity
q_2	Eq. 3.12	quadrupole moment
a/b	Eq. 3.11	aspect ratio
$-e$		electron charge
c		speed of light
k_B		Boltzmann constant

References

[1] H. Aref. Chaos in the dynamics of a few vortices- fundamentals and applications. In *Theoretical and Applied Mechanics.* IUTAM, 1985.

[2] B. R. Beck. *Measurement of the Magnetic and Temperature Dependence of the Electron-Electron Anisotropic Temperature Relaxation Rate.* PhD thesis, University of California at San Diego, 1990.

[3] R. Benzi, M. Colella, M. Briscolini, and P. Santangelo. A simple point vortex model for two-dimensional decaying turbulence. *Physics of Fluids*, A 4:1036, 1991.

[4] David L. Book. *NRL Plasma Formulary.* 1990.

[5] R. J. Briggs, J. D. Daugherty, and R. H. Levy. Role of landau damping in crossed-field electron beams and inviscid shear flow. *Physics of Fluids*, 13:421, Feb 1970.

[6] L. J. Campbell. Transverse normal modes of finite vortex arrays. *Physical Review A*, 24:514, 1981.

[7] O. Cardoso, D. Marteau, and P. Tabeling. Freely decaying two-dimensional turbulence: a quantitative experimental study. Submitted to *Phys. Rev. Lett.*

[8] G. F. Carnevale, J. C. McWilliams, Y. Pomeau, J. B. Weiss, and W. R. Young. Evolution of vortex statistics in two-dimensional turbulence. *Physical Review Letters*, 66:2735, 1991.

[9] B. Cluggish. Private Communication.

[10] B. Cluggish, J. H. Malmberg, T. B. Mitchell, and C. F. Driscoll. Damping of the l=1 diocotron mode and associated transport. *Bull. Am. Phys. Soc.*, 37:1415, 1992.

[11] S. Crooks and T. M. O'Neil. Private Communication.

[12] R. C. Davidson and N. A. Krall. Vlasov equilibria and stability of an electron gas. *Physics of Fluids*, 13:1543, 1970.

[13] Ronald C. Davidson. *Physics of Nonneutral Plasmas.* Addison-Wesley Publishing Co., 1990. and references within.

[14] J. S. deGrassie. *Equilibrium, Waves and Transport in the Pure Electron Plasma.* PhD thesis, University of California at San Diego, 1977.

[15] J. S. deGrassie and J. H. Malmberg. Waves and transport in the pure electron plasma. *Physics of Fluids*, 23:63, 1980.

[16] C. F. Driscoll. Observation of an unstable l=1 diocotron mode on a hollow electron column. *Physical Review Letters*, 64:645, 1989.

[17] C. F. Driscoll and K. S. Fine. Experiments on vortex dynamics in pure electron plasmas. *Physics of Fluids*, 6:1359, 1990.

[18] C. F. Driscoll, K. S. Fine, and J. H. Malmberg. Reduction of radial losses in a pure electron plasma. *Physics of Fluids*, 29:2015, 1986.

[19] C. F. Driscoll and J. H. Malmberg. Length-dependent containment of a pure electron plasma. *Physical Review Letters*, 50:167, 1983.

[20] C. F. Driscoll, J. H. Malmberg, and K. S. Fine. Observation of transport to thermal equilibrium in pure electron plasmas. *Physical Review Letters*, 60:1290, 1988.

[21] D. G. Dritschel and D. W. Waugh. Quantification of the inelastic interaction of unequal vortices in two-dimensional vortex dynamics. *Physics of Fluids*, A 4:1737, 1992.

[22] D. H. E. Dubin and T. M. O'Neil. Two-dimensional guiding-center transport of a pure electron plasma. *Physical Review Letters*, 60:1286, 1988.

[23] D. L. Eggleston, C. F. Driscoll, B. R. Beck, A. W. Hyatt, and J. H. Malmberg. Parallel energy analyzer for pure electron plasma devices. *Physics of Fluids*, 1992. Submitted.

[24] D. L. Eggleston and J. H. Malmberg. Observation of an induced-scattering instability driven by static field asymmetries in a pure electron plasma. *Physical Review Letters*, 59:1675, 1987.

[25] D. L. Eggleston, T. M. O'Neil, and J. H. Malmberg. Collective enhancement of radial transport. *Physical Review Letters*, 53:982, 1984.

[26] K. S. Fine. *Experiments with the l=1 Diocotron Mode.* PhD thesis, University of California at San Diego, 1988.

[27] K. S. Fine. Simple model of a finite length diocotron mode. *Bull. Am. Phys. Soc.*, 36:2331, 1991.

[28] K. S. Fine. Simple model of a nonlinear diocotron mode. *Physics of Fluids*, 1992. Submitted.

[29] K. S. Fine, C. F. Driscoll, J. H. Malmberg, and T. B. Mitchell. Measurements of symmetric vortex merger. *Physical Review Letters*, 67:588, 1991.

[30] P. Freymuth. On transition in a separated laminar boundary layer. *Journal of Fluid Mechanics*, 25:683, 1966.

[31] D. Gresillon and M. A. Dubois, editors. *Turbulence and Anomalous Transport in Magnetized Plasmas.* Editions de Physique, 1987.

[32] R. W. Griffiths and E. J. Hopfinger. Coalescing of geostrophic vortices. *Journal of Fluid Mechanics*, 178:73, 1987.

[33] G. W. Hart. The effect of a tilted magnetic field on the equilibrium of a pure electron plasma. *Physics of Fluids*, B3:2987, 1991.

[34] T. H. Havelock. The stability of motion of rectilinear vortices in ring formation. *Phil. Mag.S.7.*, 11:617, 1931.

[35] M. J. M. Hill. On the motion of fluid, part of which is moving rotationally and part irrotationally. *Phil. Trans. R. S.*, page 363, 1884.

[36] X. P. Huang. *Measurements of Two-Dimensional Freely Evolving Turbulence in a Magnetized Pure Electron Column.* PhD thesis, University of California at San Diego, 1993.

[37] A. W. Hyatt. *Measurement of the Anisotropic Temperature Relaxation Rate in a Magnetized Pure Electron Plasma.* PhD thesis, University of California at San Diego, 1988.

[38] C. A. Kapetanakos and A. W. Trivelpiece. Diagnostics of non-neutral plasmas using an induced-current electrostatic probe. *Journal of Applied Physics*, 42:4841, 1971.

[39] Yu. V. Katyshev, N. V. Makhaldiani, V. G. Makhankov, and A. B. Shvachka. Stable solutions for vortex systems. *Physics Letters*, 73A:39, 1979.

[40] G. Kirchhoff. *Vorlesungen Uber Mathematische Phsic.* B. G. Teubner, 1883.

[41] R. H. Levy. Diocotron instability in a cylindrical geometry. *Physics of Fluids*, 8:1288, 1965.

[42] R. H. Levy. Two new results in cylindrical diocotron theory. *Physics of Fluids*, 11:920, 1968.

[43] Lord Kelvin. Vibrations of a columnar vortex. *Phil. Mag.*, 10:155, 1880.

[44] A. E. H. Love. On the stability of certain vortex motions. *Proc. London Math. Soc.*, 25:18, 1893.

[45] J. H. Malmberg and J. S. deGrassie. Properties of a nonneutral plasma. *Physical Review Letters*, 35:577, 1975.

[46] J. C. McWilliams. The emergence of isolated coherent vortices in turbulent flow. *Journal of Fluid Mechanics*, 146:21, 1984.

[47] M. V. Melander, N. J. Zabusky, and J. C. McWilliams. Asymmetric vortex merger in two dimensions: Which vortex is 'victorious'? *Physics of Fluids*, 30, 1987.

[48] M. V. Melander, N. J. Zabusky, and J. C. McWilliams. Symmetric vortex merger in two dimensions: causes and conditions. *Journal of Fluid Mechanics*, 195, 1988.

[49] M. V. Melander, N. J. Zabusky, and A. S. Styczek. A moment model for vortex interactions of the two-dimensional euler equations. *Journal of Fluid Mechanics*, 167, 1986.

[50] T. B. Mitchell, C. F. Driscoll, and K. S. Fine. Experiments on stability of equilibria of two vortices in a cylindrical trap. *Physical Review Letters*, 1993. Submitted.

[51] J. D. Moody and J. H. Malmberg. The free expansion of a pure electron plasma column. *Physical Review Letters*, 1992. Submitted.

[52] T. M. O'Neil. A confinement theorem for nonneutral plasmas. *Physics of Fluids*, 23:2216, 1980.

[53] T. M. O'Neil. Cooling of a pure electron plasma by cyclotron radiation. *Physics of Fluids*, 23:725, 1980.

[54] T. M. O'Neil. New theory of transport due to like particle collisions. *Physical Review Letters*, 55:943, 1985.

[55] F. M. Penning. *Physica*, 3:873, 1936.

[56] A. J. Peurrung. *Measurement of a Magnetized Pure Electron Plasma.* PhD thesis, University of California at Berkeley, 1992.

[57] A. J. Peurrung and J. Fajans. A limitation to the analogy between pure electron plasmas and 2-d inviscid fluids. Submitted to *Phys. Rev. Lett.*

[58] S. A. Prasad and T. M. O'Neil. Finite length thermal equilibria of a pure electron plasma. *Physics of Fluids*, 22:278, 1979.

[59] W. H. Press, B. P. Flannery, S. A. Teuloksky, and W. T. Vetterling. *Numerical Recipes.* Cambridge University Press, 1986.

[60] C. W. Roberson and C. F. Driscoll, editors. *Non-Neutral Plasma Physics.* American Institute of Physics, 1988.

[61] K. V. Roberts and J. P. Christiansen. Topics in computational fluid mechanics. *Computer Physics Communications*, 3 Suppl.:14, 1972.

[62] V. J. Rossow. Convective merging of vortex cores in lift-generated wakes. *J. Aircraft*, 14:283, 1977.

[63] P. G. Saffman. *Vortex Dynamics.* Cambridge University Press, 1992.

[64] P. G. Saffman and R. Szeto. Equilibrium shapes of a pair of equal uniform vortices. *Physics of Fluids*, 23:12, 1980.

[65] R. A. Smith. Effects of electrostatic confinement fields and finite gyroradius on an instability of hollow electron columns. *Physics of Fluids*, B 4:287, 1992.

[66] R. A. Smith. Inviscid relaxation of distorted 2d vortices. *Bull. Am. Phys. Soc.*, 37:1767, 1992.

[67] J. J. Thomson. *A Treatise on the Motion of Vortex Rings.* MacMillan, 1883.

[68] D. W. Waugh. The efficiency of symmetric vortex merger. *Physics of Fluids*, A 4:1745, 1992.

[69] J. B. Weiss and J. C. McWilliams. Temporal scaling behavior of decaying two-dimensional turbulence. *Physics of Fluids*, 1993. Submitted.

[70] W. D. White and J. H. Malmberg. Feedback damping of the $l = 1$ diocotron wave. *Bull. Am. Phys. Soc.*, 27:1031, 1982.

[71] W. D. White, J. H. Malmberg, and C. F. Driscoll. Resistive wall destabilization of diocotron waves. *Physical Review Letters*, 49:1822, 1982.